LA-13121-T
Thesis

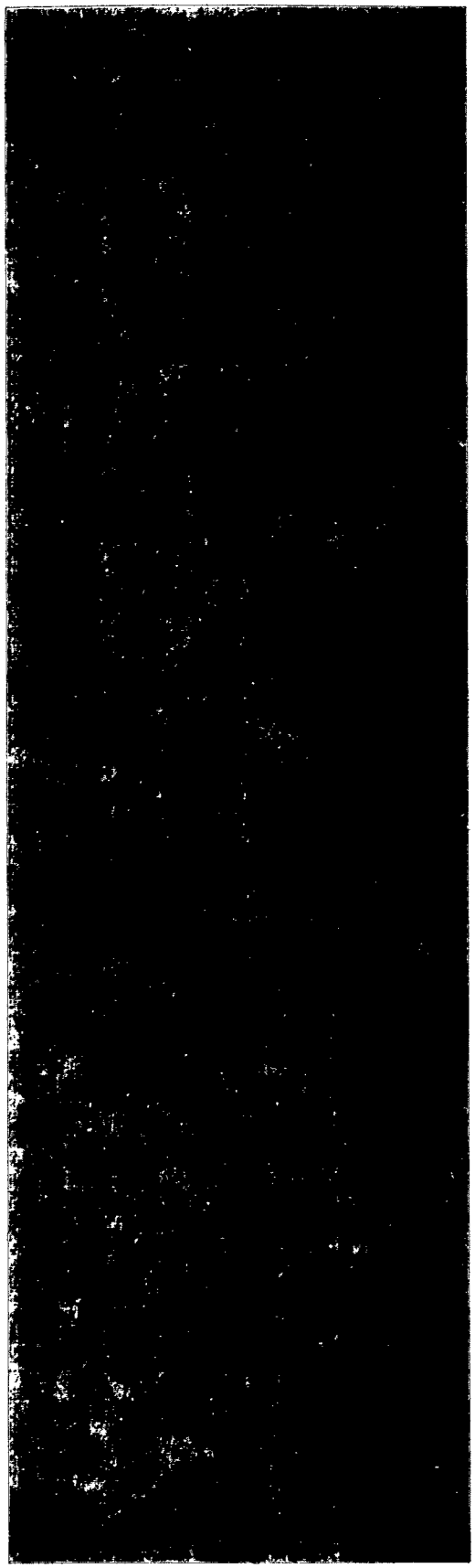

Three Dimensional Winds: A Maximum Cross-Correlation Application to Elastic Lidar Data

Los Alamos
NATIONAL LABORATORY

Los Alamos National Laboratory is operated by the University of California for the United States Department of Energy under contract W-7405-ENG-36.

This report was accepted by the Department of Physics, University of Texas at Austin, Austin, Texas, in partial fulfillment of the requirements for the degree of Doctor of Philosophy. The text and illustrations are the independent work of the author and only the front matter has been edited by the CIC-1 Writing and Editing Staff to conform with Department of Energy and Los Alamos National Laboratory publication policies.

An Affirmative Action/Equal Opportunity Employer

LA-13121-T
Thesis

UC-700
Issued: May 1996

Three Dimensional Winds: A Maximum Cross-Correlation Application to Elastic Lidar Data

William Tillman Buttler

Los Alamos
NATIONAL LABORATORY
Los Alamos, New Mexico 87545

TABLE OF CONTENTS

ACKNOWLEDGMENTS

I began development of remote wind sensing algorithms at the request of David Holtkamp (of the Los Alamos National Laboratory Physics Division) in the summer of 1992. By late 1993, I had developed a crude working version of the computer programs which I used to extract the wind fields plotted in Ch. 5.

The computer programs and algorithms currently used to extract wind information from Los Alamos National Laboratory (LANL) elastic lidar (light detection and ranging) data were developed, tested, and initially exercised on wind data acquired during the Barcelona Air Quality Initiative (BAQI) which took place in July 1992. At the request of Dr. Jose M. Baldasano, the director of the *Institut de Tecnologia i Modelització Ambiental* (ITEMA), Universitat Politècnica de Catalunya at Barcelona, Spain, lidar wind data were acquired to test a nonhydrostatic wind model in use at ITEMA. ITEMA funded a graduate student, Cecilia Soriano, to analyze the BAQI wind data. My discussions with Cecilia were invaluable in understanding the principles underlying the maximum cross-correlation method and their successful application to lidar data. Cecilia is currently using algorithms similar to those discussed in this thesis to analyze the BAQI data.

Experimental LANL lidar wind data were first acquired during the *1992 Mexico City Lidar Measurements Campaign*. Two methods were evaluated to extract wind speeds from the Mexico City data. Chuck Lebeda (of LANL's X Division) proposed a slope method to extract wind speeds from the lidar data, but I proposed the basic max-

imum cross-correlation method. Chuck Lebeda's slope idea failed to yield consistent results due to the sensitivity of the slope measurement with the Mexico City lidar data and was thus abandoned, but Chuck Lebeda's help and insight in evaluating both the slope method and the correlation method were instrumental to my success in the development and application of the maximum cross-correlation method to lidar data.

Others who contributed to my understanding of correlation techniques were Paul Pope (of LANL's EES Division) and John Moses (of LANL's Physics Division). Paul had applied a maximum cross-correlation technique to estimate surface velocities in the Mississippi River, and he sent me references to some of the papers he had read before he had analyzed his data. John Moses was my group leader in Physics Division at the time and he assisted me in working through some of the details of implementing correlation methods to one-dimensional data.

I considered the cross-correlation idea to be viable after studying several lidar wind sensing papers by Ed Eloranta, University of Wisconsin at Madison. Over the years, I had several discussions with Eloranta about his work in the field of elastic lidar winds. Eloranta's open discussions with me regarding his early work and his many papers on the subject of lidar winds inspired me and helped me better understand the application of correlation techniques to lidar data.

Douglas M. Alde (of LANL's EES Division) contributed to my understanding and success with the method. My discussions with Doug led to major improvements in

the final algorithms. Doug was a source of ideas and a resource of data processing techniques.

C. Fred Moore and George H. Nickel are two people without whose support, both financial and intellectual, I could not have completed my work. Fred is my University advisor and George is my LANL advisor. Both encouraged me and prodded me along to completion. George is the deepest resource of physics knowledge I have encountered. His study habits influence me in a positive way, and I am truly fortunate to have him as one of my thesis advisors.

I also acknowledge Joe J. Tiee and Charles R. Quick, Jr. (of LANL's CST Division), and David A. Clark (of LANL's Physics Division) for their help in acquiring the lidar data analyzed in this thesis. Those three people are outstanding lidar experts and friends.

The assistance of Bright Dornblaser and Pete Brightenbach (and others) of the Texas Natural Resource Conservation Commission, Carlos A. Rincon of the Environmental Defense Fund, Eric Aboe of the New Mexico Environment Department (and others), Howard Kraye (and others) of Santa Fe Technologies, and Bruce Kennedy and José Serna (and others) of the Physical Science Laboratory was important in the acquisition of the lidar data discussed in this thesis. Thank you all, and sincere apologies to those who assisted in this project but whose names have been omitted. The omission is unintentional. My regrets, and my thanks.

Special thanks to Lynn R. Veeser (my team leader), Joseph S. Ladish (my present group leader), and Thomas J. Bowles (a prior group leader) for all of their support in getting this thesis work done. They supported me through thick and thin, and are outstanding individuals whom it has been my pleasure to know.

Finally, thanks to Janet Slate (a personal friend), James P. Theiler (of LANL's NIS Division), David Oró (of LANL's Physics Division), Vaikunth Stewart (of LANL's CIC Division), and the others whose comment and review of my thesis led to a better document.

Bless you all.

This work was performed under the auspices of the Department of Energy.

Three-Dimensional Winds: A Maximum Cross-Correlation Application to Elastic Lidar Data

William Tillman Buttler

ABSTRACT

Maximum cross-correlation techniques have been used with satellite data to estimate winds and sea surface velocities for several years. Los Alamos National Laboratory (LANL) is currently using a variation of the basic maximum cross-correlation technique, coupled with a deterministic application of a vector median filter, to measure transverse winds as a function of range and altitude from incoherent elastic backscatter lidar (light detection and ranging) data taken throughout large volumes within the atmospheric boundary layer. Hourly representations of three-dimensional wind fields, derived from elastic lidar data taken during an air-quality study performed in a region of complex terrain near Sunland Park, New Mexico, are presented and compared with results from an Environmental Protection Agency (EPA) approved laser doppler velocimeter. The wind fields showed persistent large scale eddies as well as general terrain-following winds in the Rio Grande valley.

1

Light Detection and Ranging (Lidar)

A basic lidar system includes a laser with optics, an optical receiver to collect the scattered radiation, a detector to measure the power of the scattered radiation, electronics to digitize and record the detected scattered radiation, and a computer to control the lidar system. The different types of information imbedded within lidar data are related to the particular scattering process involved in the interaction of the laser light with atmospheric constituents (particulate aerosols, molecules, etc.). Common scattering processes are Mie scattering, Rayleigh scattering, Raman scattering, fluorescence, and resonance scattering.

Resonance scattering occurs when the incident radiation is absorbed and re-emitted by an atom or molecule. The absorption corresponds to a quantum mechanical transition of the absorber to an excited state; the excited state quickly decays to the ground state resulting in a re-emission of radiation at the same frequency as the inci-

dent radiation. The radiation is re-emitted in all directions. Jackson (Jackson 1975) discusses resonance scattering (also known as resonance florescence) in detail in Ch. 17, sec. 17.8 of *Classical Electrodynamics.*

Fluorescence differs from resonance scattering by the length of the transition lifetime of the excited state back down to its initial ground state, and in the mode of de-excitation. The resonating states in resonance scattering are short lived (less than a 10^{-9} s) while fluorescing states exist for lifetimes on the order of 10^{-9} s (Measures 1984). (Phosphorescence is a long lived fluorescent type process.) In the de-excitation process, the phosphorescing molecule or atom will cascade through more than one energy level in the transition from the excited state to the ground state.

Raman scattering is an inelastic process where the absorbed radiation is converted into mechanical energy, such as rotational energy. Raman spectra are often used to remotely measure temperatures in the atmosphere.

Rayleigh scattering results from electric dipole induced radiation from scatterers whose sizes are small relative to the wavelength of the incident radiation. The magnitude of Rayleigh scattering cross-sections depends on the square of the polarizability of the scatterers and is proportional to the inverse 4th power of the wavelength of the incident radiation (Jackson 1975). The wavelength of Rayleigh scattered radiation is the same wavelength as the incident radiation. The differential scattering cross-section, or angular distribution, of Rayleigh scattered light from small conducting spheres can be derived from a long wavelength approximation (Jackson, 1985; Bohren

et al. 1983) where the scatterer is small compared with the wavelength of the incident radiation.

Mie scattering results from magnetic and electric multipole induced radiation from spherical scatterers similar in size to the incident radiation. All of the dielectric properties of the scatterers must be considered when calculating Mie scattering cross-sections, and there is no simple result as in the Rayleigh case. Mie backscattering cross-sections are observed to be between 10 and 20 orders of magnitude larger than Rayleigh backscattering cross-sections (Measure 1984), and the wavelength of Mie scattered radiation is the same wavelength as the incident radiation. The differential scattering cross-sections of Mie scattered light often show many different intensity lobes between the forward and backward directions. The characteristic angular distribution of dipole radiation is peaked in the forward and backward directions and can be zero or near zero at directions transverse to the direction of the incident radiation. Mie scattering functions are calculated from exact solutions to Maxwell's vector wave equations for time varying electromagnetic fields impinging on the surface of small dielectric spheres. The boundary conditions on the electromagnetic radiation at the surface of the sphere are important in Mie calculations.

This thesis examines elastically scattered monostatic lidar data (in elastic light scattering the wavelength of the scattered light is the same wavelength as the incident light). Two common elastic light scattering processes in the atmosphere are Rayleigh (Jackson, 1985; Bohren et al. 1983) and Mie (Bohren et al. 1983) scattering.

The monostatic elastic nature of the lidar data means that the information imbedded in a lidar signal is minimal. A monostatic elastic lidar signal can change if the scattering species or one or more of the following properties of the scatterers changes: local number density, shapes, sizes, size distributions, species, or distributions. Thus, scattering aerosols are only minimally discussed. The scattering aerosols could be water, dust, or pollution; no attempt is made to classify the scattering aerosols.

Mie scattering cross-sections can be several orders of magnitude larger than the Rayleigh scattering cross-sections. The Rayleigh scattering cross-sections, differential as well as total scattering cross-sections (Jackson 1975; Bohren et al. 1983; Measures 1984), are proportional to the inverse power of the wavelength to the 4th power ($(d\sigma/d\Omega)_R$ and $\sigma_R \propto 1/\lambda^4$). Thus, for elastic scattering processes in the atmosphere, the wavelength of the lidar laser should be near the size of the atmospheric scatterers of interest. Based on this premise, the laser wavelength chosen for this study was 1.064 μm since a large number of man-made (anthropogenic) boundary-layer aerosols are between 0.1 μm and 10 μm (Measures 1984), and there are a minimal number of absorbers found in the boundary layer at this wavelength.

The motivation behind this thesis is the measurement of winds within the atmospheric boundary layer, and the main premise of this thesis is that boundary layer aerosols are carried along with the mean wind. This means that the main extinction mechanisms at this wavelength are elastic scattering processes, such as Mie and Ray-

leigh scattering (extinction is defined as the amount of light scattered and absorbed from the emitted laser pulse).

Finally, because the emitted laser light is an intensely focused beam, the emitted light scatters in all directions from the scattering region. This means that the scatterers behave as point sources distributing the scattered radiation over the surface of a sphere. Thus, the scattered lidar signal will decay as the inverse second power of the range from the scattering region. This leads to the monostatic backscattering lidar equation:

$$P(\lambda, r) = \frac{CE(\lambda)\,\beta(\lambda, r)\, e^{-2\int_0^r \alpha(\lambda, r')\, dr'}}{r^2}, \tag{1.1}$$

where $P(\lambda,r)$ is the amplitude of the lidar signal scattered from range r at wavelength λ; the amplitude corresponds to the rate at which photons are scattered back to the telescope (J/s). $\beta(\lambda,r)$ is the volume backscatter coefficient at range r and wavelength λ (1/m-sr). $\alpha(\lambda,r')$ is the volume extinction coefficient at range r' and wavelength λ (1/m); the factor of 2 precedes the volume extinction coefficient because the measured signal has traveled to and from the scattering region at range r. C is the system constant; this term combines the effects of optical transmission efficiencies in the telescope and filters, as well as the efficiency of the detector and the effective telescope collection area (m^3/s). $E(\lambda)$ is the laser energy per pulse at wavelength λ (J).

The functions β and α in Eq. 1.1 represent macroscopic quantities or averages over large numbers of scatterers. The scattering properties of each aerosol depend

on its size, shape, and refractive index. A macroscopic sample should contain a distribution of particle sizes and number densities even if there is only one kind of scatterer (and therefore only one refractive index). So, the backscatter power from such a simple-species sample can vary with the size distribution for fixed concentration and with the concentration for fixed-size distribution. The lidar only sees a change in backscatter power in a sample. Fig. 1.1 shows a typical lidar signal.

1-1 Data Reduction[1]

The amount of backscatter in lidar signal processing is solved by inverting the lidar equation (Eq. 1.1)—which is not possible with a monostatic lidar since there is one equation and two unknowns, α and β, which also depend on a number of variables themselves. The best known approach to inverting the lidar equation is referred to as Klett inversion (Klett 1981). Klett assumes a simple relationship between the volume extinction, $\alpha(\lambda,r)$, and the volume backscatter $\beta(\lambda,r)$; this assumption leads to a stable analytical inversion of the equation for which Klett offered some empirical data to support the validity of the inverted solution in certain situations. The conditions for accurately inverting the lidar equation are seldom met in the boundary layer, however; thus Klett solutions are of limited value in extracting the volume backscatter. Klett solutions are computationally stable, and the Klett method can improve the quality of lidar images. But there is no single solution to the lidar equation. A family of volume backscatter coefficients exists for every value of the volume extinction. One

1. Appendix A describes the LANL lidar system used to acquire data analyzed in this thesis.

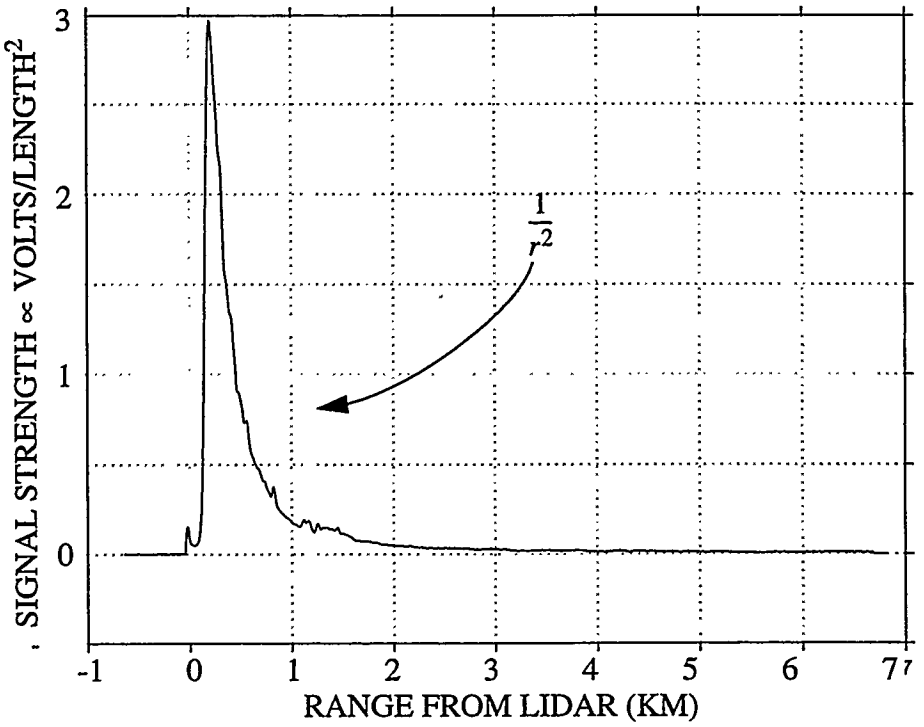

Fig. 1.1: Background Corrected Lidar Signal

The inverse decay of the lidar signal with range squared ($1/r^2$) is marked on the figure. The first 100 or so noise channels are seen between about -0.6 km and 0 km.

The digitizing electronics were triggered at the initial spike at 0 km. The spike marks the departure of the laser pulse.

Once the laser pulse is marked and timing begins, the backscatter signal rises from an initial value of 0 V/L^2 to a peak value near 3 V/L^2 at a distance of about 300 m from the lidar. The signal is increasing in this region because the laser beam exits 19 in. off the centerline of the telescope optical axis. Thus, the geometry of the collecting optics and the laser beam are such that the field of view (FOV) of the telescope and the laser beam do not completely overlap before about 300 m. The signal maximum occurs where the FOV of the telescope and the laser beam completely overlaps. When full overlap occurs, the $1/r^2$ decay of the backscatter lidar signal becomes evident.

Signal fluctuations in the $1/r^2$ region are caused by changing aerosol properties.

needs to know the sizes, shapes, densities, and species of the scatterers to know the extinction.

Only a few simple corrections are necessary to extract transverse winds from lidar data acquired within the boundary layer: (1) constant solar background noise; (2) the inverse r^2 decay of the signal; (3) high-frequency detector noise using a low-pass filter; and (4) when possible, fluctuations in signal strength caused by fluctuations in output laser power.

1-1.1 Background Subtraction

Averaging the first 100 digitized samples determines the constant solar-background noise. We acquire these first 100 samples during the delay time before the lidar signal data acquisition. Once lidar signal data acquisition begins, the digitizer records the flight time for the propagation and backscatter of the laser pulse. Collecting optics focus the backscattered light onto the avalanche photo diode. We use the flight time to extract range information from the digitized backscatter signals. Fig. 1.1 shows a background-corrected lidar signal.

1-1.2 Range Correction

Fig. 1.2 shows the background-corrected lidar signal (Fig. 1.1) after correcting for its $1/r^2$ dependence. In dry climates, or in regions where volume extinctions are small, these two corrections are often adequate for visualizing lidar data. Correcting for a small constant volume extinction improves lidar image quality.

1-1.3 Low-Pass Filtering

Two-dimensional low-pass filtering improves lidar image quality with regard to two effects: high-frequency detector noise (exhibited as fluctuations about the back-scatter signal), and variations in signal strength caused by fluctuations in output laser power. Two-dimensional low-pass filtering is effective in reducing high-frequency noise but only minimally corrects for the fluctuations in output laser power.

All lidar data discussed in this thesis are low-pass filtered with a two-dimensional Gaussian mask. The Gaussian mask works as a weighted averaging filter, and

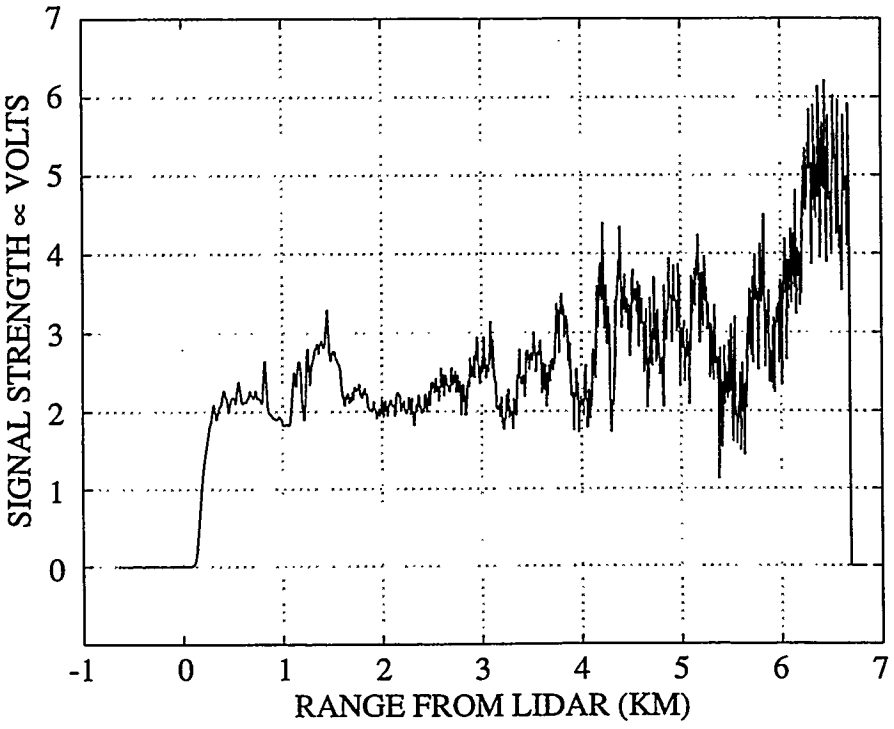

Fig. 1.2: Background and Range Corrected Signal

This range corrected signal clearly shows detail contained in backscatter lidar signals. These signals can be collected in a variety of formats to show the distributions of aerosols in the horizontal dimension, the vertical dimension, or both dimensions.

weights the data point at the center of the mask with a weighted sum of data points nearby; the Gaussian mask used to smooth the lidar data had a total of 5 weighting bins in the range dimension and 5 weighting bins in the transverse (time) dimension. I assigned the weights of the mask using the half widths described in the preceding discussion. Convolving the filter mask with the data accomplishes the low-pass filtering of the data with the Gaussian mask. Given two functions g, and h, the convolution of the two functions, denoted $g \bullet h$, is defined by Eq. 1.2 (Press et al. 1992):

$$g \bullet h \equiv \int_{-\infty}^{\infty}\int_{-\infty}^{\infty} g(\tau, \rho)h(t-\tau, \rho-r)d\tau d\rho. \tag{1.2}$$

The function g represents the two-dimensional averaging mask in Eq. 1.2. The filtering mask, g, is normalized such that the integral of $g \bullet h$ over the space and time variables, τ and ρ, results in a unitary (area preserving) transformation of the function h. The unitary nature of the transform is described in Eq. 1.3:

$$\text{If } g \text{ is defined } \ni \int_{-\infty}^{\infty}\int_{-\infty}^{\infty} g(\tau, \rho)d\tau d\rho \equiv 1, \text{ then}$$

$$\int_{-\infty}^{\infty}\int_{-\infty}^{\infty} h(t-\tau, \rho-r)d\tau d\rho = \int_{-\infty}^{\infty}\int_{-\infty}^{\infty} g(\tau, \rho)h(t-\tau, \rho-r)d\tau d\rho. \tag{1.3}$$

Although this restriction on the Gaussian mask is not essential for smoothing the data, the unitary nature of the transformation is a sound data processing technique and provides for direct comparisons of the unfiltered data with the filtered data.

1-1.3.1 Gaussian Mask Half Widths

The rate of digitization (20 megasamples per second) sufficiently over-samples the data to satisfy the Nyquist condition (Press et al. 1992); so, the bandwidth of the detector (3 MHz) places an upper bound of about 50 m on the minimum range resolution of the lidar detector system. I approximate the upper limit on the minimum lidar range resolution as the speed of light divided by 2 times the detector bandwidth, where the factor of 2 results from the emitted laser pulse traveling to and from the scattering region at range r. Thus, a Gaussian half width allowing for resolution of feature sizes of 30 to 50 m in the range dimension effectively removes high-frequency fluctuations in the backscatter lidar signal.

For lidar records collected at a fixed observation angle, the backscatter intensity will vary as a function of range and time. The upper limit on the minimum lidar resolution in the range dimension was estimated to be 50 m or less with the 3 MHz bandwidth detector, but there is no such restriction in the time dimension. I chose the filter half-width in the time dimension to help smooth fluctuations in the output laser power. Although a low-pass Gaussian filter does not completely correct for the shot-to-shot laser energy fluctuations, effects of energy fluctuations can be reduced.

I chose 1 range bin and 2 bins in the time dimension (for a set of lidar records collected at a fixed observation angle) for the filter's half widths. I calculated the range bins as the speed-of-light divided by 2 times the rate of digitization—7.5 m. The time separation of each time bin is a function of the number of times the laser is pulsed dur-

ing the acquisition of each backscatter lidar record. The lidar time bins were about 1.8 s in width. (These data are discussed in more detail in Ch. 3.)

1-1.4 Pseudo-Energy Correction

After the data have been corrected for the background noise, the $1/r^2$ dependence, and low-pass filtered, the data are pseudo-corrected for pulse-to-pulse fluctuations in the output laser power—when possible. The pseudo-correction for the laser power fluctuations is based on the assumption that aerosols flowing by any given observation angle are approximately constant during time periods on the order of one or two minutes. Based on this assumption, comparing multiple integrated backscatter return records (e. g., Fig. 1.1) for a set of lidar data records acquired at the same observation angle accomplishes energy normalization. This pseudo-correction will fail if a cloud passes by the lidar observation angle, but the correction works more than 95% of the time. A reliable and accurate measurement of each emitted laser pulse is required to properly correct for the output laser power fluctuations. The energy measurement principle is simple but a reliable measurement was not available for the data analyzed in this thesis.

References

Bohren, C. F., and D. R. Huffman, "Absorption and Scattering of Light by Small Particles," by John Wiley & Sons, Inc. (1983).

Buttler, W. T., C. Soriano, D. A. Clark, C. R. Quick, and T. N. Oakeley, "Sunland Park Border Air-Quality Study," Los Alamos National Laboratory Document LA-UR-95-861 (1995).

Jackson, J. D., "Classical Electrodynamics (Second Edition)," by John Wiley & Sons, Inc. (1975).

Klett, J. D., "Stable Analytical Inversion Solution For Processing Lidar Returns," *Applied Optics*, Vol. 20, No. 2 (1981).

Measures, R. M., "Laser Remote Sensing: Fundamentals and Applications," by John Wiley & Sons, Inc. (1984).

Press, W. H., S. A. Teukolsky, W. T. Vetterling, and B. P. Flannery, "Numerical Recipes in FORTRAN: The Art of Scientific Computing (Second Edition)," by Cambridge University Press (1992).

Suggested Reading

Klett, J. D., "Lidar Inversion With Variable Backscatter/Extinction Ratios," *Applied Optics*, Vol. 24, No. 11 (1985).

2

Atmospheric Physics

The remote measurement of winds within the earth's atmospheric boundary layer using lidar techniques is the objective of this thesis. Measurements discussed in this thesis were performed in the fluid atmosphere; because of this, a general discussion of thermodynamics and hydrodynamics of the atmosphere is included. However, little understanding or knowledge of either of these two fields of physics is necessary to understand the algorithms developed in this thesis.

2-1 The Atmospheric Boundary Layer

The atmospheric boundary layer is directly influenced through interactions with the surface of the earth. The region of the atmosphere directly above the atmospheric boundary layer is generally referred to as the free atmosphere and can be regarded as an ideal fluid where winds result from potential flow and the rotation of the earth, and where viscous forcings are small, i.e., motions in the free atmosphere are dominated by the Coriolis force and pressure gradients. Within the atmospheric

boundary layer lies the mixed layer, and the surface layer lies within the mixed layer. Residual layers of aerosols and pollutants are also within the atmospheric boundary layer.

The interaction of the fluid atmosphere with the surface of the earth results in frictional forcings between the earth and the atmosphere and thus an exchange of momentum. Boundary conditions require that the velocity of the fluid atmosphere be zero everywhere at the interface between the fluid atmosphere and the solid earth. These boundary conditions result in viscous damping in a thin layer near the surface of the earth—the boundary layer in which we live. Flow in the boundary layer can be laminar or turbulent and is characterized by considerable velocity gradients in the vertical dimension within the layer.

Surface interactions which lead to turbulence in the atmosphere include short- and long-wave radiative processes, evaporation and transpiration, and frictional forces. Long-wave radiative processes vary with the local characteristics of the surface, i.e., radiant exchange is different for concrete than for soil, or grass. Short-wave radiative processes include reflection and absorption of solar radiation—the albedo. Short-wave processes also directly affect the rate of evaporation of water into the atmosphere, another important surface interaction affecting dynamics within atmospheric boundary layer.

Intense vertical mixing of scalar quantities such as water vapor, and potential temperature through advective and turbulent processes characterize the mixed layer.

Vertical profiles in which potential temperature and humidity are nearly constant with height characterize this portion of the atmospheric boundary layer. Advection and convection or turbulence are the main forces mixing aerosols, pollution, and scalar quantities in the mixed layer. Anthropogenic processes such as industrial emissions from power plants and wind shear which often occurs across the top of the mixed layer also account for some of the mixing. The thickness or depth of the mixed layer is generally greatest near solar noon, constant or nearly constant until sunset, and least just before sunrise. A capping inversion in the potential temperature marks the top of the mixed layer.

The region between the mixed layer and the free atmosphere is the entrainment zone. Sporadic thermals which rise above the mixed layer entrain cleaner air from the free atmosphere above into the boundary layer below. Kelvin-Helmholtz waves, and sometimes clouds, perform a similar function. These thermals which penetrate from the mixed layer into the free atmosphere have a negative buoyancy, and settle into the boundary layer since there is little turbulence in the free atmosphere. Clean, warmer air from the free atmosphere entrained into the boundary layer rapidly mixes into the mixed layer due to the turbulent nature of this region of the atmosphere. This causes the depth of the mixed layer to grow. Less turbulent air entrained into more turbulent air increases the thickness or depth of the mixed layer. Turbulent entrainment of clearer air from the free atmosphere into the mixed layer, folded repeatedly by overturning turbulent cells, is one major source of structure in the aerosol density. (Tem-

perature, pressure, and humidity characterize a meteorological structure. In this thesis, structure refers to a random, but organized, coherent pattern observed in atmospheric aerosol distributions. These patterns exist for finite measurable time periods.) The other source of structure in the aerosol densities are emissions near the surface.[1]

The lowest 5% to 10% of the atmospheric boundary layer is called the surface layer. Mixing processes within this layer are considered reversible and adiabatic (Stull 1988), and throughout the main body of the mixed layer (the lowest 35% to 80% of the atmospheric boundary layer) mixing processes are nearly adiabatic. The surface layer is not readily discriminated by elastic-backscatter lidar techniques.

Residual layers are thought to develop after thermals cease to form, when turbulence decays at sunset. The decaying turbulence leads to a general subsidence of the depth of the mixed layer. Aerosols, pollution and moisture may then be trapped above the top of the receding mixed layer. After the sun rises, photochemical processes in the residual layer can result in the production of ozone and other photochemically produced pollutants. During the night, some pollutants may react with moisture and other residual-layer constituents to form new compounds. Aerosols in these layers either swell through the absorption of moisture or adsorb moisture and precipitate out. Residual layers are usually entrained down into the mixed layer after turbulence is fully developed during the daytime, but residual layers may also persist for several

1. Personal communications with E. W. Eloranta were very helpful in gaining insight into boundary layer structure resulting from the folding of clearer air from the free atmosphere down into the dirtier mixed layer air.

days (Buttler et al. 1994). Multiple residual layers were observed during the Barcelona Air-Quality Initiative.

The "top" of the mixed layer, or the "top" of the atmospheric boundary layer, are not smooth flat surfaces. A capping temperature inversion and thermals that penetrate adjacent layers and entrain clearer air into the more turbulent atmosphere below define this surface.

2-2 Thermodynamics

A parcel of air has many degrees of freedom, and may be defined with a few parameters called state variables. There are two types of state variables of importance: *intensive* and *extensive* variables. Intensive variables do not change in value when the size (spatial extent and number of degrees of freedom) of the system changes. The intensity of the intensive variable remains the same when the *extent* of the thermodynamic system changes. Examples of intensive variables are pressure, P, and temperature, T; volume, V, and entropy, S, are examples of extensive variables. Extensive and intensive variables occur in pairs.

The internal energy, U:

$$U = ST - PV + \sum_j \mu_j N_j, \tag{2.1}$$

where S is entropy, T is temperature, P is pressure, V is volume, μ is the chemical potential, and N is the number of chemical species with chemical potential μ describes

how much energy is stored in a thermodynamic system. S, V, and N are extensive variables while T, P, and μ are intensive variables.

Many times in an experiment, we must identify the independent variables which are readily measured. For instance, often it is easier to fix the volume and vary the pressure, or to vary the temperature, etc. In this case we find that the form of the internal energy equation is not appropriate to conduct the experiment and we must transform the thermodynamic equation in a fashion where the extensive variables are appropriate for the experiment. These types of transformations are called *Legendre* transformations (Reichl 1980). For instance, if we wish to change our independent variables from S and V to S and P, then we calculate the differential of the internal energy, U, minus $(-PV)$. The resulting equation, called the *enthalpy*, is useful for describing experiments carried out at constant entropy and pressure. The *Helmholtz* free energy results from subtracting ST from the internal energy, U, and the *Gibbs* free energy results from subtracting ST and $(-PV)$ from the internal energy, U. In summary

$$\begin{aligned}
&\text{Internal Energy: } U = ST - PV + \sum_j \mu_j N_j, \\
&\text{Enthalpy: } H = U + PV, \\
&\text{Helmholtz Free Energy: } A = U - ST, \\
&\text{Gibbs Free Energy: } G = U + PV - ST.
\end{aligned} \tag{2.2}$$

In *exact* differential form, we have:

$$
\begin{aligned}
dU &= TdS - PdV + \sum_j \mu_j dN_j, \\
dH &= dU + PdV + VdP = TdS + VdP + \sum_j \mu_j dN_j, \\
dA &= -SdT - PdV + \sum_j \mu_j dN_j, \\
dG &= -SdT + VdP + \sum_j \mu_j dN_j.
\end{aligned}
\tag{2.3}
$$

Since these thermodynamic equations are exact differentials, definitions for temperature, entropy, volume, and pressure (for simplicity, assume that dN=0) are

$$
\begin{aligned}
dU &= TdS - PdV \Rightarrow T = \left.\frac{\partial U}{\partial S}\right)_V \wedge -P = \left.\frac{\partial U}{\partial V}\right)_S, \\
dH &= TdS + VdP \Rightarrow V = \left.\frac{\partial H}{\partial P}\right)_S, \\
dA &= -SdT - PdV \Rightarrow -S = \left.\frac{\partial A}{\partial T}\right)_V.
\end{aligned}
\tag{2.4}
$$

Furthermore, since the variables are independent, rates of change between many different thermodynamic quantities are related; these relations are referred to as *Maxwell* relations (Reichl 1980).

In summary, the internal energy, U, is useful for describing processes which occur at constant V, S, and N. The enthalpy, H, describes processes which occur at constant S, P, and N. The Helmholtz free energy, A, describes processes carried out at constant T, V, and N. The Gibbs free energy, G, describes processes which occur at constant P, T, and N.

2-2.1 Ideal Gas

The equation of state for an ideal gas is

$$PV = nRT, \tag{2.5}$$

where n is the number of moles and R is the universal gas constant. Particles or molecules in a liquid or gaseous state, within a confined volume, have a three translational degrees of freedom. There are also three possible rotational degrees of freedom. Not all of the rotational degrees of freedom are accessible, however.

Consider a diatomic molecule in the form of a dumbbell such that the two atoms are assumed to be point-masses possessing equal moments of inertia, I, about axes at right angles to a line connecting the two masses (Fig. 2.1). The energy of a free diatomic molecule has three possible contributions: translational energy, rotational energy, and vibrational energy, i.e.,

$$\varepsilon = \varepsilon_{trans} + \varepsilon_{rot} + \varepsilon_{vib} = \frac{p^2}{2m} + \frac{L^2}{2I} + \frac{m\omega^2 l_0^2}{2}, \tag{2.6}$$

where l_0 is a length scale characteristic to an atomic vibration displacement.

A *Boltzmann* gas will have a classical momentum, p, while the rotational and vibrational states are excited quantum mechanically such that

$$\varepsilon_{l,n} = \frac{m\langle v^2\rangle}{2} + \frac{l(l+1)\,\hbar^2}{2I} + \left(n + \frac{1}{2}\right)\hbar\omega. \tag{2.7}$$

2-2.2 Rotational Energy

The moment of inertia of a diatomic nitrogen (N_2) rigid rotor about a line perpendicular to the line joining the two masses (Fig. 2.1) is

$$I_A \approx \frac{14 \times m_p l_A^2}{2} \sim 7.3\times10^{-34} MeV \cdot s^2, \tag{2.8}$$

where the length scale, l_A, of atomic dimensions for molecules, is on the order of angstroms, or $l_A \sim 10^{-10}$ m. There are *two* degrees of freedom for rotations about a line perpendicular to the line joining the two masses.

For rotations around the axis joining the two masses, the dimension of interest is on the order of *nuclear* dimensions, i.e., $l_N \sim 10^{-15}$ m. The moment of inertia for rotations about this axis will be

$$I_N \approx 2 \times \frac{2}{5} \times 14 \times m_p \frac{l_N^2}{4} \sim 2.9\times10^{-44} MeV \cdot s^2. \tag{2.9}$$

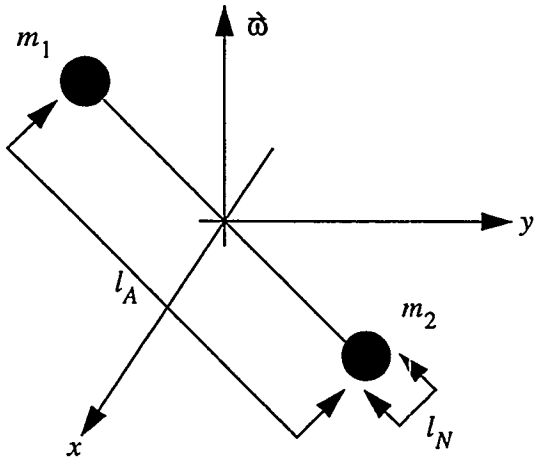

Fig. 2.1: Rigid Rotor

A characteristic temperature (Sommerfeld 1956) for quantum mechanical rotational states is defined as follows

$$\Theta = \frac{\hbar^2}{2Ik_B}, \tag{2.10}$$

where the quantized rotational energy is

$$\varepsilon_{rot} = l(l+1)\frac{\hbar^2}{2I}, \tag{2.11}$$

and the rotational energy states are $(2l+1)$ degenerate, where l is the quantum number associated with the angular momentum of the diatomic molecule.

Thus, rotations about the axes at right angles to the line joining the two masses will contribute to the gas constant when the temperature is greater than

$$\Theta_A \sim \frac{2.6\times10^{-27} eV \cdot s^2}{I_A} \sim 3.6K, \tag{2.12}$$

and rotations about the line joining the two masses are excited when the temperature is greater than

$$\Theta_N \sim \frac{2.6\times10^{-27} eV \cdot s^2}{I_N} \sim 1\times10^{11} K. \tag{2.13}$$

When $T \ll \Theta_A$, rotational states are frozen and N_2 behaves as a monatomic fluid. N_2 will be in a solid state long before $T=\Theta_A$. T_m, the melting point of N_2, is ~63 K—a difference of about 60 degrees. The main assumption in the calculation was that the length of the atomic bond for N_2, l_A, was one angstrom (Å=10^{-10} m). We could work backwards with our knowledge of the melting temperature of N_2 to get an esti-

mate on the length of the atomic bond of N_2 (or other diatomic molecules for that matter).

When $T \gg \Theta_A$, the value of Z_{rot}, the rotational partition function is

$$Z_{rot} = \sum_{l=0}^{\infty} (2l+1) e^{-l(l+1)\Theta/T}. \tag{2.14}$$

Let $x_l = l(l+1)\Theta/T$. Calculate Δx_l and transform the sum to an integral:

$$\begin{aligned} \Delta x_l &= x_l - x_{(l-1)} = 2l\frac{\Theta}{T}, \\ \Rightarrow Z_{rot} &= \frac{T}{\Theta}\int_0^{\infty} e^{-x} dx + \sum_{l=0}^{\infty} e^{-l(l+1)\Theta_c/T} = \frac{T}{\Theta} + Rem. \end{aligned} \tag{2.15}$$

In the classical limit where $T \gg \Theta_A$, the remainder term is small, and we find for the energy per unit mass, u:

$$u_{rot} = k_B T^2 \frac{d}{dT} \ln(Z_{rot}) = k_B T = \frac{2}{2} k_B T, \tag{2.16}$$

where the rotational energy per unit mass is the number of degrees of freedom (2) divided by 2 times $k_B T$. (Two rotatiogas constantnal degrees of freedom contribute to the gas constant for diatomic molecules.)

The logical conclusion is that a diatomic molecule will disassociate *long* before rotational states about the axis joining the two masses can be excited—they are not accessible. Thus, diatomic molecules have *three* translational degrees of freedom and *two* rotational degrees of freedom—a total of *five* degrees of freedom which contribute to the gas constant, R.

2-2.3 Vibrational Energy

A similar argument can be applied for the vibrational energy states and the resulting characteristic temperature is

$$\Theta = \frac{\hbar\omega}{k_B}. \tag{2.17}$$

Vibrational states are only excited at high temperatures and add a total of two additional degrees of freedom. At temperatures of interest in the atmosphere, however, these vibrational degrees of freedom are not excited. There are a total of three translational degrees of freedom and two rotational degrees of freedom for diatomic gases. On average, polyatomic gases have one additional degree of freedom.

2-2.4 Thermodynamic Quantities

The equation of state for the internal energy of an ideal gas is

$$U = \alpha RT = C_V T, \tag{2.18}$$

where

$$C_V \approx \frac{5}{2}R = \frac{5}{2}Nk_B = \frac{5}{2}\cdot\frac{6.022\times10^{23}}{mol}\cdot\frac{1.381\times10^{-23}J\cdot K^{-1}}{28.9g\cdot mol^{-1}} \sim 720\frac{J\cdot K^{-1}}{kg} \tag{2.19}$$

for *dry* air. The result is only approximate since the assumption that dry air consists mainly of diatomic molecules, i.e., N_2, and O_2, isn't quite right. Although nitrogen, N, and oxygen, O, are mostly diatomic, and compose 78% and 21% of our atmosphere, respectively, another ~1% of our atmosphere is a mix of monatomic, diatomic, and

polyatomic molecules. For example, other common diatomic molecules in our atmosphere are HO, NO, and CO. Polyatomic molecules include CO_2, SO_x, NO_x, O_3. (Many of the aforementioned chemical compounds are commonly found in our boundary layer and often have anthropogenic sources.) In the calculation for the heat capacity of dry air at constant volume, 28.97 $g{\cdot}mol^{-1}$ is a more accurate value for the mass of dry air, m_d, rather than m_d=28.9 $g{\cdot}mol^{-1}$=28.6/0.99 $g{\cdot}mol^{-1}$ (28.6 $g{\cdot}mol^{-1}$ is the mass of 99% of our atmosphere—the nitrogen and oxygen; division by 0.99 normalizes the gas constant to a 100% diatomic atmosphere composed of N_2, and O_2). m_d=28.6 $g{\cdot}mol^{-1}$ appropriately corrected for the number of degrees of freedom of the remaining 1% of our atmosphere yields C_V~716 $J{\cdot}kg^{-1}{\cdot}K^{-1}$, for dry air. Assuming a diatomic atmosphere gives C_V=720 $J{\cdot}kg^{-1}{\cdot}K^{-1}$ which is close to the correct result of C_V=716 $J{\cdot}kg^{-1}{\cdot}K^{-1}$ (Brutsaert 1982).

The enthalpy is

$$H = U + PV = C_V T + RT = C_P T \Rightarrow C_P = R + C_V. \tag{2.20}$$

The entropy is

$$dH = dU - d(-PV) = TdS + VdP \Rightarrow dS = \frac{1}{T}(dH - VdP), \text{ but}$$

$$V = \frac{RT}{P}, \text{ and } dH = C_p dT \Rightarrow S - S_0 = C_p \ln\frac{T}{T_0} - R\ln\frac{P}{P_0}, \tag{2.21}$$

$$\Rightarrow \Delta S = C_p \ln\left(\frac{T}{T_0}\cdot\left(\frac{P_0}{P}\right)^{R/C_p}\right) = C_p \ln\left(\frac{\Theta}{T_0}\right),$$

where Θ is the *potential* temperature, i.e.,

$$\Theta = T_0 e^{\Delta S/C_p} \equiv T\left(\frac{P_0}{P}\right)^{R/C_p} \approx T\left(\frac{P_0}{P}\right)^{R/\left(\frac{5}{2}R+R\right)} = T\left(\frac{P_0}{P}\right)^{2/7}. \tag{2.22}$$

The symbol Θ represents the temperature a parcel of air at pressure P and temperature T will have when compressed adiabatically to pressure P_0. This process is natural in our atmosphere and thus potential temperature is used to describe temperature profiles of our atmosphere. For example, the absolute temperature of a parcel of air may be much lower than temperatures at sea level, but the parcel of air may have a higher potential temperature. When this is true, the parcel of air will be some altitude above sea level. Thus, potential temperature describes the temperature a parcel of air at some altitude, z, would have if it were at sea level, 1 atmosphere of pressure, and 0° Celsius.

2-2.5 Moist Air

The equation of state for dry air is

$$P_d V_d = RT \Leftrightarrow P_d = \rho_d RT. \tag{2.23}$$

Mix in some water vapor such that

$$\begin{aligned} p &= p_d + p', \\ \rho &= \rho_d + \rho', \end{aligned} \tag{2.24}$$

where the primed coordinates correspond to the pressure and density of water vapor, and the subscript, d, denotes dry air. In the spirit of Chuck Leith,[2] mixing ratio is defined as,

$$\mu = \frac{\rho'}{\rho_d}. \tag{2.25}$$

For the equation of state,

$$\begin{aligned} p &= \rho_d RT + p' = RT\left(\rho_d + \rho'\frac{R'}{R}\right) = RT\left(\rho - \rho' + \rho'\frac{R'}{R}\right), \\ &= \rho RT\left[1 - \frac{\rho'}{\rho}\left(1 - \frac{R'}{R}\right)\right] = \rho RT\left[1 + \frac{\rho'}{\rho_d(1+\rho'/\rho_d)}\left(\frac{1 - R/R'}{R/R'}\right)\right], \\ &= \rho RT\left[1 + \frac{\mu}{(1+\mu)}\left(\frac{1 - R/R'}{R/R'}\right)\right]. \end{aligned} \tag{2.26}$$

Define σ to be the ratio of the heat capacity of dry air to the heat capacity of water vapor, i.e.,

$$\begin{aligned} \sigma &\equiv \frac{R}{R'} \approx \frac{18g \cdot mol^{-1}}{28.97g \cdot mol^{-1}} = 0.621, \\ \Rightarrow \frac{p}{\rho} &= RT\left[1 + \frac{\mu}{(1+\mu)}\frac{(1-\sigma)}{\sigma}\right] = RT\left[1 + 0.61\frac{\mu}{(1+\mu)}\right]. \end{aligned} \tag{2.27}$$

The specific humidity, q (Brutsaert 1982), is defined as the ratio of mass of water vapor per unit mass of moist air

$$q = \frac{\rho'}{\rho} = \frac{\mu}{(1+\mu)} \Rightarrow p/\rho = RT(1 + 0.61q). \tag{2.28}$$

2. C. E. Leith supervised George H. Nickel during George's Ph.D. work at Livermore National Laboratory. George H. Nickel, in turn, supervised my Ph.D. work at Los Alamos National Laboratory. Much of my understanding of atmospheric physics has come directly from Chuck Leith notes from the 1960's.

The virtual temperature, T_V, is defined as the temperature dry air should have in order to have the same density as moist air with given q, T, and p:

$$T_V \equiv T(1 + 0.61q) \Rightarrow p/\rho = RT_V. \tag{2.29}$$

This means that moist air has the properties of dry air at a higher temperature, or lower density at the same pressure.

2-2.6 Latent Heat of Vaporization

During a phase change, such as liquid to vapor, or solid to vapor, or solid to liquid, heat is either absorbed or released. A coexistence curve (between a gas and a liquid, for example), is used to determine the relationship for the heat absorbed or released during the phase change. The Gibbs free energies of the coexisting phases in an ideal *PVT* system must be equal. Thus during the phase change, the change between the Gibbs free energies are equal. This leads to the Clausius-Clapeyron relation

$$\left.\frac{dP}{dT}\right)_{Coex} = \frac{\Delta S}{\Delta V} = \frac{\Delta H}{T\Delta V}, \tag{2.30}$$

where ΔH is the heat absorbed or released during the phase change, and ΔV is the change in volume. For the case of a phase change from a liquid to a gas, the volume of the gas is much larger than the volume of the liquid; neglect the volume of the liquid to find

$$\left.\frac{dP}{dT}\right)_{Coex} \sim \frac{\Delta H}{TV_{gas}}. \tag{2.31}$$

The heat absorbed or released during the phase change is called the latent heat. The process is reversible and the latent heat of vaporization is equal to the negative of the latent heat of condensation. The phase changes of water in our atmosphere lead to low and high pressure regions which drive atmospheric dynamics.

2-3 Hydrodynamics

Our atmosphere is a fluid in motion within a rotating reference frame. The thermodynamic properties of the atmosphere influence motions within and above the boundary layer. Reversible phase changes of water force motions in the atmosphere.

2-3.1 Physics in a Rotating Frame of Reference

Consider motions in a rotating frame of reference from an inertial frame (Fig. 2.2).

(2.32) $$\vec{R} = \vec{r}_1 + \vec{r}_2.$$

Eq. 2.32 implies

(2.33) $$\frac{d}{dt}\vec{R} = \frac{d}{dt}\left(\vec{r}_1 + \vec{r}_2\right) = \dot{\vec{r}}_1 + \dot{\vec{r}}_2.$$

Note that

(2.34) $$\vec{r}_2 = \sum_{i=1}^{3} x_i e_i,$$

and this implies

$$\dot{\vec{r}}_2 = \frac{d}{dt}\sum_{i=1}^{3} x_i e_i = \sum_{i=1}^{3}\left(\dot{x}_i e_i + x_i \dot{e}_i\right). \tag{2.35}$$

This term accounts for motions of the particle (or parcel of air) at $\vec{r}_2$ with respect to the origin; the first term on the far right of Eq. 2.33 accounts for motions of the origin of the rotating frame with respect to the observer. If the distance between the inertial frame and the rotating frame is constant, then

$$\frac{d\vec{r}_1}{dt} \equiv 0, \tag{2.36}$$

and this is the case in point. Thus,

$$\frac{d\vec{R}}{dt} = \frac{d\vec{r}_2}{dt} = \dot{\vec{r}}_2 = \sum_{i=1}^{3}\left(\dot{x}_i e_i + x_i \dot{e}_i\right). \tag{2.37}$$

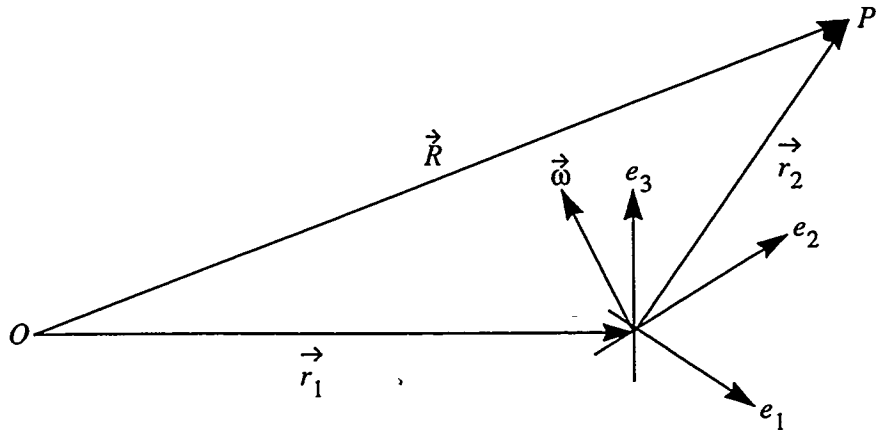

Fig. 2.2: Rotating Reference Frame

The observation point is located at O (an inertial frame of reference), and the observer is at rest observing how $\vec{R}$, which describes a vector between the observer and the particle (or parcel of air) at point P, changes with time. The axes are fixed in a reference frame which is in motion with respect to O. The point P is in motion with respect to the axes and the observer at O.

The time derivative of any unit axis is

$$\frac{d}{dt}e_i \equiv \vec{\omega} \times e_i, \tag{2.38}$$

where $\vec{\omega}$ is the axis about which the rotating frame of reference is turning. This implies that

$$\frac{d}{dt}\vec{R} = \sum_{i=1}^{3}\left(\dot{x}_i e_i + x_i \dot{e}_i\right) = \vec{v}_2 + \vec{\omega} \times \vec{r}_2. \tag{2.39}$$

To determine the equations of motion take another time derivative to find how the particle is accelerating with respect to the observer. This gives

$$\begin{aligned} \frac{d^2}{dt^2}\vec{R} &= \frac{d}{dt}\sum_{i=1}^{3}\left(\dot{x}_i e_i\right) + \frac{d}{dt}\left(\vec{\omega} \times \vec{r}_2\right), \\ &= \left[\vec{a}_2 + \vec{\omega} \times \vec{v}_2\right] + \left[\dot{\vec{\omega}} \times \vec{r}_2 + \vec{\omega} \times \left(\vec{v}_2 + \vec{\omega} \times \vec{r}_2\right)\right], \\ &\equiv \vec{a}_2 + 2\vec{\omega} \times \vec{v}_2 + \vec{\omega} \times \left(\vec{\omega} \times \vec{r}_2\right). \end{aligned} \tag{2.40}$$

The subscripts on the position, velocity, and acceleration of the particle in the rotating reference frame add nothing to the meaning of Eq. 2.40, thus we drop them and solve for the acceleration on the particle to find

$$\vec{a} = \frac{\vec{F}}{m} - 2\vec{\omega} \times \vec{v} - \vec{\omega} \times \left(\vec{\omega} \times \vec{r}\right). \tag{2.41}$$

For the situation where the earth is the rotating reference frame, $\vec{\omega}$ is the angular frequency corresponding to the period of the earth's rotation and is aligned along the earth's rotational axis—not the earth's symmetry axis. For short time periods $\vec{\omega}$ can be considered constant. (In reality $\vec{\omega}$ precesses about an axis defined by the earth's angular momentum, $\vec{L}$. In turn, the angular momentum axis precesses

about the earth's symmetry axis. This precession of the $\vec{\omega}$ axis about $\vec{L}$ is known as the *Chandler wobble* (Baierlein 1983). The period of the wobble is more than 400 times longer than the period of the earth's rotation and thus can be ignored in this problem.) The first term on the right hand side of Eq. 2.41 includes gravitational acceleration and any forces which act on particles in rotating reference frames, such as from viscous effects in the atmosphere. The second term is the *Coriolis term.* The third term on the right hand side of Eq. 2.41 is a correction to the gravitational force caused by the earth's rotation. Thus,

$$\vec{g} \equiv -\left(\frac{GM_{\text{Earth}}}{r^2}\right)e_3 - \vec{\omega} \times (\vec{\omega} \times \vec{r}) . \tag{2.42}$$

2-3.2 The Hydrostatic Equation

Our atmosphere exists because of our gravitational field, its density decreases with altitude. The hydrostatic equation is based on the assumption that the atmosphere is in static equilibrium, i.e., gravitational forces are balanced with the vertical pressure gradients. This implies that

$$\ddot{z} = -g - \frac{1}{\rho} dp = 0, \tag{2.43}$$

or

$$g = -\frac{1}{\rho} dp \Leftrightarrow g dz. \tag{2.44}$$

With $\rho = 1/V$ and $dS \equiv 0$, Eq. 2.44 states that the differential of the enthalpy, dH, is equivalent to gdz.

From the ideal gas law,

(2.45) $$\rho = \frac{p}{RT}.$$

This implies

(2.46) $$p = p_0 e^{-z/z_0},$$

where

(2.47) $$z_0 = \frac{RT}{g},$$

and p_0 is the pressure at z=0.

Vertical motions in the atmosphere are negligible in the hydrostatic approximation. Vertical motions are indeed small compared to the horizontal motions in our atmosphere. Consider forcings on a parcel of air due to pressure differences. The acceleration on the parcel of air is

(2.48) $$\vec{a} = \frac{\vec{F'}}{\rho} - \frac{\nabla p}{\rho} - 2\vec{\omega} \times \vec{v} + \vec{g},$$

where Eq. 2.42 describes $\vec{g}$ and $\vec{F'}$ includes viscous forces.

2-3.3 Viscous Forcings

The hydrostatic equation assumes that vertical pressure forcings are equal and opposite to the sum of the gravitational forcings and the centripetal forcings. Consider a plane normal to the sum of the centripetal and gravitational forces. In an atmosphere at rest (hydrostatic equilibrium), the traction (Kennard 1938) across the plane

(the force per unit area) is normal to the plane, i.e., the traction tangential to the plane is zero everywhere. In an atmosphere which is not at rest, tractions are both normal to the plane as well as tangential to the plane. Tangential tractions result in shearing motions in the fluid and are the phenomenon of viscosity. In incompressible fluids, the shearing component of the stress is proportional to the velocity gradient.

2-3.3.1 Self Diffusion

On the molecular level random motions with equal probabilities in all directions exist. Molecules move and collide with other molecules altering the directions of the colliding molecules. The collisions create shear stresses and can diffuse momentum away from the parcel of air.

Identical particles unevenly distributed throughout a volume will diffuse until they are evenly distributed throughout the volume which they occupy. The rate of this particle diffusion of identical particles is called the coefficient of self-diffusion.

The coefficient of kinematic viscosity is the coefficient of viscosity divided by its mass density. The net transport of molecules across the imaginary plane in the gas during the diffusion process requires finding the number of molecules which cross the imaginary plane from the upper half plane (Reichl 1980). Consider a segment of our plane, dS, whose coordinate system is defined such that dS is centered on the coordinate system. Next consider a volume element, dV, of the gas positioned at r, θ, and ϕ in the coordinate system (see Fig. 2.3). Assume that the total number density, n, of the identical particles remains constant and that the tagged particles number density,

denoted $n_T(z)$, will vary with z during the diffusion process. The tagged particles in dV will collide with each other at an average rate of

$$n_T(z)dV/\tau = \left(\frac{\lambda}{\lambda}\right)n_T(z)dV/\tau = \frac{\lambda}{\tau}\frac{n_T(z)}{\lambda}dV = n_T(z)\frac{\langle v\rangle}{\lambda}dV, \tag{2.49}$$

where τ is the mean free time (between collisions), λ is the mean free path (between collisions), and $\langle v\rangle$ is the average molecular velocity. The average molecular velocity

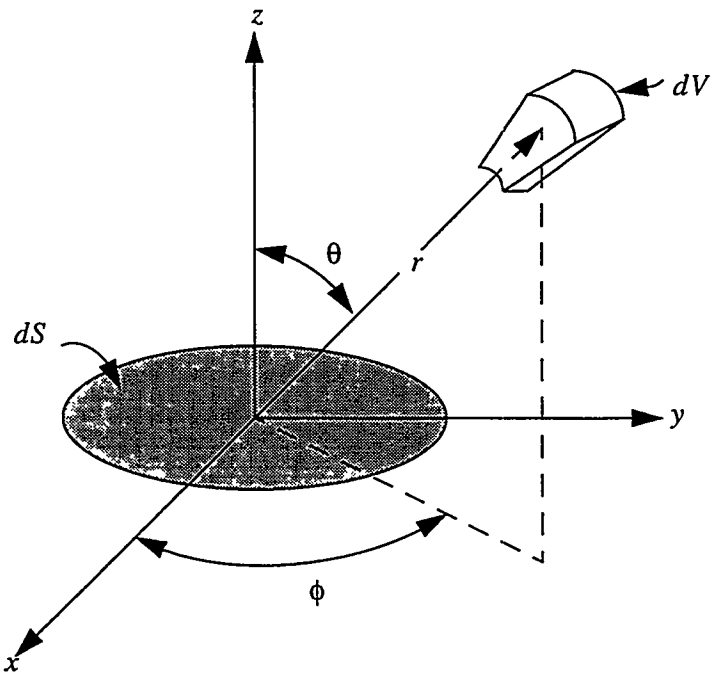

Fig. 2.3: *dS* and *dV* Coordinate System

The *xy*-plane defines our imaginary plane dividing the gas. *dS* is situated on top of the plane at the center of the coordinate system, and there is a net transport of particles across the plane as the particles diffuse throughout the system until the system reaches equilibrium.

is equivalent to the mean free path divided by the mean free time. With $d\Omega$ the solid angle subtended by dS,

$$d\Omega = \frac{dS|\cos\theta|}{r^2}. \tag{2.50}$$

(Then Eq. 2.50 is divided by 4π—the full angle—since calculating the fraction of particles scattered from dV across dS is needed.) The probability any tagged particle will reach dS from r, θ, and ϕ without undergoing a collision, P_{NC}, is

$$P_{NC}(r) = e^{-r/\lambda}, \tag{2.51}$$

where λ is the number of collisions per unit length—the mean free path. Putting Eqs. 2.49 to 2.51 together, the number of particles from dV reaching dS from $\vec{r}$ per unit time per unit area from the upper half plane, $\dot{N}_+(\vec{r})$, is

$$\dot{N}_+(\vec{r}) = \int_{\text{Upper Half Plane}} \left(n_T(z)\frac{\langle v\rangle}{\lambda}\right)\left(\frac{\cos\theta}{4\pi r^2}\right)e^{-r/\lambda}dV, \tag{2.52}$$

where

$$dV = r^2\sin\theta dr d\theta d\phi. \tag{2.53}$$

The number of particles reaching dS from the lower half plane, $\dot{N}_-(\vec{r})$, is similar,

$$\dot{N}_-(\vec{r}) = -\int_{\text{Lower Half Plane}} \left(n_T(z)\frac{\langle v\rangle}{\lambda}\right)\left(\frac{\cos\theta}{4\pi r^2}\right)e^{-r/\lambda}dV. \tag{2.54}$$

Except for the sign, and limits of integration over θ, these two results are identical. The difference of $\dot{N}_+$ and $\dot{N}_-$ gives the net flow of particles in the z-direction across dS:

$$\dot{N}_+ - \dot{N}_- = \int_0^\infty r^2 dr \int_0^\pi \sin\theta d\theta \int_0^{2\pi} d\phi \left(n_T(z) \frac{\langle \nu \rangle}{\lambda} \right) \left(\frac{\cos\theta}{4\pi r^2} \right) e^{-r/\lambda}. \tag{2.55}$$

The form of $n_T(z)$ is needed to integrate Eq. 2.55. If $n_T(z)$ is a slowly varying function (incompressible flow, for example), then $n_T(z)$ can be expanded in a Taylor series about z=0 and the terms in the expansion can be integrated. The Taylor series expansion is

$$n_T(z) = n_T(0) + \left(\frac{\partial n_T}{\partial z} \right)_{z=0} \frac{z}{1!} + \left(\frac{\partial^2 n_T}{\partial z^2} \right)_{z=0} \frac{z^2}{2!} + \left(\frac{\partial^3 n_T}{\partial z^3} \right)_{z=0} \frac{z^3}{3!} + \cdots \tag{2.56}$$

Three important points about Eqs. 2.55 and 2.56 are: (1) the probability function, $e^{-r/\lambda}$, in the integrand implies that only small values of z will contribute to the flow of particles across dS (because of the mean free path); (2) the form of the Taylor expanded number density convolved with the other terms in the integrand implies that only integration of the odd terms in the number density function will contribute to the particle flow; and (3) if the tagged particle number density is a slowly varying function of z, the higher order derivatives will be small and the integration can be terminated at the second-order derivative. Considering these three items,

$$\dot{N}_+ - \dot{N}_- = \left(\frac{\langle \nu \rangle \lambda}{3} \right) \left(\frac{\partial n_T}{\partial z} \right)_{z=0} + \vartheta \left(\frac{\partial^3 n_T}{\partial z^3} \right) \approx D \left(\frac{\partial n_T}{\partial z} \right)_{z=0}, \tag{2.57}$$

where D is the coefficient of self diffusion. If $\dot{N}_+$ is greater than $\dot{N}_-$, and if the partial derivative of the number density of the tagged particles is greater than zero, then there will be a net current of tagged particles in the negative z direction. Thus the flux of particles is defined as

$$J_v(z) = -D\frac{\partial}{\partial z}n_T(z). \tag{2.58}$$

For a tagged particle number density which varies in all directions,

$$\vec{J}_v(\vec{r}) = -D\nabla_{\vec{r}}n_T(\vec{r}). \tag{2.59}$$

Thus, the coefficient of self diffusion is proportional to the average molecular velocity times the mean free path.

2-3.3.2 Viscosity—The Diffusion of Momentum

Viscosity is the diffusion of momentum due to molecular forcings in a fluid system. Molecules will diffuse from regions of higher pressure to those of lower pressure. As this diffusion occurs, particles with higher velocities scatter into regions with lower particle velocities. Turbulence results in local variations in velocity which causes a velocity gradient. A diffusion of momentum results from the turbulence as faster moving eddies interact with slower moving eddies. Thus, a velocity gradient exists and the flux of particles is

$$\vec{J} = -\nu\nabla(\rho\vec{v}), \tag{2.60}$$

and by the continuity equation,

$$\frac{\partial}{\partial t}(\rho\vec{v}) = -\nu\nabla\cdot\nabla(\rho\vec{v}) = -(\rho\nu)\nabla^2\vec{v} \equiv -\eta\nabla^2\vec{v}, \tag{2.61}$$

where ν is the coefficient of kinematic viscosity and $\eta=\rho\nu$ is the coefficient of viscosity. (Eq. 2.61 is applicable to incompressible flow.) Dividing through by the density (for the case of incompressible flow) gives the acceleration,

$$\frac{\partial}{\partial t}\vec{v} = -\nu\nabla^2\vec{v}. \tag{2.62}$$

This term represents the viscous forcings and leads to the final equation of motion

$$\vec{a} = -\frac{\nabla p}{\rho} + \vec{g} - 2\vec{\omega}\times\vec{v} + \nu\nabla^2\vec{v}, \tag{2.63}$$

where

$$\nu \sim \frac{\lambda\langle v_{mol}\rangle}{3}. \tag{2.64}$$

Eq. 2.63 represents conservation of momentum for incompressible flow and is one of the Navier-Stokes equations.

2-3.3.3 Average Molecular Velocity

An ideal gas obeys Boltzmann statistics. Convolving the molecular velocity with the classical Boltzmann distribution, f_B, gives the average molecular velocity. The Boltzmann distribution, f_B, is

$$f_B(\varepsilon) \equiv \left(\frac{\mu}{2\pi k_B T}\right)^{\frac{3}{2}} e^{-\varepsilon/k_B T}, \tag{2.65}$$

where k_B is the Boltzmann constant, μ is the reduced mass for the particle system, and ε represents the total energy of the system. The average molecular velocity includes only the relative term in ε. In a dilute ideal gas the total energy of the system is equivalent to the kinetic energy of the system. Thus, the average molecular velocity is

$$\langle v_{mol} \rangle \equiv \left(\frac{\mu}{2\pi k_B T} \right)^{\frac{3}{2}} \int_{\forall} v e^{-\mu v^2 / 2k_B T} d\vec{v} = 4\pi \left(\frac{\mu}{2\pi k_B T} \right)^{\frac{3}{2}} \cdot \int_0^{\infty} v^3 e^{-\mu v^2 / 2k_B T} dv. \tag{2.66}$$

Integrating Eq. 2.66 by parts shows that the average molecular velocity of a Boltzmann (ideal) gas is proportional to the temperature of the gas, i.e.,

$$\langle v_{mol} \rangle = \sqrt{\frac{8kT}{\pi \mu}}. \tag{2.67}$$

2-3.4 Navier-Stokes

The Navier-Stokes equations represent the conservation of momentum, of mass, and of energy. The dynamics of atmospheres, and fluids in general, are thought to be governed by the Navier-Stokes equations.

2-3.4.1 Conservation of Mass

The total mass of a system is conserved if the system is closed such that no mass can be introduced or removed. Consider a flow of gas through a fixed imaginary box (Fig. 2.4) such that the rate at which particles enter the box is the rate at which particles leave the box, i.e., total mass is conserved. The flux through the box along the y-axis is

$$j_y = \rho v_y. \tag{2.68}$$

The difference per unit time of the mass flow through the xz-plane at $y=0$ and $y=\Delta y$ is defined as,

$$\frac{\Delta \rho}{\Delta t} = -\frac{\rho v_y(x, \Delta y, z) - \rho v_y(x, 0, z)}{\Delta y}. \tag{2.69}$$

If more mass leaves the box at $y=\Delta y$ than enters the box at $y=0$ implies an increase in mass per unit time (thus the minus sign). A similar result applies for mass flux through any of the xy, xz, or yz-planes. Take the appropriate limits as the differences approach zero, and find the equation for the conservation of mass, or the *continuity* equation

$$\frac{\partial \rho}{\partial t} + \nabla \cdot (\rho \vec{v}) = 0. \tag{2.70}$$

For incompressible flow, this reduces to

$$\nabla \cdot \vec{v} = 0. \tag{2.71}$$

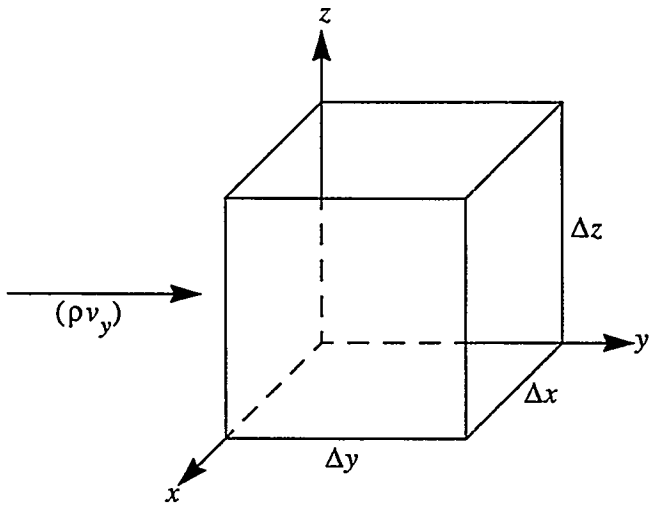

Fig. 2.4: Mass Flux Through a "Fixed Box"

The mass flux through any side of the box is ρv_i, $i=1,2,3$.

2-3.4.2 Conservation of Energy

The total energy of a system is conserved if the sum of the kinetic and potential energy in the system is constant—a positive change in the kinetic energy is equal and opposite to the change in the potential energy. The flux of energy in the system must consider the kinetic energy as well as the free energy of the hydrodynamic system. The independent thermodynamic variables determine the form of the free energy in the energy equation. The independent variables dictate the use of either the kinetic energy and the Helmholtz free energy, or the kinetic energy and the Gibbs free energy, etc. Thus, the flux of energy is

$$\vec{J}_\varepsilon = \left(\frac{1}{2}\rho v^2 + \rho u\right)\vec{v}, \tag{2.72}$$

where u is the internal energy per unit mass. Using the continuity equation for the energy

$$\frac{\partial}{\partial t}\left[\left(\frac{1}{2}v^2 + u\right)\rho\right] + \nabla \cdot \vec{J}_\varepsilon = 0. \tag{2.73}$$

Consider the components of the time derivative separately to find the differential of ρu,

$$d(\rho u) = u d\rho + \rho du = u d\rho + \rho\left(Tds + \frac{p}{\rho^2}d\rho\right) = h d\rho + \rho T ds, \tag{2.74}$$

where h is the enthalpy per unit mass. This implies

$$\frac{\partial}{\partial t}(\rho u) = h\frac{\partial \rho}{\partial t} + \rho T\frac{\partial s}{\partial t} = -h\nabla(\rho\vec{v}) - \rho T\vec{v}\cdot\nabla s. \tag{2.75}$$

Finally,

$$\frac{\partial}{\partial t}\left[\left(\frac{1}{2}v^2+u\right)\rho\right] = -\nabla\cdot\left[\rho\vec{v}\left(\frac{1}{2}v^2+h\right)\right], \tag{2.76}$$

and is the correct form for conservation of energy for an ideal fluid or gas (Landau 1987). Where the temperature is uneven throughout the parcel, consider thermal conduction of heat and the flux of energy due to frictional forcings. Thus,

$$\frac{\partial}{\partial t}\left[\left(\frac{1}{2}v^2+u\right)\rho\right] = -\nabla\cdot\left[\rho\vec{v}\left(\frac{1}{2}v^2+h\right)-\vec{v}\cdot\underline{\sigma}-\kappa\nabla T\right], \tag{2.77}$$

where κ is the coefficient of thermal conductivity and the additional term, a vector, accounts for frictional forcings. As mentioned earlier, it is also appropriate here to account for radiative processes such as the reflection of sunlight from the earth's surface.

In an experimental situation where measurements are acquired, the experimenter controls as many variables as possible. For example, the experimenter might attempt to acquire measurements from a system in a steady state situation which can be isolated from heat conduction, etc.

2-4 Discussion

Water is the engine which drives our atmosphere. Phase changes of water cause high and low pressure regions throughout the earth's atmosphere. Radiative interactions between the earth and sun heat the atmosphere and earth's surface causing the phase changes of water.

Winds carry mass from high pressure regions to low pressure regions, and the Coriolis force deflects those winds at right angles to the pressure gradient. The Coriolis force is negligible on horizontal motions near the equator which is why hurricanes, tropical storms, and typhoons do not originate within the tropics. Geostrophic winds result when the horizontal pressure gradients and the Coriolis forces balance each other. When this condition occurs winds follow lines of constant pressure—isobars. The geostrophic approximation is common in atmospheric modeling problems.

As mentioned in section 2-3.2, the hydrostatic approximation is often used for modeling the dynamical equation of motion (Eq. 2.63). The hydrostatic approximation assumes a balance between the vertical pressure gradient and the acceleration per unit mass.

In modeling the dynamical equations of motion for the atmosphere, modelers often separate the wind speed into an average component and a fluctuating component; derivatives are computed and the fluctuating components are then modeled using finite difference schemes. These models incorporate boundary conditions and initial conditions appropriate for the problem and use a variety of closure schemes and approximations together with the Courrant stability condition (Press et al. 1992).

Consider the acceleration on a parcel of air (Eq. 2.63), then

$$\vec{a} = \frac{d}{dt}\vec{v} \equiv \frac{\partial}{\partial t}\vec{v} + \vec{v} \cdot \nabla\vec{v}, \tag{2.78}$$

which is the transformation from a Lagrangian frame of reference to the Eulerian frame of reference. The velocity gradient term is called the Reynolds stress tensor. The dot product of the velocity and the Reynolds stress tensor, where the velocity can be written as $\vec{v} = ue_1 + ve_2 + we_3$, gives for the cartesian acceleration components

$$\begin{aligned}
&\left[\frac{\partial u}{\partial t} + u\frac{\partial u}{\partial x} + v\frac{\partial u}{\partial y} + w\frac{\partial u}{\partial z} = -\frac{1}{\rho}\frac{\partial p}{\partial x} - 2\omega v + \nu\nabla^2 u\right]e_1, \\
&\left[\frac{\partial v}{\partial t} + u\frac{\partial v}{\partial x} + v\frac{\partial v}{\partial y} + w\frac{\partial v}{\partial z} = -\frac{1}{\rho}\frac{\partial p}{\partial y} + 2\omega u + \nu\nabla^2 v\right]e_2, \\
&\left[\frac{\partial w}{\partial t} + u\frac{\partial w}{\partial x} + v\frac{\partial w}{\partial y} + w\frac{\partial w}{\partial z} = -\frac{1}{\rho}\frac{\partial p}{\partial x} + \nu\nabla^2 w\right]e_3.
\end{aligned} \tag{2.79}$$

Now multiply the e_1 component by ρ, the continuity equation by u, and add the two under the assumption of incompressible flow,

$$\left[\frac{\partial}{\partial t}(\rho u) + \frac{\partial}{\partial x}\left(\rho u^2\right) + \frac{\partial}{\partial y}(\rho uv) + \frac{\partial}{\partial z}(\rho uw) = -\frac{1}{\rho}\frac{\partial p}{\partial x} - 2\omega v + \nu\nabla^2 u\right]e_1. \tag{2.80}$$

Similarly, for the e_2 component

$$\left[\frac{\partial}{\partial t}(\rho v) + \frac{\partial}{\partial x}(\rho uv) + \frac{\partial}{\partial y}\left(\rho v^2\right) + \frac{\partial}{\partial z}(\rho vw) = -\frac{1}{\rho}\frac{\partial p}{\partial y} + 2\omega u + \nu\nabla^2 v\right]e_2. \tag{2.81}$$

And, by analogy for the e_3 component

$$\left[\frac{\partial}{\partial t}(\rho w) + \frac{\partial}{\partial x}(\rho uw) + \frac{\partial}{\partial y}(\rho vw) + \frac{\partial}{\partial z}\left(\rho w^2\right) = -\frac{1}{\rho}\frac{\partial p}{\partial z} + g + \nu\nabla^2 w\right]e_3. \tag{2.82}$$

Apply the assumption of average velocity components with fluctuating components and an appropriate average, and collect the remaining terms for the individual components. The equations of motion can then be expressed in the form of Eq. 2.79 with an additional term to account for the fluctuations about the average. The e_1 component is

shown in Eq. 2.83 where the barred terms on the left side of the equation represents an equation of motion for the average component and the barred and primed coordinates on the right side of the equation represents the equation of motion for the fluctuating e_1 component. The e_2, and e_3 components can be expressed similarly.

$$\left(\frac{\partial}{\partial t}\bar{u} + \bar{u}\frac{\partial}{\partial x}\bar{u} + \bar{v}\frac{\partial}{\partial y}\bar{u} + \bar{w}\frac{\partial}{\partial z}\bar{u} + \frac{1}{\rho}\frac{\partial p}{\partial x} + 2\omega\bar{v} - \nu\nabla^2\bar{u}\right)e_1 = \tag{2.83}$$
$$-\frac{1}{\rho}\left(\frac{\partial}{\partial x}\rho\overline{u'u'} + \frac{\partial}{\partial y}\rho\overline{u'v'} + \frac{\partial}{\partial z}\rho\overline{u'w'}\right)e_1.$$

Express the fluctuating components in analogy with the molecular viscosity terms (Houghton 1986), i.e.,

$$\rho\overline{u'v'} \approx -\rho\nu_T\frac{\partial}{\partial x}\bar{u}, \tag{2.84}$$

where ν_T is the coefficient of kinematic eddy viscosity. This leads to

$$\frac{\partial}{\partial t}\langle\vec{v}\rangle + \langle\vec{v}\rangle\cdot\nabla\langle\vec{v}\rangle = -\frac{1}{\rho}\nabla p - 2\vec{\omega}\times\langle\vec{v}\rangle + (\nu+\nu_T)\nabla^2\langle\vec{v}\rangle + \vec{g},$$
$$\Leftrightarrow \frac{d}{dt}\langle\vec{v}\rangle = -\frac{1}{\rho}\nabla p - 2\vec{\omega}\times\langle\vec{v}\rangle + \nu(1+Re)\nabla^2\langle\vec{v}\rangle + \vec{g}, \tag{2.85}$$

where the brackets (as opposed to the bars) now represent the average quantities.

This is the approach most often used in modeling the dynamics in the atmospheric boundary layer. Eq. 2.84 describes first-order closure. The ratio of the kinematic eddy viscosity to the kinematic viscosity is the Reynolds number, *Re*. When *Re* is less than about 10^3, viscosity dominates flows; when *Re* is greater than 10^3, flows are turbulent. *Re* is proportional to an average velocity times a length scale—in this case, a turbulent length scale, λ_T, such as those of turbulent eddies in the boundary

layer. Considering an average velocity of 10 m/s and eddy-scale sizes on the order of 10^2 m, then the kinematic viscosity is on the order of 10^3 m^2/s or less. Division by 3 for the kinematic viscosity gives eddy viscosities on the order of 10^2 m^2/s, which is the generally accepted order of magnitude. In developing algorithms to extract wind information from lidar data within the atmospheric boundary layer, I assumed turbulent length scales on the order of 10^2 m.

Atmospheric modelers do use higher orders of closure for some models, but most atmospheric models use the first-order closure scheme. Second-order closure is used to model sub-grid scale processes to account for motions on smaller scales than the modeling grid size.

References

Baierlein, R., "Newtonian Dynamics," by McGraw-Hill, Inc. (1983).

Brutsaert, W., "Evaporation of Water into the Atmosphere," by Klewer Academic Publishers (1982).

Buttler, W. T., W. E. Eichinger, C. G. Lebeda, D. I. Cooper, and J. Moses, "Barcelona Air Quality Initiative," *Alliance For Transportation Research Project Document*, No. ATR 94-1 (1994).

Houghton, J. T., "The Physics of Atmospheres, Second Edition," by Cambridge University Press (1986).

Kennard, E. H., "Kinetic Theory of Gases," by the McGraw-Hill Book Company, Inc. (1938).

Landau, L. D., and E. M. Lifshitz, "Fluid Mechanics (2nd Edition)," *Course of Theoretical Physics*, Vol. 6, by Pergamon Press plc. (1987).

Press, W. H., S. A. Teukolsky, W. T. Vetterling, and B. P. Flannery, "Numerical Recipes in FORTRAN: The Art of Scientific Computing (Second Edition)," by Cambridge University Press (1992).

Reichl, L. E., "A Modern Course in Statistical Physics," by the University of Texas Press (1980).

Stull, R. B., "An Introduction to Boundary Layer Meteorology," by Klewer Academic Publishers (1988).

Sommerfeld, A., "Thermodynamics and Statistical Mechanics," *Lectures on Theoretical Physics*. Vol. V, Printed by Academic Press, Inc. (1956).

Suggested Reading

Batchelor, G. K., "An Introduction to Fluid Dynamics," by Cambridge University Press (1967).

Evans, H. L., "Laminar Boundary-Layer Theory," by Addison-Wesley Publishing Company, Inc. (1968).

Ghil, M., and S. Childress, "Topics in Geophysical Fluid Dynamics: Atmospheric Dynamics, Dynamo Theory, and Climate Dynamics," *Applied Mathematical Sciences*, Vol. 60, by Springer-Verlag New York, Inc. (1987).

McIlveen, R., "Fundamentals of Weather and Climate," by Chapman and Hall (1992).

3

Lidar as an Atmospheric Probe

The four basic elastic-backscatter lidar scanning patterns or data acquisition algorithms are correlation scans, time-domain scans, and three and two-dimensional scans. These are used to interrogate and obtain information within the planetary boundary layer—often called the *convective mixed layer* (Stull 1988), the *atmospheric boundary layer* Brutsaert 1982), and the *turbulent boundary layer* (Landau 1987).

3-1 Two-Dimensional Scans

Fix either the azimuthal or vertical angle and raster the lidar system in the other angle to acquire a two-dimensional scan. For example, fix the lidar's azimuthal angle and raster the lidar with regular angular steps in the vertical dimension to acquire a two dimensional vertical scan. Conversely, fix the lidar's vertical angle and raster the lidar with regular angular steps in the horizontal dimension to acquire a two-dimensional horizontal scan.

3-1.1 Horizontal Scans

Horizontal scans can reveal trends in aerosol transport, such as direction of flow, as well as pinpoint sources of aerosols and the distribution of aerosols in the horizontal dimension. A horizontal scan can show the direction of flow to a relative accuracy of ±180°. Flow is probably from the SE in Fig. 3.1 because the plumes visible in this scan are thinner and more intense (red colors are more intense than blue colors) at the SE corner of the scan than in the NW corner of the scan. The results of correlation wind scans support this assumption (Ch. 5).

3-1.2 Vertical Scans

Vertical scans contain information about the structure of the planetary boundary layer (Fig. 3.2). A sudden decrease in backscattered power as the laser beam passes from the less clean air of the mixed layer into cleaner air above identifies the top of the mixed layer. An increased return power followed by another decrease in return power above the mixed layer identifies a residual layer. More than one residual layer may be present. Finally, a sudden decrease in backscatter return to the noise level of the detector identifies the free atmosphere. Clouds sometimes form in the entrainment zone between the mixed layer and the free atmosphere. Large increases in the magnitude of the range-corrected returns in lidar data signify clouds.

Vertical profiles of lidar data are nearly constant with height within the mixed layer but exceptions do occur. For example, Fig. 3.2 shows clean air between convec-

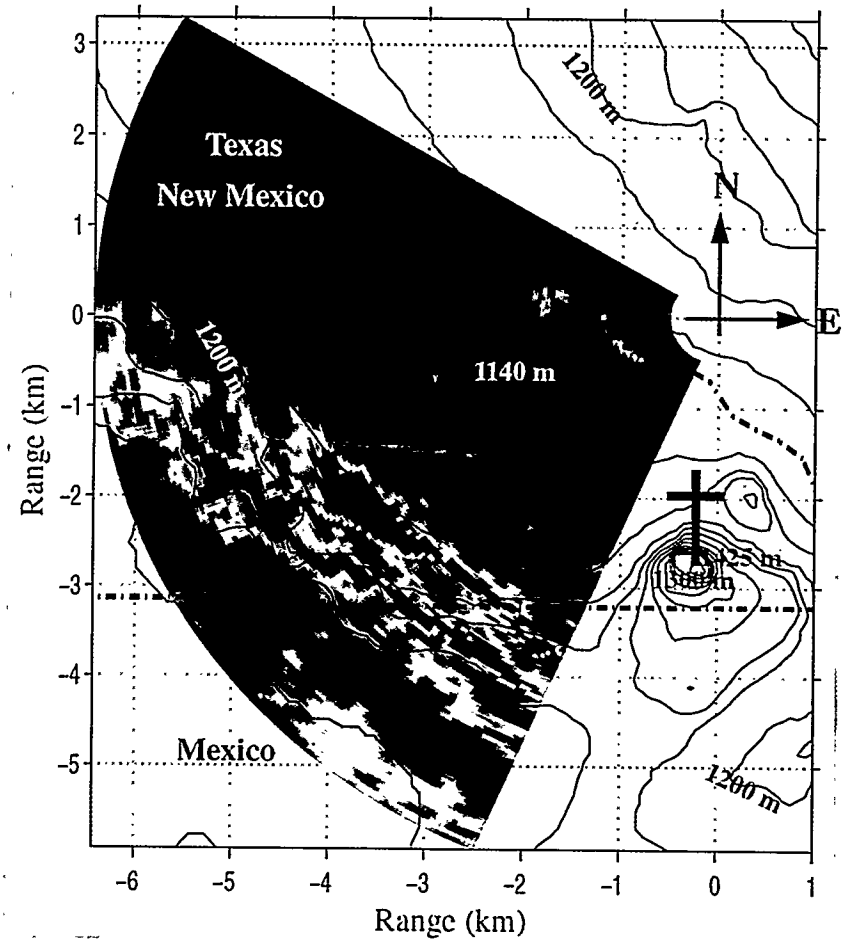

Fig. 3.1: Horizontal Scan

This horizontal scan was acquired at ~9 am on September 11, 1995, at Sunland Park, New Mexico. The scan is plotted on a topographic map of the Mexico, New Mexico, and Texas border area. (The topographic map was generated from a digital elevation map provided by the United States Geological Survey.)

The cross identifies Sierra de Cristo Rey peak. The Franklin Mountains lie to the northeast of the plot and the Sierra Juarez are about 7 km south of Sierra de Cristo Rey. The lidar is positioned at zero km north and zero km east. Red colors correspond to high backscatter-return power and blue colors correspond to low backscatter-return power.

Large amounts of aerosols were seen flowing into New Mexico from Ciudad Juarez, Mexico, and El Paso, Texas. Aerosols from El Paso generally follow the Rio Grande river which closely tracks the Texas/New Mexico border while the aerosols from Mexico are flowing across the plain between Sierra de Cristo Rey and Sierra Juarez.

tive plumes penetrating the mixed layer top. One plume extends to the cloud bottom by more than one km above the convective plume. The extended plume could be a mixed layer penetrating thermal caused by thermodynamic processes occurring in the cloud. Cloud thermals can pull boundary layer aerosols to high altitudes.

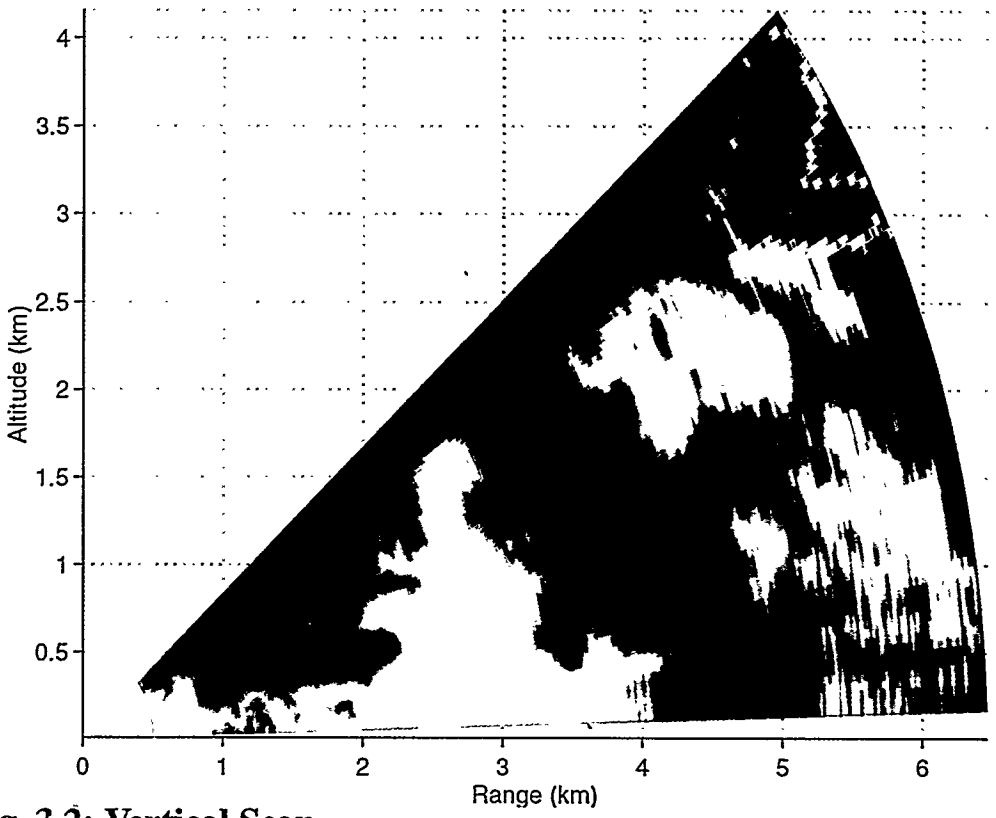

Fig. 3.2: Vertical Scan

This scan shows a well developed mixed layer with a cloud at the top of the planetary boundary layer. No residual layer is visible and the mixed layer reveals a convective thermal entraining cleaner air from the free atmosphere above into the mixed layer below. Also, a plume extends to a cloud at 3 km altitude. The cloud may be drawing the plume up. The mechanism for such a process could be water condensation in the cloud which releases heat and causes turbulence leading to an updraft.

This scan reveals the poorly defined nature of the "top" of the mixed layer/boundary layer. Cloud backscatter returns were two orders of magnitude higher than mixed layer returns. The cloud returns were set to a magnitude of 5.0 dimensionless units so that the mixed layer structure could be observed.

Strong correlations between relative humidity and vertical profiles of range-corrected lidar data have been observed within the boundary layer (Soriano et al. 1995). Fig. 3.3 shows a vertical profile extracted from the vertical scan seen in Fig. 3.2. This vertical profile coincides with the cloud thermal and does not clearly identify the depth of the mixed layer. The cloud bottom does identify the top of the boundary layer, however.

3-2 Three-Dimensional Scans

Three-dimensional scans can be acquired in two unique ways: (1) sequential vertical scans acquired at regular azimuthal intervals (fixing the lidar at different azimuthal angles and rastering through the elevation angles); or (2) sequential horizontal scans acquired at regular elevation angles (fixing elevation angles and rastering the

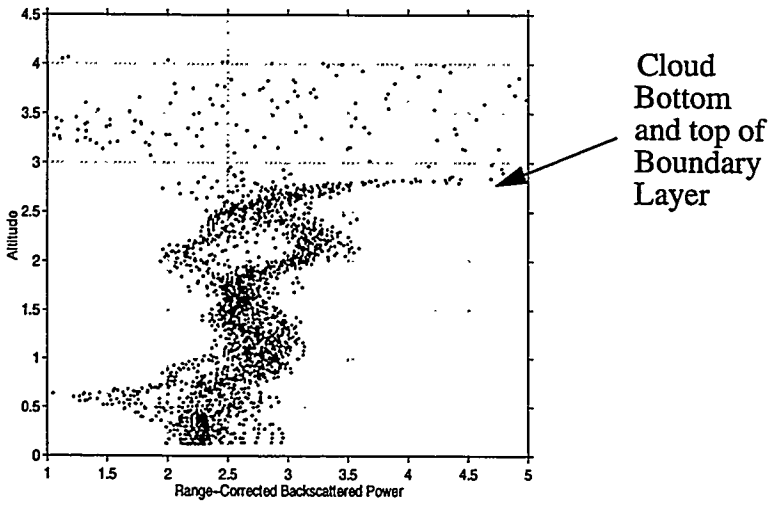

Fig. 3.3: Vertical Profile

Returns from the cloud were two orders of magnitude larger than the aerosol returns plotted here. This image shows a nearly constant with height corrected returns from the aerosols within the mixed layer.

lidar in the horizontal dimension). Three-dimensional scans are often visualized with semi-transparent colored iso-surfaces, in slices, or as semi-transparent colored spheres related to backscattered power or aerosol densities.

Three-dimensional scans contain information about the distribution of aerosols in the horizontal and vertical dimension. During the past few years, scientists at the University of Wisconsin at Madison have used three-dimensional scans to measure winds in the planetary boundary layer (Schols et al. 1992).

3-3 Time-Domain Scans

Fixing both the azimuth and elevation angles and acquiring data at those fixed angles for some duration of time is used to acquire time-domain data. Time-domain scans record aerosol motion toward or away from the lidar much like doppler-lidar devices. Doppler-type lidars measure radial winds, and scanning the doppler device in a circular pattern above the lidar system is used to measure vertical wind profiles. Such scanning patterns result in doppler data acquired on a conical surface. The maximum doppler shift toward or away from the doppler lidar system is used to infer wind direction and speed. The Physical Science Laboratory (PSL) of Las Cruces, New Mexico, uses this type of lidar system (often referred to as a Laser-Doppler Velocimeter [LDV]). The PSL provided their LDV for ground truth during the Border Area Air-Quality Study.

3-4 Correlation Scans

Repetitively rastering the lidar for some duration of time between two or three different azimuthal angles acquires a correlation scan. The resulting data base gives the motion of aerosols between the two or three lidar-observation angles. The observation angles are predetermined and a small angle separates the azimuths. The azimuthal separation between adjacent observation angles determines the duration of data acquisition. The time duration is chosen such that a 1 m/s cross-wind can be observed at roughly 6-km range from the lidar system. Correlation scans are used to measure three-dimensional winds in the planetary boundary layer. Three-dimensional winds are horizontal winds as a function of range and altitude. The correlation scanning pattern yields a time-domain scan at each of the azimuthal angles.

Fig. 3.4 shows a correlation scan acquired at Sunland Park, New Mexico in September 1994. Many of the features which allow the measurement of winds are seen in the correlation scan (Fig. 3.4).

3-5 Summary

Elastic-backscatter lidar techniques use several scanning patterns to extract information within the planetary boundary layer. Vertical scans are used to extract information about residual layers and the mixed layer depth. The depth of the mixed layer, in the strict constructionist definition of the boundary layer, equates to the depth of the planetary boundary layer. Atmospheric modelers are most interested in this

boundary layer depth since most hydrostatic and nonhydrostatic atmospheric models predict the average mixed layer depth. Correlation scans are used to estimate the three-dimensional velocity field within the boundary layer and residual layers. Horizontal

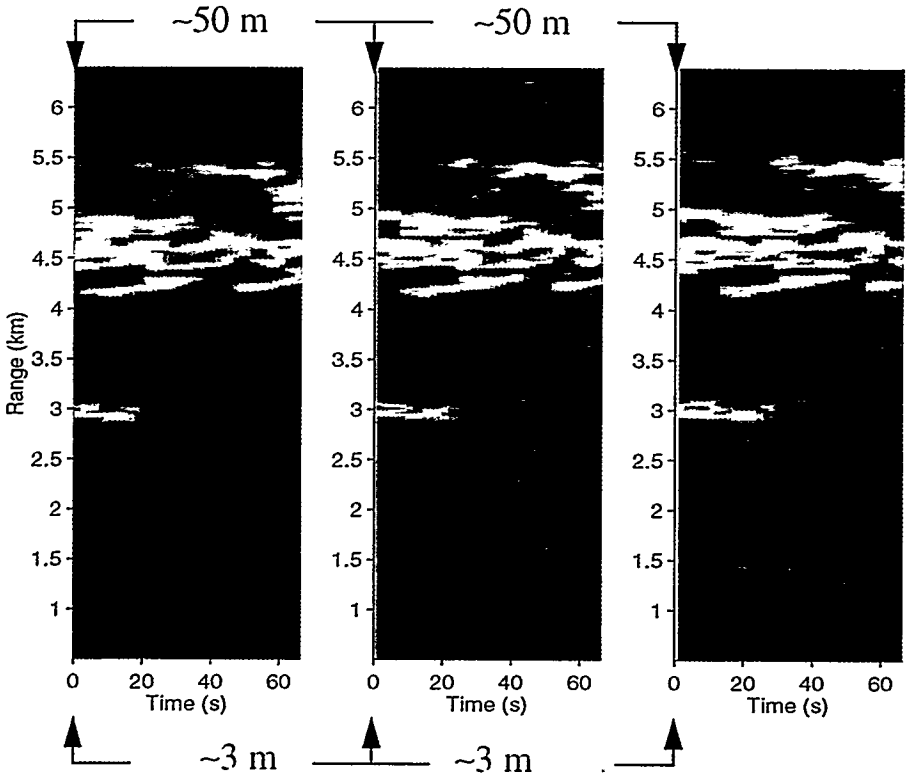

Fig. 3.4: Correlation Scan

This three-angle correlation scan was acquired at 7:47 am on September 11, 1994 at Sunland Park, New Mexico, and reveals many of the aerosol features which can lead to strong correlations between different lidar observation angles. This scan was acquired at an elevation angle of 1.5°. The angular separation between the three observation angles is 0.45°. This angle was chosen such that a 1 m/s cross wind could be observed at a range of 7 km from the lidar.

As mentioned earlier, a three-angle correlation scan contains three unique time-domain scans—one time-domain scan at each of the observation angles. Since the time-domain scans are spatially separated, the correlation scans record the motion of aerosols between the different observation angles or lines of sight. Also, range data at each angle are acquired sequentially, and not concurrently, since repetitively rastering the lidar system between the different observation angles constructs the scans.

scans are used to locate sources of aerosol introduction into the mixed layer and to identify general trends in aerosol transport.

References

Brutsaert, W., "Evaporation of Water into the Atmosphere," by Klewer Academic Publishers (1982).

Landau, L. D., and E. M. Lifshitz, "Fluid Mechanics (2nd Edition)," *Course of Theoretical Physics*, Vol. 6, by Pergamon Press plc. (1987).

Schols, J. L. and E. W. Eloranta, "Calculation of Area Averaged Vertical Profiles of the Horizontal Wind Velocity From Volume-Imaged Lidar Data," *Journal of Geophysical Research*, Vol. 97, No. D17 (1992).

Soriano, C., W. T. Buttler, and J. M. Baldasano, "Comparison of Temperature and Humidity Profiles With Elastic Backscatter Lidar Data," *Air Pollution III*, Vol. 2, Air Pollution Engineering and Management (1995).

Stull, R. B., "An Introduction to Boundary Layer Meteorology," by Klewer Academic Publishers (1988).

United States Geologic Survey (USGS), 1.800.USA.MAPS; Digital Elevation Map Site: "Anonymous FTP: edcftp.cr.usgs.gov." The digital elevation map (DEM) used in this thesis can be found in "pub/data/DEM/250/E/el_paso-w.gz" at the anonymous ftp site listed above. The USGS 7.5 minute DEMs are in compressed "gzip" free-ware format.

4

Maximum Cross-Correlation

Cross-correlation is a measure of the deviation about the mean between two sequences (ordered sets) of data. When one sequence lags another, the maximum correlation between the sequences occurs at the separation (delay or lag) between the sequences. For example, the lag between $cos(\omega t)$ and $-sin(\omega t)$ is $\Delta t=\pi/(2\omega)$ seconds since $cos(\omega(t-\Delta t))=-sin(\omega t)$.

Correlation coefficients are used to determine the lag between two sequences, The correlation coefficient, γ, is

$$\gamma \equiv \frac{\sum_r (A(r) - \langle A(r)\rangle)\ (B(r) - \langle B(r)\rangle)}{\sqrt{\left[\sum_r (A(r) - \langle A(r)\rangle)^2\right] \times \left[\sum_r (B(r) - \langle B(r)\rangle)^2\right]}}, \tag{4.1}$$

where γ gives an estimate of the similarity of sequence $A(r)$ and sequence $B(r)$. ($\langle A(r)\rangle$ and $\langle B(r)\rangle$ imply average values.) Dividing by the square root of the product of the sum of the elements of sequence $A(r)$ (minus its average) squared and the sum of the

ments of sequence $B(r)$ (minus its average) squared normalizes the result of the correlation between the sequences to a range of values between ± 1. A cross-correlation of $+1$ indicates that two correlated sequences are similar. A correlation of -1 indicates that two correlated sequences are similar, but negative to each other. (Note, a correlation coefficient is a number calculated between sequences of the same cardinality, i.e., sequences possessing the same number of elements.)

4-1 One-Dimensional Cross-Correlation

A correlation function, $\gamma_{n'}$, is constructed by calculating partial correlations between overlapping sub-range of the elements of two sequences as one sequence is slipped (slid or indexed) through the other (n' corresponds to the lag between the two sequences). If the cardinality of the sequences used to calculate $\gamma_{n'}$ is n, then the cardinality of the correlation function will be $2n - 1$, with $(1 - n) \leq n' \leq (n - 1)$.

Eqs. 4.2 to 4.5 demonstrate an algorithm to calculate a one-dimensional cross-correlation between two sequences. The one-dimensional cross-correlation function ($\gamma_{n'}$) is calculated by use of Eqs. 4.2 to 4.5. The function is a sequence of numbers relating similarities between overlapping sub-range of two one-dimensional sequences. Eqs. 4.2 and 4.5 are single numbers; Eq. 4.3 is a sequence of $n - 1$ correlation coefficients; Eq. 4.4 is a sequence of $n - 2$ correlation coefficients.

(4.2) $$\gamma_{1-n} = sign(f_n) \cdot sign(g_1),$$

$$(4.3)\qquad \gamma_{n'} = \left\{ \frac{\sum_{i=1}^{n'+n} (f_{n-i+1} - \langle f \rangle)(g_{n'+n-i+1} - \langle g \rangle)}{\sqrt{\sum_{i=1}^{n'+n} (f_{n-i+1}^2 - \langle f \rangle^2)} \sqrt{\sum_{i=1}^{n'+n} (g_i^2 - \langle g \rangle^2)}} \right\}, (2-n \le n' \le 0),$$

$$(4.4)\qquad \gamma_{n'} = \left\{ \frac{\sum_{i=1}^{n-n'} (f_i - \langle f \rangle)(g_{i+n'} - \langle g \rangle)}{\sqrt{\sum_{i=1}^{m} (f_i^2 - \langle f \rangle^2)} \sqrt{\sum_{i=1}^{m} (g_{i+n'}^2 - \langle g \rangle^2)}} \right\}, (1 \le n' \le n-2),$$

$$(4.5)\qquad \gamma_{n-1} = sign(f_1) \cdot sign(g_n),$$

Calculate the numerator in Eqs. 4.3 and 4.4 by use of the equivalent relation in Eq 4.6, and calculate the denominator in Eqs. 4.3 and 4.4 by use of the equivalent relation in Eq. 4.7.

$$(4.6)\qquad \sum_{i=1}^{m} (f_{n-i+1} - \langle f \rangle)(g_{m-i+1} - \langle g \rangle) \Leftrightarrow \sum_{i=1}^{m} \left(f_{n-i+1} - \frac{1}{m} \sum_{i=1}^{m} f_{n-i+1} \right) g_{m-i+1}.$$

$$(4.7)\qquad \sum_{i=1}^{m} (f_i - \langle f \rangle)^2 = \sum_{i=1}^{m} (f_i^2 - 2\langle f \rangle f_i + \langle f \rangle^2) \Leftrightarrow \sum_{i=1}^{m} \left(f_i^2 - \left(\frac{1}{m} \sum_{i=1}^{m} f_i \right)^2 \right).$$

The averages in the calculation are the sequence averages within the overlapped region. The correlation function, $\gamma_{n'}$, for the two sequences f_n and g_n (seen in Fig. 4.1) is shown in Fig. 4.2.

The magnitude of the first and last few elements of $\gamma_{n'}$ are very near one and illustrate a problem with this one-dimensional calculation. These first and last few elements must be ignored to recover the correct lag between sequences f_n (Fig. 4.1A) and g_n (Fig. 4.1B). Ignoring the first and last few elements of the correlation sequence

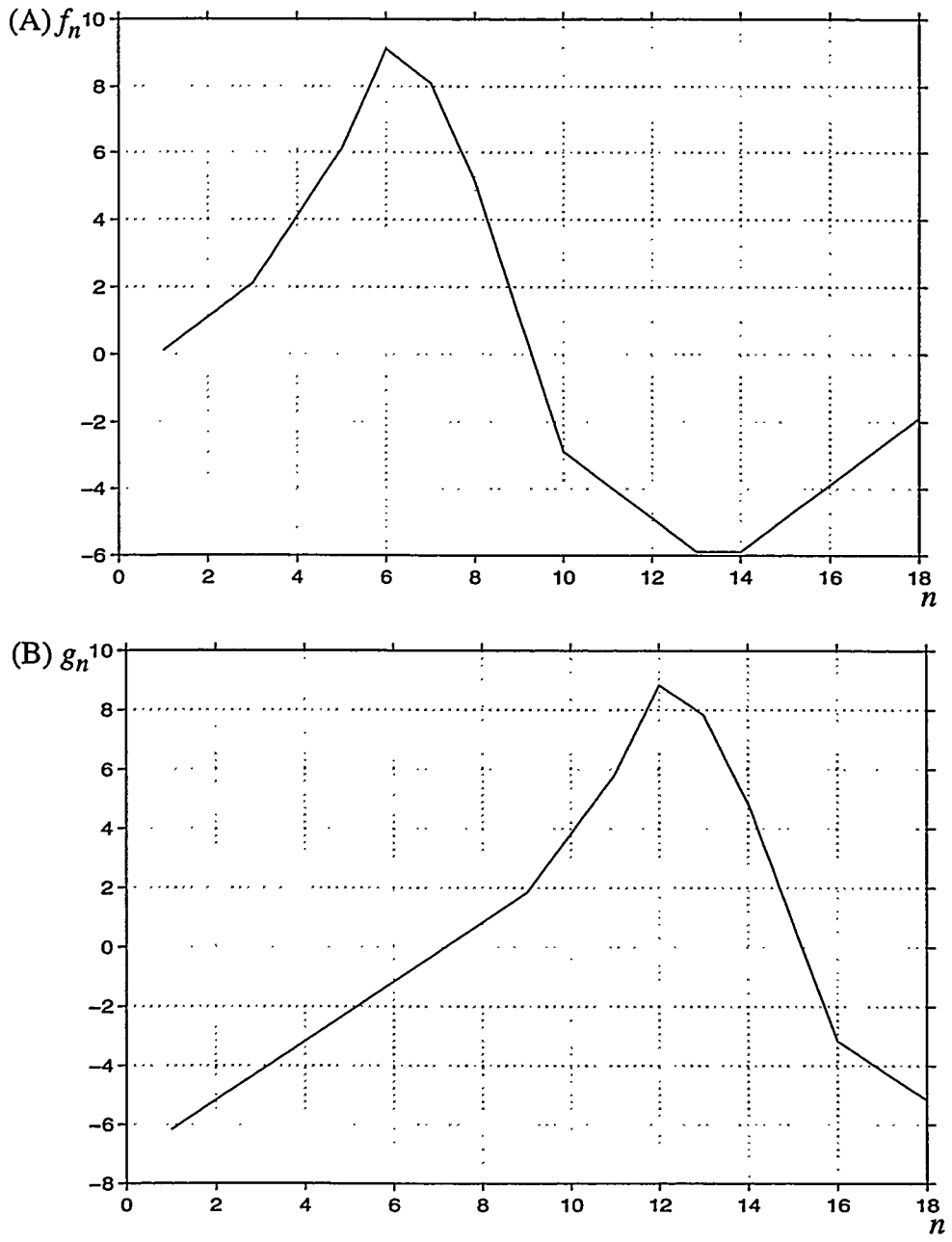

Fig. 4.1: Distributions f_n and g_n.

(A) f_n = {1, 2, 3, 5, 7, 10, 9, 6, 2, -2, -3, -4, -5, -5, -4, -3, -2, -1} - 1/9.

(B) g_n = {-5, -4, -3, -2, -1, 0, 1, 2, 3, 5, 7, 10, 9, 6, 2, -2, -3, -4} - 7/6,

where n = {1, 2, ..., 17, 18}.

shows that g_n lags sequence f_n by six bins. Prog. 4.1 is the computer program used to calculate the cross-correlation sequence, $\gamma_{n'}$ (Fig. 4.2). This algorithm can be extended to two dimensions to calculate a two-dimensional cross-correlation function.

4-2 One-Dimensional Maximum Cross-Correlation

Maximum cross-correlation is a variation of the cross-correlation algorithm presented in section 4-1. Maximum cross-correlation partitions one of the sequences being correlated into sub-sequences (hereafter called *kernels* denoted by κ). The cardinality of a kernel is predetermined and is less than the cardinality of the sequences being correlated. Kernel selection can be arbitrary or based on some statistical prop-

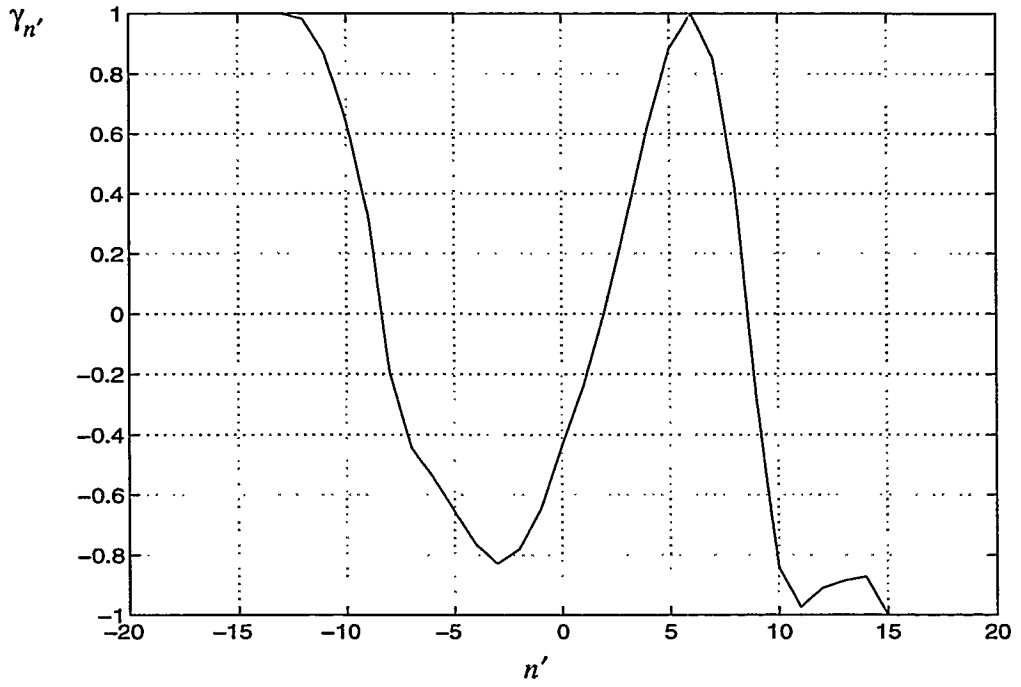

Fig. 4.2: 1-d Correlation Function or Lag Distribution, $\gamma_{n'}$, between f_n and g_n.

The first and last few channels must be rejected to recover the appropriate lag of six bins between distribution f_n, (Fig. 4.1A) and g_n (Fig. 4.1B).

erty of the subsequences such as their variances. The sequence from which kernels are chosen is called the *kernel space*, K. The remaining sequence is called the *search space*, Σ.

After choosing a kernel, κ, from the kernel space, K, the kernel is slid or indexed through the remaining sequence and correlation coefficients between the kernel (κ) and search space sub-sequences (σs) centered on the index bin are calculated and stored in a lag-vector (the σ–κ lag-vector). After κ has been indexed through Σ, the cross-correlation function (sequence), or σ–κ lag-vector, is complete. The maxi-

```
%    This program calculates the 1-D correlation function for the two
%    distributions
%
f = [1 2 3 5 7 10 9 6 2 -2 -3 -4 -5 -5 -4 -3 -2 -1];
g = [-5 -4 -3 -2 -1 0 1 2 3 5 7 10 9 6 2 -2 -3 -4];
n = length(f);
gamma = zeros(1,2*n-1);
for i = 1:n
   p = f(n+1-i:n) - mean(f(n+1-i:n));
   q = g(1:i) - mean(g(1:i));
   gamma(i) = sum(p.*q)/sqrt(sum(p.*p)*sum(q.*q));
   p = g(n+1-i:n) - mean(g(n+1-i:n));
   q = f(1:i) - mean(f(1:i));
   gamma(2*n-i) = sum(p.*q)/sqrt(sum(p.*p)*sum(q.*q));
end
f = f - mean(f);
g = g - mean(g);
gamma(n) = sum(f.*g)/sqrt(sum(f.*f)*sum(g.*g));
```

Prog. 4.1: One-Dimensional Correlation Function

This computer program is written in the matlab computer language, and it illustrates the algorithm to compute the one-dimensional correlation function for the functions *f* and *g*.

mum value in the σ–κ lag-vector corresponds to the best kernel and search space sub-sequence match. The lag associated with the maximum gives the delay between κ and Σ.

Consider the application of the maximum cross-correlation method to the sequences f_n and g_n (Fig. 4.1). Fig. 4.3 shows K (sequence f_n) and a κ. Sequence g_n and Σ are equivalent. (More than one κ can be selected from K and correlated with Σ.) The kernel shown in Fig. 4.3 is centered on bin number 4. The first sub-sequence, σ_0, chosen from Σ has the same cardinality as κ (seven) and is centered on bin number 4. Calculate the correlation between κ and σ_0 and store it in the *zero* lag position of the σ–κ lag-vector. Next, choose another sub-sequence, σ_1, from Σ (σ_1's cardinality remains unchanged, but now it is centered on bin number 5). Calculate the correlation between κ and σ_1 and store it in the +1 lag position of the σ–κ lag-vector. Repeat this procedure until all possible correlations between the κ and Σ sub-sequences are calculated. The maximum value or maximum cross-correlation in the σ–κ lag-vector determines the delay between κ and Σ sub-sequences (σ_is).

Fig. 4.4 shows the σ–κ lag-vector for this example. A correlation of 100% between κ and Σ sub-sequences was observed at a lag of +6 bins. High correlations in the first 5 channels are caused by the similarity of the slope of the first 12 Σ channels (see Fig. 4.1B) with the slope of the first 4 κ channels (Fig. 4.4). Prog. 4.2 is the program used to calculate the maximum cross-correlation function.

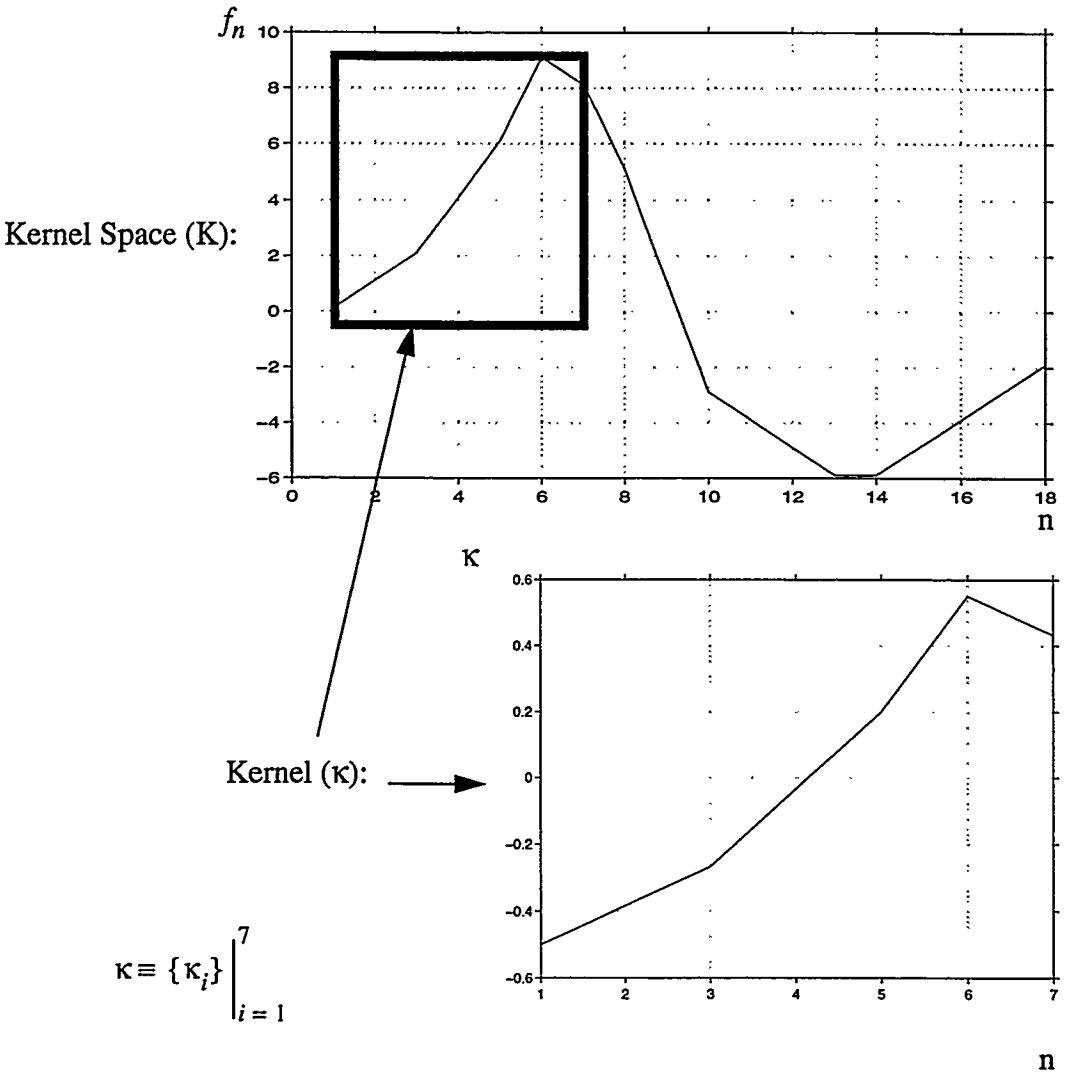

Fig. 4.3: Kernel Space and Kernel

The kernel, κ, is selected from the kernel space, f_n, and is defined so that its average is zero. It is normalized by dividing its elements by the square root of the sum of the elements minus the average of the elements. In this example, the cardinality of κ was seven.

4-2.1 One-Dimensional Correlation Summary

Correlation is a measure of the similarity between two data sequences. A correlation of +1 indicates the sequences are similar, and a correlation of −1 indicates that the sequences are similar but negative to each other.

Fig. 4.2 shows the one-dimensional correlation function (sequence) for distributions f_n and g_n (Fig. 4.1). This calculation was shown to be a poor predictor of the lag (delay) between two sequences unless the first and last few correlations are

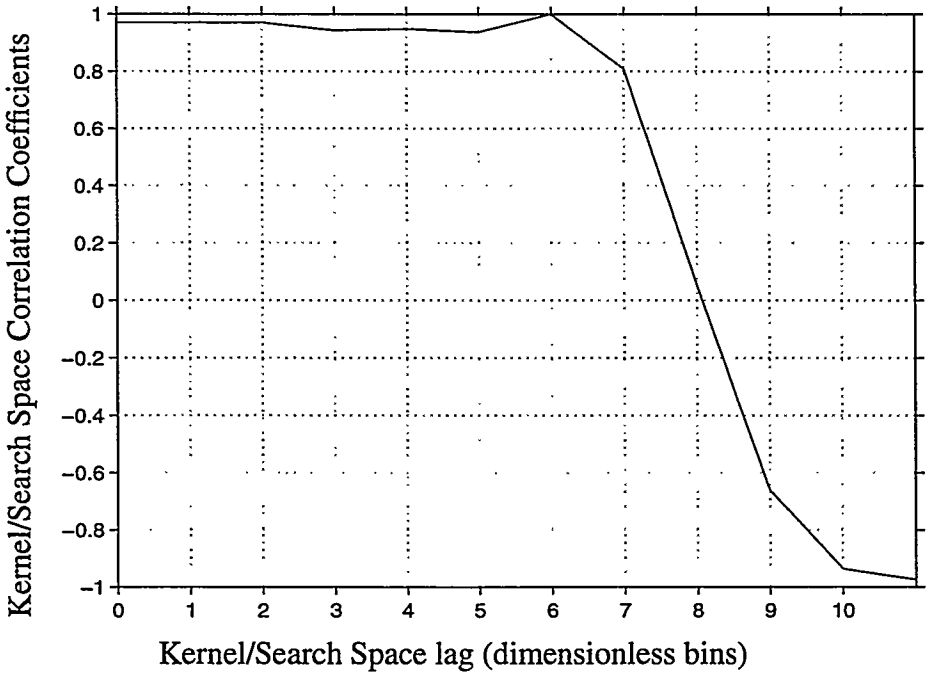

Fig. 4.4: σ–κ Lag-Vector

The lag-vector shown above corresponds to correlations between the kernel, K_n, and the search space, g_n. The lag-vector shows that the search space lags the kernel by +6 bins with a 100% correlation. To determine if the search space negatively lagged the kernel, it would have been necessary to select a kernel from the opposite end of the kernel space, i.e., from the last 7 kernel space bins.

ignored. Often, the biased correlation function (Bendat et al. 1971) is used to estimate the lag between two sequences. The biased function is normalized by dividing the correlation function by the number of elements in each sequence (as opposed to division by the product of the square root of the sum of the squares of the sequences). The biased calculation can give the lag between two sequences, but it fails to predict the degree of similarity between the sequences.

```
%     Select the kernel, average it to zero, and normalize it by the
%     square root of the sum of its squares.
%
f = [1 2 3 5 7 10 9 6 2 -2 -3 -4 -5 -5 -4 -3 -2 -1];
g = [-5 -4 -3 -2 -1 0 1 2 3 5 7 10 9 6 2 -2 -3 -4];
kernel_size = 7;
kernel = f(1:kernel_size);
kernel = kernel - mean(kernel);
kernel_norm = sqrt(sum(kernel.*kernel));
kernel = kernel/kernel_norm;
%     Get the lag-vector.
%
lag_vector = zeros(1,length(g)-kernel_size+1);
for i = 1:length(g)-kernel_size+1
  sub_image = g(i:i+kernel_size-1);
  sub_image = sub_image - mean(sub_image);
  sub_image_norm = sqrt(sum(sub_image.*sub_image));
  sub_image = sub_image/sub_image_norm;
  gamma = sum(kernel.*sub_image);
  lag_vector(i) = gamma;
end
```

Prog. 4.2. One-Dimensional Maximum Cross-Correlation Function

This computer program is written in the matlab computer language, and it illustrates the algorithm to compute the one-dimensional correlation function for the functions f and g.

The maximum cross-correlation method was applied to f_n and g_n. This method can be computationally expensive, but it eliminates the need to bias the data to recover the lags. Also, it accurately estimates the degree of similarity between different sequences. I extended the one-dimensional maximum cross-correlation algorithm to two dimensions and applied the technique to elastic lidar data to measure horizontal winds as a function of range and altitude (three-dimensional winds) in the atmospheric boundary layer.

4-3 Two-Dimensional Maximum Cross-Correlation

The basis for two-dimensional maximum cross-correlation was established in the one-dimensional example (section 4-2). As in the one-dimensional example, begin with a kernel space and a search space. Now, however, the kernel is indexed through two-dimensions (time and distance, for example). Otherwise, the principle is the same. As before, each time the kernel is moved one time or distance bin through the search space, calculate the correlation between the kernel and the search space sub-image centered on the distance and time index. Then, store the amount of correlation at the index lag positions in a two-dimensional space-time lag matrix. The maximum value in the space-time lag matrix gives the temporal and spatial delay between the kernel and lag-image (the best search space sub-image match with the kernel).

4-3.1 Definitions

Consider a search space, σ, and a kernel space, K. Define the dimension of each space as

$$dim(\sigma) = dim(\mathrm{K}) = [M \quad N]. \tag{4.8}$$

From K we select *one* kernel, κ, and correlate κ with sub-images, σ_{pq}, from σ. Define the dimension of κ and the σ_{pq}s so that

$$dim(\kappa) = dim(\sigma_{pq}) = [m \quad n], \tag{4.9}$$

with $m \ll M$ and $n \ll N$. Define κ' so that

$$\kappa' \rightarrow \kappa - \langle\kappa\rangle, \tag{4.10}$$

where the average of κ, denoted $\langle\kappa\rangle$, is defined as

$$\langle\kappa\rangle = \sum_{i=1}^{m}\sum_{j=1}^{n} \kappa_{ij} / (m \cdot n). \tag{4.11}$$

With these definitions (Eqs. 4.9 to 4.12), we define the elements of the two-dimensional cross-correlation function, Γ_{pq}, which fill the lag-matrix, Γ, as

$$\Gamma_{pq} \equiv \frac{\sum_{i=1}^{m}\sum_{j=1}^{n} \kappa'_{ij}(\sigma_{i-1+p,j-1+q} - \langle\sigma_{pq}\rangle)}{\sqrt{\sum_{i=1}^{m}\sum_{j=1}^{n} \kappa'^{2}_{ij}}\sqrt{\sum_{i=1}^{m}\sum_{j=1}^{n} (\sigma_{i-1+p,j-1+q} - \langle\sigma_{pq}\rangle)^2}}, \tag{4.12}$$

where

$$\langle\sigma_{pq}\rangle = \frac{1}{m \cdot n}\sum_{i=1}^{m}\sum_{j=1}^{n} \sigma_{i-1+p,j-1+q}, \tag{4.13}$$

and

$$dim(\Gamma) = [p \;\; q] = [\,(M-m+1) \;\; (N-n+1)\,], \tag{4.14}$$

i.e., in Eqs. 4.12 and 4.13, $1 \le p \le (M - m + 1)$, and $1 \le q \le (N - n + 1)$. Note two important properties of the numerator in Eq. 4.12 which are useful for calculating the correlation between κ' and the σ_{pq}s: (1) the sum on the left in Eq. 4.15 is equivalent to the sum on the right

$$\sum_{i=1}^{m}\sum_{j=1}^{n} \kappa'_{ij}(\sigma_{i-1+p,j-1+q} - \langle\sigma_{pq}\rangle) = \sum_{i=1}^{m}\sum_{j=1}^{n} \kappa'_{ij}\sigma_{i-1+p,j-1+q}, \tag{4.15}$$

because

$$\sum_{i=1}^{m}\sum_{j=1}^{n} \kappa'_{ij} = 0; \tag{4.16}$$

and (2) Eqs. 4.12 and 4.15 can be calculated using the *correlation* theorem (Press et al. 1992). The correlation of functions g and h, denoted $Corr(g,h)$, is defined as the middle term in Eq. 4.17, and is equivalent to the term on the right in Eq. 4.17:

$$Corr(g,h) \equiv \int_{-\infty}^{\infty} g(t+\tau)h(\tau)d\tau \Leftrightarrow \Im^{-1}\,[\Im\,[g(t+\tau)] \times \Im^{*}\,[h(\tau)]\,]. \tag{4.17}$$

The correlation theorem states that the integral of the product of $g(t + \tau)$ and $h(t)$ is equivalent to the *inverse* Fourier transform, $\Im^{-1}[\ldots]$, of the product of the Fourier transform, $\Im[\ldots]$, of $g(t + \tau)$ and the *complex conjugate* of the Fourier transform, $\Im^{*}[\ldots]$, of $h(t)$, i.e., $Corr(g,h) \Leftrightarrow \Im^{-1}[\Im[g] \times \Im^{*}[h]]$. Thus, for computational purposes we can use the correlation theorem to calculate the lag matrix, Γ, between κ' and σ.

First, redefine κ' by its normalization:

$$\kappa' \rightarrow \kappa / \sqrt{\sum_{i=1}^{m} \sum_{j=1}^{n} \kappa_{ij}^{2}}, \tag{4.18}$$

where by previous definition $\langle \kappa \rangle = 0$. Next, center the normalized kernel in a zero padded matrix of the same dimension as the search space and calculate Γ, i.e.,

$$\Gamma = \Im^{-1} [\Im [\kappa'] \times \Im^{*} [\sigma]]. \tag{4.19}$$

Note that Γ is the unnormalized lag matrix of interest.

The lag matrix (Γ) must be normalized one pixel at a time. This requires a calculation of normalization coefficients for the elements of Γ. Calculate the normalization coefficients by *filtering* (convolving) the search space with a summing filter of the same dimension as κ'. The filter, ϑ, is a matrix of ones defined such that $dim(\vartheta) = dim(\kappa) = [m\, n]$. Calculate the pixel normalizations by first summing the σ_{pq}s over the weights of the filter, ϑ:

$$\Sigma_{pq} = (m \cdot n) \langle \sigma_{pq} \rangle \equiv \sum_{i=1}^{m} \sum_{j=1}^{n} \vartheta_{ij} \sigma_{i-1+p, j-1+q}, \tag{4.20}$$

where by application of the correlation theorem:

$$\Sigma_{pq} \Leftrightarrow \Im^{-1} [\Im [\vartheta] \times \Im^{*} [\sigma_{pq}]]. \tag{4.21}$$

Next, square the σ_{pq}s and sum the squares over the weights of the filter, ϑ:

$$\Sigma_{pq}^{2} = (m \cdot n)^{2} \langle \sigma_{pq}^{2} \rangle \equiv \sum_{i=1}^{m} \sum_{j=1}^{n} \vartheta_{ij} \sigma_{i-1+p, j-1+q}^{2}, \tag{4.22}$$

where by use of the correlation theorem:

$$\Sigma_{pq}^2 = \Im^{-1}\left[\Im\left[\vartheta\right] \cdot \Im^*\left[\sigma_{pq}^2\right]\right]. \tag{4.23}$$

With these definitions (Eqs. 4.20 to 4.23), define the pixel normalization, π_{pq}:

$$\pi_{pq} = \sqrt{\Sigma_{pq}^2 - (m \cdot n)\,(\Sigma_{pq})^2}. \tag{4.24}$$

Thus, the cross-correlation matrix, Γ, is appropriately normalized by dividing the elements of Γ by the elements of the normalization matrix π, i.e.,

$$\Gamma_{pq} \rightarrow \Gamma_{pq}/\pi_{pq}. \tag{4.25}$$

4-3.2 Two-Dimension Summary

Two-dimensional maximum cross-correlation is a template matching scheme. Given a template (*kernel*) from the kernel space, and another image (*search space*) which may contain a sub-image of the degraded kernel (image degradation in the lidar wind context results from advective and turbulent transport of the imaged aerosols), the maximum cross-correlation algorithm searches the search space for the best kernel and search space sub-image match. The search is accomplished by sliding (or indexing) the kernel throughout the search space and calculating correlation coefficients between the kernel and search space sub-images of the same dimension as the kernel. The coefficients are stored in a two-dimensional lag-matrix whose maximum value (maximum cross-correlation) gives the delays between the kernel and the search space sub-images.

In the context of the lidar data, the delays, or lags (range and time lags), are used to calculate a wind speed and direction. The application of the algorithm to lidar data produces a database containing information about winds as a function of range and altitude. The database is postprocessed to identify the most likely wind speeds and directions in the scanned volume of space.

As noted in an earlier chapter, a typical three-angle correlation data set contains information about the variation in backscattered intensity as a function of range and time at three similar observation angles (the observation angles are separated by a small angle). The maximum cross-correlation algorithm calculates correlations between aerosol features that persist between two or three of the angles. High correlations can determine winds so that $\vec{v}_{wind} \sim \vec{\Delta r}/\Delta t$, where $\vec{\Delta r}$ is a function of the range-lag and angular separation between the kernel and the lag-image (search space sub-image which best matches the kernel).

4-4 Sample Problem: A Lidar Application

Cross-correlation calculations usually compare the same scene at different times. Imagine taking a geosynchronous satellite photo of a region of the earth at 1000 hours and another photo of the same region of earth, from the same geosynchronous satellite, at 1100 hours. If clouds are present and pixel intensities between the two images are correlated, then the result of the pixel correlations is a range-lag between the images. Calculate the direction and distance the clouds have traveled by determining the distance vector between the original pixels, position and the lagged pixels,

position. The mean wind is the distance traveled divided by the difference in time (60 minutes in this example).

Stationary features in the correlated images can add a type of noise to the resulting lags. What happens mathematically is that the stationary features in the images skew the deviation about the mean square between the two data sets toward zero lag. The fine scale detail (which may have moved) cannot be resolved above the zero lags of the stationary parts between the two images. This effect can be minimized by application of the maximum cross-correlation method.

Maximum cross-correlation reduces the stationary feature effect by separating one of the larger images into small kernels and correlating the kernels with sub-images from the remaining larger image. This method can be computationally expensive but can produce accurate lags (or delays) while reducing the effects of bulk-image features. Further, the size of the kernels can be varied to determine how winds depend on feature sizes. This technique has been used to measure sea-surface velocities (Emery et al. 1986), ice pack motions (Ninnis et al. 1986), and cloud motions (Leese et al. 1970).

The application of the maximum cross-correlation technique to elastic lidar data differs from the basic application in that the lidar surveys different scenes (different observation angles) during the same time period. The basic application usually correlates the same scene at later times.

Imagine trying to determine how fast a car is travelling past a picket fence by building two-dimensional images from a time-series of snapshots taken alternately through different slits in the picket-fence—this is analogous to the lidar problem. In the lidar problem, correlations are performed in the temporal and spatial domains to yield a range- and time-lag between adjacent observation angles. The lags and the spatial separation between the positions of maximum cross-correlation between the two observation angles are used to calculate a wind vector between the kernel and the lag-image.

4-4.1 Three-Angle Correlation Scans

The Los Alamos lidar wind sensing technique estimates three-dimensional wind fields through the use of three-angle correlation scans. The three-angle scanning pattern (Fig. 4.5) was done by the University of Wisconsin lidar team as early as 1979 (Sroga et al. 1980) and as recently as 1985 (Hooper et al. 1986) to measure winds. Eloranta's lidar team (Edwin Eloranta is the chief scientist directing Wisconsin's lidar program) continued to use this scanning technique until the late 1980s when they began using three-dimensional scanning algorithms to remotely measure three-dimensional wind fields.

The maximum cross-correlation method provides best results with lidar data acquired at low elevation angles (θ) when the winds are transverse to the lidar's field of view. Three-angle (ϕ) correlation scans, as opposed to two-angle correlation scans, were used at LANL for two reasons: (1) the three angles allow more independent cor-

relations per data file, i.e., correlations can be calculated between observation angles 1 and 2, observation angles 1 and 3, and observation angles 2 and 3, and thus provide a large database of correlation results to postprocess and examine for trends to allow development of selection rules for determining the most likely direction of transport; (2) because data acquisition was restricted to about 65 s per file (to permit the hourly survey of a large volume of space), the three-angle scans provided a way to measure

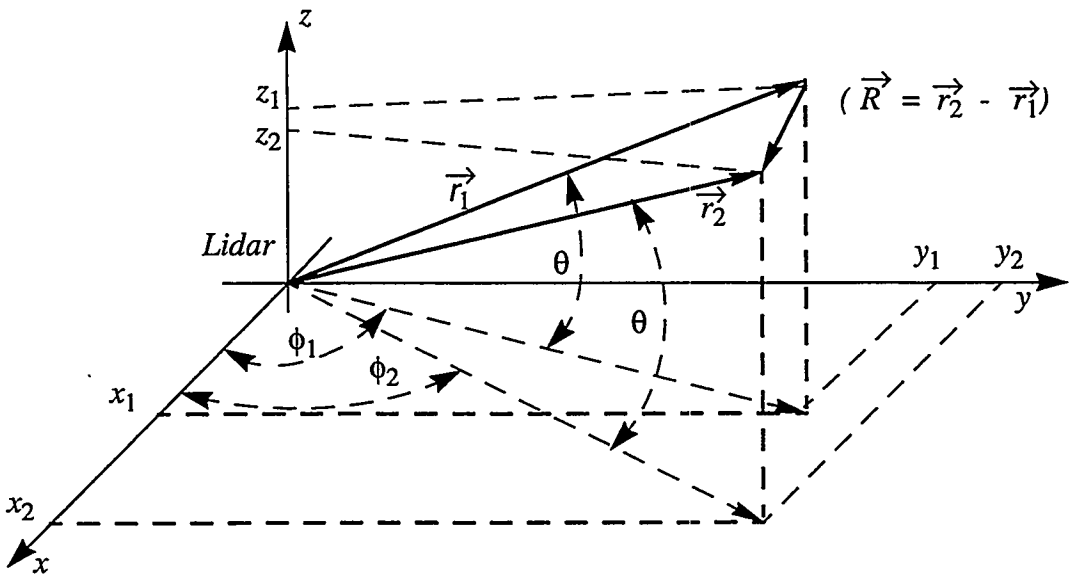

Fig. 4.5: Two-Angle Correlation Scan Pattern

The above diagram illustrates the observation angles for a two-angle correlation scanning pattern. Observation angle one is ϕ_1, and observation angle two is ϕ_2. A three-angle scanning pattern would include one more observation angle, ϕ_3. The elevation angle at which the data are acquired is θ.

Multiple-angle data are acquired by pointing the lidar in each direction for ~0.2 s to accumulate a record. The lidar cycle time through all three angles is about 1.8 s, and the time required to obtain 35 records for each angle is 62 s. Each correlation scan contains a total of 105 records.

This figure illustrates some of the important quantities used to estimate wind speed, direction, and their uncertainties. The lidar directions are $\vec{r_1}$ and $\vec{r_2}$. The laser is at the origin and the elevation angle θ stays unchanged while ϕ varies in steps of 0.45°.

winds at far and near ranges in the allotted data acquisition time period. For example, the three azimuth angles in the correlation scans are usually separated by a small angle (0.50° or less). This small separation angle means an imaged aerosol inhomogeneity must traverse a minimum distance of 50 m to be observed in two adjacent lidar observation angles at a range of 6 km. Thus, an aerosol inhomogeneity traveling at 2 m/s at a distance of 6 km from the lidar requires a minimum of 25 s to traverse the distance between adjacent observation angles. The transport time will be longer than 25 s if the direction of transport is not transverse (at a right angle) to the observation angle. Low-speed winds might only be resolved between two adjacent observation angles at far ranges, and winds may only be resolved between the first and third observation angles at near ranges. In addition, when wind speeds are high, the time of transport between adjacent observation angles can be so fast that large uncertainties in the wind calculation result. In this circumstance, correlations between line of sight 1 and line of site 3 can produce more accurate results—especially at near ranges.

4-4.1.1 Example Calculation

Fig. 4.6 shows a kernel space, K, and Fig. 4.7 shows the search space, σ (these images correspond to angles 1 and 3 of the three-angle correlation scan seen in Fig. 3.4, Ch. 3). The two observation angles are azimuthally separated by 0.9° and were acquired at an elevation angle of 1.5°. A kernel, κ, is arbitrarily chosen from the kernel space, K, and cross-correlated with the search space, σ. The cross-correlation procedure produces a lag-matrix, Γ, whose maximum value gives a range- and time-

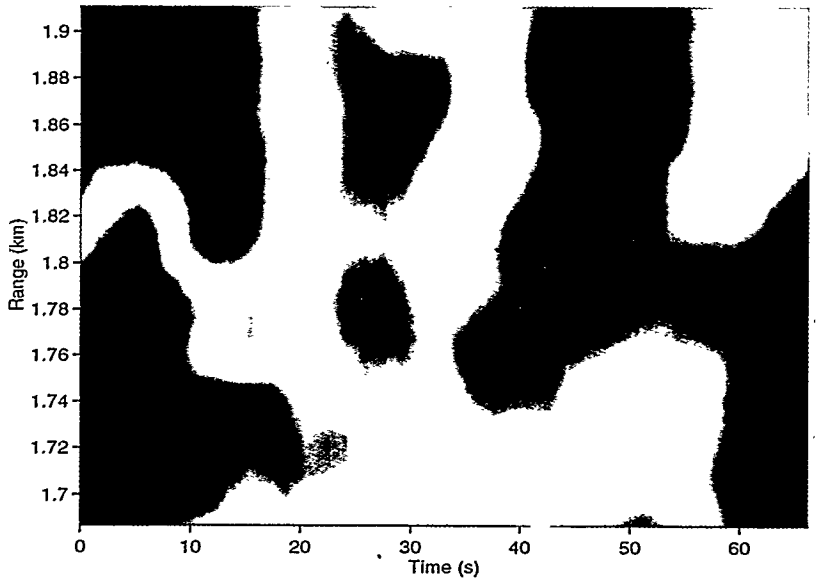

Fig. 4.6: Kernel Space, K

Kernels from the above kernel space, K, are arbitrarily selected and cross-correlated with the search space (Fig. 4.7).

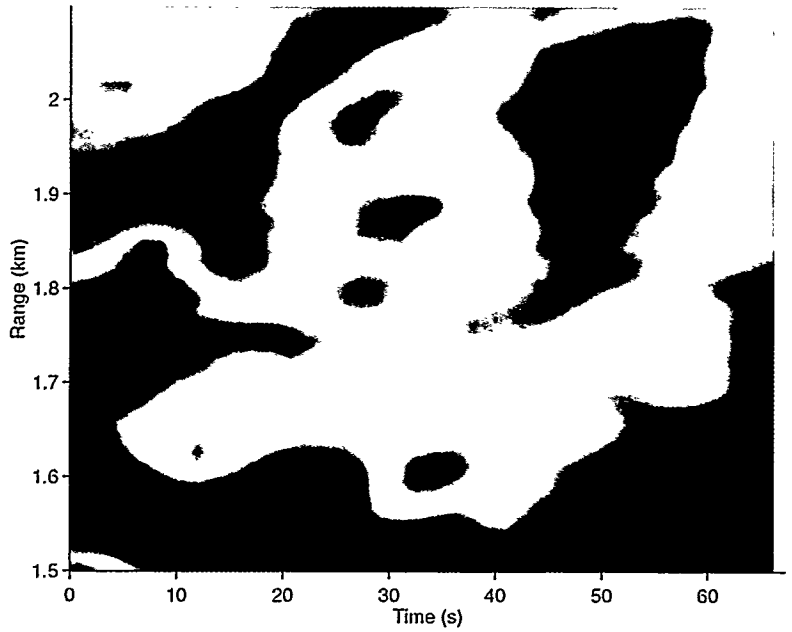

Fig. 4.7: Search Space, σ

This search space is centered at the same range as the kernel space, K.

lag (delay) between κ and search space sub-images, σ_{pq}s. Fig. 4.8 shows the lag matrix, Γ, calculated from cross-correlating κ (Fig. 4.9A) with σ (Fig. 4.7). The range-and-time lags corresponding to the maximum cross-correlation in Γ are used together with the angular separation between K and σ (0.9°) and the ranges of κ and the search space lag-image, λ, from the lidar to calculate the wind between κ and the σ_{pq}s. Fig. 4.9 shows, κ, and the lag-image, λ, which gave the maximum cross-correlation between κ and the σ_{pq}s. The best search space sub-image match with κ is λ, and it is centered at t = 23.4 s at a distance of 1.814 km; κ is centered at t = 20.6 s and a distance of 1.799 km. The time delay between κ and λ is 2.8 s. This azimuthal separation

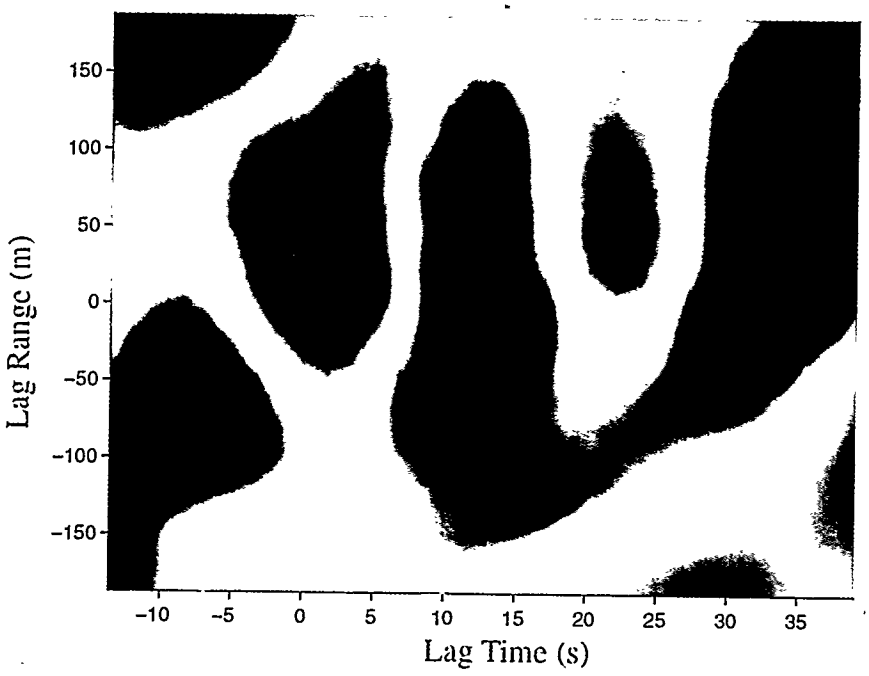

Fig. 4.8: Lag-Matrix, Γ

The lag-matrix, Γ, between κ and σ. Red colors correspond to high correlations and blue colors correspond to low correlations.

between κ and λ (0.9°), their elevation angle (1.5°), and their ranges from the lidar (1.814 km and 1.799 km) give a wind speed of 13.8 m/s. The orientation of the lidar with respect to north gives the wind direction as 131 degrees from north. The altitude of the measurement is ~90 m above the ground at ~1.8 km. The correlation between κ

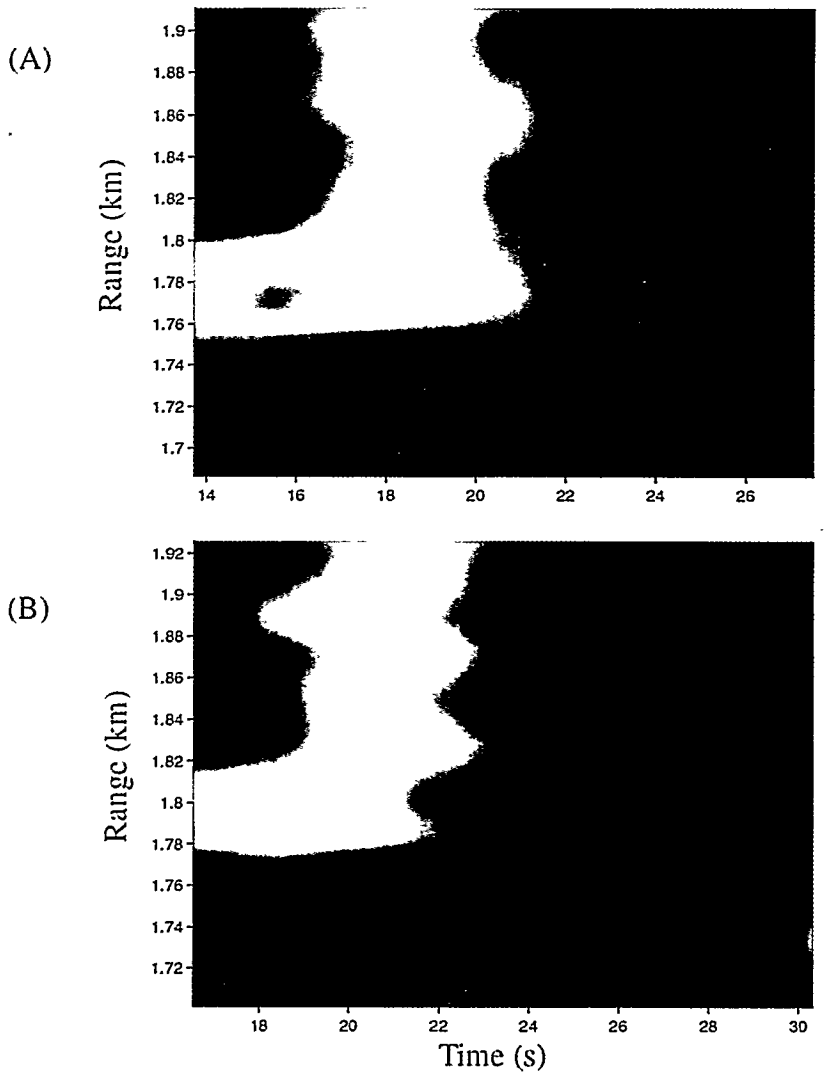

Fig. 4.9: Kernel, κ, and Lag-Image, λ

κ is the top image (A) and λ is the bottom image (B). κ was selected from the kernel space, K (Fig. 4.6), while λ is the best kernel and search space sub-image match from the search space, σ (Fig. 4.7).

and λ was 97.7%. The similarity between κ and λ supports the high correlation value. The Physical Science Laboratory (PSL) laser doppler velocimeter[1] (LDV) (positioned ~1.8 km from the lidar at the azimuth angle the lidar data were acquired) measured winds of ~11 m/s at ~125 degrees from north. The lidar measurement has an uncertainty of ±5 degrees and ±3 m/s. The mathematical forms of uncertainties in the lidar calculation are discussed in the next section. Uncertainties in the LDV winds are not known by the author, but they are thought to be less than 10%. LDV wind measurements are instantaneous point measurements across the diameter of a circle acquired every 5 s. This lidar measurement is an average over a distance of ~39 m and took 2.5 s to acquire.

The computer program used to calculate the lag matrix, Γ, between κ and σ is in Appendix B. The program's algorithm is based on the correlation theorem, is written in the matlab computer language, and takes ~0.43 s to calculate the correlation matrix between a normalized kernel, κ (κ is defined such that $\langle\kappa\rangle=0$ and $dim(\kappa) = [31\ 9]$), and a unnormalized search space, σ ($dim(\sigma) = [81\ 40]$), on a Hewlett Packard HP 715/64. Thus it is clear this method can be computationally expensive when applied to large data sets (such as those produced with lidar). Because of this, kernel spaces are arbitrarily selected for the wind calculation (kernel spaces are chosen at every fifth range bin [every 30 m] for correlation with search spaces). This gave

1. PSL has indicated that laser doppler velocimeter technology was developed by the Environmental Protection Agency (personal communication). For more information, contact Jose M. Serna, (505) 522-9100 Ext. 333, Physical Science Laboratory, Box 30002, Las Cruces, New Mexico 88003-0002.

~300 kernel/search space correlations per data file when only one kernel from each kernel space is correlated with its neighboring search space.

The computer program used to calculate the explicit sums (defined by Eqs. 4.11 to 4.13) is in Appendix C. The program takes approximately 2.02 s per correlation to execute. Thus, using the correlation theorem calculates the correlations in about 1/5 the amount of time needed to calculate the explicit sums. (Note that this may not be true for computer code written in a compiled language such as *FORTRAN* or *C*.)

4-5 Wind Uncertainties

Linear error analysis is used to estimate uncertainties in the wind speed and direction. Because data are acquired as a function of range and time, uncertainties appear in the range and time variables. Range uncertainties are an artifact of the digital nature of the sampled data (data are sampled [digitized] at a rate of $\nu = 20$ mega-samples per second). The rate of digitization samples the backscattered light every 7.5 m, i.e., $\Delta r = c/(2\nu) \Leftrightarrow \Delta r = 7.5$ m, where c is the speed of light in air ($c \sim 3.00\times10^8$ m/s), and the factor of 2 results from the emitted laser light traveling to and from the scattering region of the atmosphere.

Assume the range- and time-centers of the kernel are well known. Then uncertainties are associated with the range- and time-center of the lag-image. If the range- and time-center of the kernel is $\vec{r_1}$ and t_1, then the range- and time-center of

the lag-image is $\vec{r_2} \pm \Delta r/2 = \vec{r_2} \pm 3.75$ m and $t_2 \pm \Delta t_2$. Calculate the wind direction, Θ, as the angle whose tangent is determined by the difference in the x and y coordinates of the kernel and lag-image multiplied by the sign of the time difference between the kernel and lag-image:

$$\Theta = \text{atan}\frac{\text{sgn}\,(t_2 - t_1) \cdot (y_2 - y_1)}{(x_2 - x_1)}. \tag{4.26}$$

(The sign of the time difference determines whether the imaged aerosols are traveling left to right or right to left across the lidar observation angles.)

Wind direction and speed uncertainties are calculated with the first derivative. Consider two vectors, $\vec{r_1}$ and $\vec{r_2}$, as shown in Fig. 4.5. (The direction of transport is defined by Eq. 4.26.) Now define

$$y = \text{sgn}\,(t_2 - t_1) \cdot (y_2 - y_1), \tag{4.27}$$

and

$$x = x_2 - x_1, \tag{4.28}$$

so that

$$\Theta \rightarrow \text{atan}\frac{y}{x}. \tag{4.29}$$

Thus, Θ is defined as the projection onto the *xy-plane* of the difference between the position centers of the kernel and lag-image multiplied by the sign of the time difference. (The sign of $t_2 - t_1$ can be ignored since only relative uncertainties are important.)

Fig. 4.5 shows that

$$\vec{R} = \vec{r}_2 - \vec{r}_1 = (x_2 - x_1)\hat{i} + (y_2 - y_1)\hat{j} + (z_2 - z_1)\hat{k}. \tag{4.30}$$

Therefore,

$$R \equiv |\vec{R}| = |\vec{r}_2 - \vec{r}_1| \Leftrightarrow \sqrt{r_2^2 + r_1^2 - 2r_1 r_2 \cos(\phi_2 - \phi_1)}. \tag{4.31}$$

The vertical component of the wind is small and difficult to measure with elastic backscatter lidar techniques. Based on this, the vertical component of the wind vector is ignored, and the wind speed is redefined as

$$v \equiv |\vec{v}| = R\cos\theta / |t_2 - t_1|, \tag{4.32}$$

where θ is the elevation angle at which the data are acquired, and R is defined in Eq. 4.31. Rewrite Eq. 4.29 so that

$$\Theta = \operatorname{atan} u, \tag{4.33}$$

where

$$u = y/x = (y_2 - y_1)/(x_2 - x_1). \tag{4.34}$$

This implies

$$y = \cos\theta\,(r_2 \sin\phi_2 - r_1 \sin\phi_1), \tag{4.35}$$

and

$$x = \cos\theta\,(r_2 \cos\phi_2 - r_1 \cos\phi_1), \tag{4.36}$$

where ϕ_1 and ϕ_2 are the azimuthal angles measured with respect to $\vec{r_1}$ and $\vec{r_2}$.

Recall that there is no uncertainty associated with the kernel variables $\vec{r_1}$ and t_1, and assume that the elevation angle, θ, associated with the kernel and the lag-images is constant. (Thus, there is no uncertainty associated with θ because it does not vary.) Then, uncertainty of $\vec{r_2}$ is fixed ($\Delta r_2 = 3.75$ m), the uncertainty of t_2 varies with the individual lidar record time stamps, and the uncertainties of ϕ_1 and ϕ_2 are assumed constant and equal to the resolution of the digital encoders (22×10^{-3} degrees). Calculate the uncertainty of the wind speed and direction with Eqs. 4.32 to 4.36 and the uncertain quantities associated with the kernel and lag-image as the sum of the magnitudes of the first derivative of the wind speed or direction with respect to their uncertain quantities times the uncertainty of the quantity. This statement is expressed as

$$\Delta Q = \sum_{i=1}^{n} \left|\frac{\partial Q}{\partial q_i}\right| \Delta q_i, \tag{4.37}$$

where Q is an uncertain measurement, and the q_i are the uncertainties of Qs variables.

Applying Eq. 4.37 to Eq. 4.32 gives the uncertainty in the magnitude of the wind, Δv, as

$$\Delta v = \frac{\partial v}{\partial R}\left|\frac{\partial R}{\partial r_2}\right| \Delta r_2 + \left|\frac{\partial v}{\partial t_2}\right| \Delta t_2, \tag{4.38}$$

where

$$\frac{\partial v}{\partial R} = \frac{\cos\theta}{|t_2 - t_1|} > 0, \tag{4.39}$$

$$\frac{\partial R}{\partial r_2} = \frac{r_2 - r_1\cos(\phi_2 - \phi_1)}{R} \Leftrightarrow \frac{\hat{r}_2 \cdot (\vec{r}_2 - \vec{r}_1)}{R}, \tag{4.40}$$

and

$$\frac{\partial v}{\partial t_2} = \frac{-R\cos\theta}{(t_2 - t_1)^2}. \tag{4.41}$$

Putting Eq. 4.38 together with Eqs. 4.39 to 4.41 gives

$$\Delta v \equiv \frac{R\cos\theta}{|t_2 - t_1|}\left(\frac{|\hat{r}_2 \cdot (\vec{r}_2 - \vec{r}_1)|\Delta r_2}{R^2} + \frac{\Delta t_2}{|t_2 - t_1|}\right) \Leftrightarrow v\left(\frac{|\hat{r}_2 \cdot \vec{R}|\Delta r_2}{R^2} + \frac{\Delta t_2}{|t_2 - t_1|}\right). \tag{4.42}$$

Applying Eq. 4.37 to Eqs. 4.33 to 4.36, with the definitions of the uncertain quantities, gives the uncertainty of the wind direction as

$$\Delta\Theta = \left|\frac{\partial\Theta}{\partial u}\right|\left[\left|\frac{\partial u}{\partial r_2}\right|\Delta r_2 + \left(\left|\frac{\partial u}{\partial \phi_1}\right| + \left|\frac{\partial u}{\partial \phi_2}\right|\right)\Delta\phi_1\right], \tag{4.43}$$

where

$$\frac{\partial\Theta}{\partial u} = \frac{1}{1 + u^2} \Leftrightarrow \frac{x^2}{x^2 + y^2}, \tag{4.44}$$

and

$$\begin{aligned}\frac{\partial u}{\partial r_2} &= \frac{\partial u}{\partial x}\cdot\frac{\partial x}{\partial r_2} + \frac{\partial u}{\partial y}\cdot\frac{\partial y}{\partial r_2} = \frac{-y}{x^2}\cos\theta\cos\phi_2 + \frac{x}{x^2}\cos\theta\sin\phi_2 \\ &= \frac{\cos^2\theta}{x^2} r_1 \sin(\phi_2 - \phi_1) \Leftrightarrow \frac{\cos^2\theta}{x^2}\vec{r}_1 \times \hat{r}_2.\end{aligned} \tag{4.45}$$

Putting Eq. 4.43 together with Eqs. 4.44 and 4.45 gives the uncertainty of Θ with respect to r_2 as

$$\frac{\Delta\Theta}{\Delta r_2} \to \left|\frac{\partial\Theta}{\partial u}\right|\left|\frac{\partial u}{\partial r_2}\right| \Leftrightarrow \frac{\cos^2\theta}{x^2+y^2}\left|\vec{r_1}\times\hat{r_2}\right|. \tag{4.46}$$

The uncertainty of Θ with respect to ϕ_1 is

$$\frac{\Delta\Theta}{\Delta\phi_1} \to \left|\frac{\partial\Theta}{\partial\phi_1}\right| = \left|\frac{\partial\Theta}{\partial u}\cdot\frac{\partial u}{\partial x}\cdot\frac{\partial x}{\partial\phi_1}\right| \tag{4.47}$$

where

$$\begin{aligned}\frac{\partial u}{\partial x}\cdot\frac{\partial x}{\partial\phi_1} &= -\frac{\cos\theta}{x^2}\left(y\cdot r_1\sin\phi_1 + x\cdot r_1\cos\phi_1\right),\\ &= \frac{\cos^2\theta}{x^2}\left(r_1^2 - r_1 r_2\cos\left(\phi_2-\phi_1\right)\right) \Leftrightarrow \frac{\cos^2\theta}{x^2}\left[\vec{r_1}\cdot\left(\vec{r_1}-\vec{r_2}\right)\right].\end{aligned} \tag{4.48}$$

Thus,

$$\frac{\Delta\Theta}{\Delta\phi_1} \to \left|\frac{\partial\Theta}{\partial\phi_1}\right| = \frac{\cos^2\theta}{x^2+y^2}\left|\vec{r_1}\cdot\left(\vec{r_1}-\vec{r_2}\right)\right|. \tag{4.49}$$

Symmetry considerations imply that the uncertainty of Θ with respect to ϕ_2 is

$$\frac{\Delta\Theta}{\Delta\phi_2} \to \left|\frac{\partial\Theta}{\partial\phi_2}\right| = \frac{\cos^2\theta}{x^2+y^2}\left|\vec{r_2}\cdot\left(\vec{r_2}-\vec{r_1}\right)\right| \Leftrightarrow \frac{\cos^2\theta}{x^2+y^2}\left|\vec{r_2}\cdot\left(\vec{r_2}-\vec{r_1}\right)\right|. \tag{4.50}$$

Eqs. 4.46, 4.49, and 4.50 imply that the total uncertainty in direction is

$$\Delta\Theta = \frac{\cos^2\theta}{x^2+y^2}\left[\left|\vec{r_1}\times\hat{r_2}\right|\Delta r_2 + \left(\left|\vec{r_1}\cdot\left(\vec{r_1}-\vec{r_2}\right)\right| + \left|\vec{r_2}\cdot\left(\vec{r_2}-\vec{r_1}\right)\right|\right)\Delta\phi_1\right]. \tag{4.51}$$

Thus, an upper bound on the uncertainty in wind speed is

$$\Delta v \equiv \frac{R\cos\theta}{\left|t_2-t_1\right|}\left(\frac{\left|\hat{r}_2\cdot\hat{R}\right|\Delta r_2}{R} + \frac{\Delta t_2}{\left|t_2-t_1\right|}\right), \tag{4.52}$$

and an upper bound on the uncertainty in the wind direction is

$$\Delta\Theta = \frac{\cos^2\theta}{x^2+y^2}\left|\vec{r}_1 \times \hat{r}_2\right|\Delta r_2 + \frac{\cos^2\theta}{x^2+y^2}\left(\left|\vec{r}_1 \cdot \hat{R}\right| + \left|\vec{r}_2 \cdot \hat{R}\right|\right)\Delta\phi_1. \tag{4.53}$$

4-5.1 Summary

Spatial uncertainties in the lag-image are caused the digitizer sampling rate and the rastering of the system through the three angles of the correlation scans. The consecutive nature of three-angle data acquisition also causes temporal uncertainties. The temporal and spatial uncertainties gives the uncertainties in the wind.

Finally, the looseness or flexibility in the gimbal (rastering mechanism) system could introduce a systematic error in wind direction. If a systematic error exists, the calibration runs performed at the beginning and end of each day for which data were acquired will reveal the magnitude of this uncertainty. It is expected that this directional uncertainty will introduce a simple additive constant to the wind direction.

References

Bendat, J. S., and A. G. Piersol, "Random Data: Analysis and Measurement Procedures," John Wiley and Sons (1971).

Emery, W. J., A. C. Thomas, and M. J. Collins, "An Objective Method for Computing Advective Surface Velocities from Sequential Infrared Images," *Journal of Geophysical Research,* Vol. 91, No. C11 (1986).

Hooper, W. P., and E. W. Eloranta, "Lidar Measurements of Wind in the Planetary Boundary Layer: The Method, Accuracy and Results from Joint Measurements with Radiosonde and Kytoon," *Journal of Climate and Applied Meteorology.* Vol. 25, No. 7 (1986).

Leese, J. A., and C. S. Novak, "An Automated Technique for Obtaining Cloud Motion from Geosynchronous Satellite Data Using Cross Correlation," *Journal of Applied Meteorology*, Vol. 10 (1971)

Ninnis, R. M., W. J. Emery, and J. M. Collins, "Automated Extraction of Pack Ice Motion from Advanced Very High Resolution Radiometer Imagery," *Journal of Geophysical Research.* Vol. 91, No. C9 (1986).

Press, W. H., S. A. Teukolsky, W. T. Vetterling, and B. P. Flannery, "Numerical Recipes in FORTRAN: The Art of Scientific Computing (Second Edition)," by Cambridge University Press (1992).

Sroga, J. T., and E. W. Eloranta, "Lidar Measurement of Wind Velocity Profiles in the Boundary Layer," *Journal of Applied Meteorology,* Vol. 19, No. 5 (1980).

Suggested Reading

Schols, J. L., and E. W. Eloranta, "Calculation of Area-Averaged Vertical Profiles of the Horizontal Wind Velocity From Volume-Imaging Lidar Data," *Journal of Geophysical Research,* Vol. 97, No. D17 (1992).

Garcia, C. A. E., and I. S. Robinson, "Sea Surface Velocities in Shallow Seas Extracted From Sequential Coastal Zone Color Scanner Satellite Data," *Journal of Geophysical Research,* Vol. 94, No. C9 (1989).

5

Border Area Air-Quality Study

The Mexico/New Mexico/Texas border region has been designated non-attainment by the National Atmospheric Air-Quality Standards (NAAQS) for three atmospheric pollutants: ozone (O_3), carbon monoxide (CO), and respirable particulate matter (PM). Sunland Park, New Mexico, has experienced O_3 violations of the NAAQS during late summer months (such as September) usually between 1000 and 1400 hours. Ozone is not emitted directly into the boundary layer but is produced in secondary photo-chemical processes involving Volatile Organic Compounds (VOCs) and Nitrogen Oxygen compounds (NO_x).

The New Mexico Environment Department (NMED) believes that the Sunland Park non-attainment problems are caused by the transport of O_3 (and possibly VOCs, and NO_x) into the region from El Paso, Texas, and Ciudad Juarez, Mexico. EPA regulations may permit the state of New Mexico to avoid implementation of

some EPA regulatory measures if New Mexico can show that air pollution in Sunland Park is mainly migrating from outside of the area. Economic development in the region may then be allowed to continue. It was for this purpose that NMED funded the Border Area Air-Quality Study.

The Border Area Air-Quality study was conducted between September 8 and 11, 1994, in a collaboration between the NMED, the Physical Sciences Laboratory (PSL), the Texas Natural resources Conservation Commission (TNRCC), and Los Alamos National Laboratory (LANL). The main objective of the study was to map three-dimensional winds on both sides of Paso del Norte (the north pass) in the Mexico/New Mexico/Texas border area. (Fig. 5.1 shows a digital elevation map of the extended pass region. The north pass lies between the Franklin Mountains and the Sierra de Cristo Rey; El Paso, Texas, borders the Franklin Mountains east of the pass; Ciudad Juarez, Mexico, is south and east of the Sierra de Cristo Rey; Sunland Park, New Mexico, is west of the pass. Digital information for the map were provided by the United States Geologic Survey.)

Hourly three-dimensional wind fields measured on the west side of the north pass are plotted between 0800 and 1600 hours for September 10 and 11, 1994, in this chapter. PSL provided calibration wind data for experimental integrity. Calibration data were acquired 2 hours each day of the study with an EPA-approved remote-wind sensor. The calibration data were acquired from 0800 to 0900 hours and from 1300 to 1500 hours. Boundary layer depths, as observed by the lidar, are also plotted. The

boundary layer depths place a lower bound on the altitude at which the lidar can sense winds and the wind fields show the directions of mass flow, or aerosol transport, in the border area.

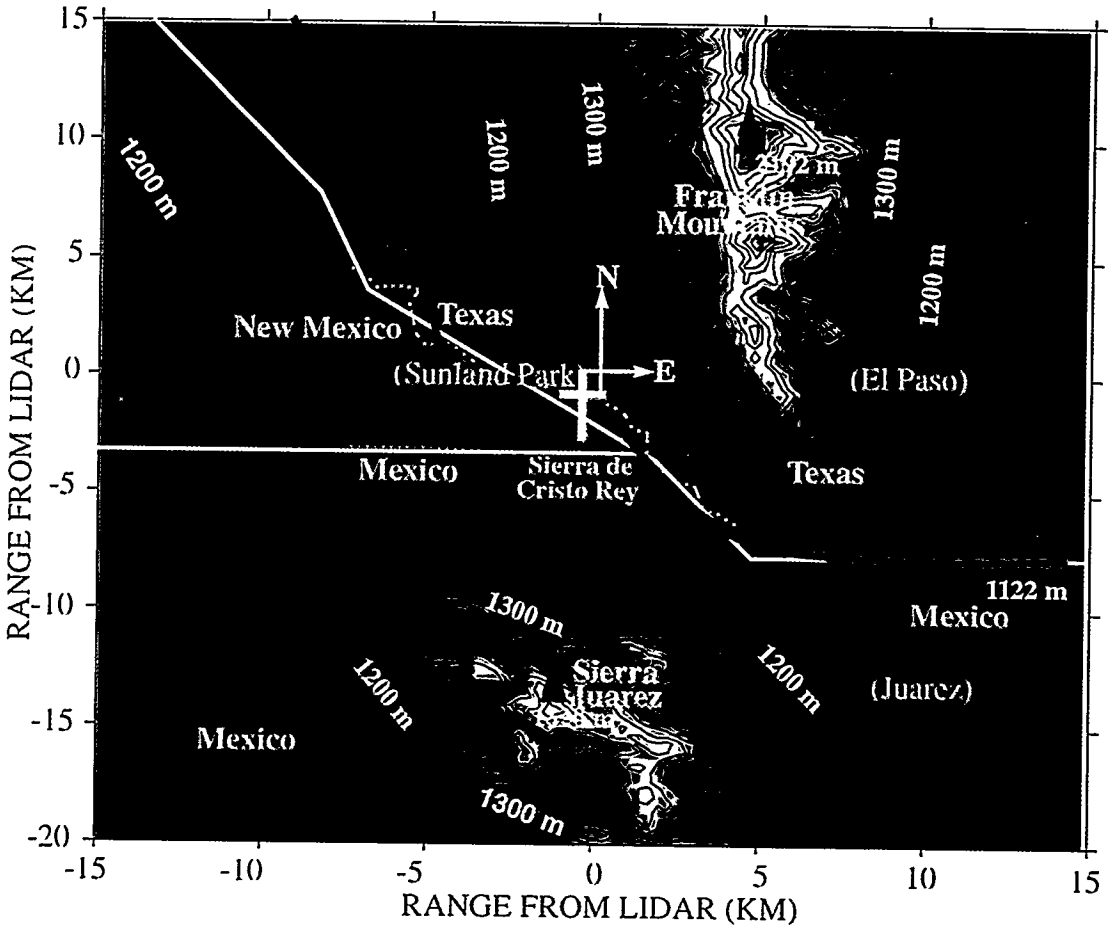

Fig. 5.1: Digital Elevation Map of the Extended Pass Region

The extended pass includes the plain between the Sierra de Cristo Rey and the Sierra Juarez as well as the north pass which lies between the Sierra de Cristo Rey and the Franklin Mountains.

The lidar system was positioned at the intersection of the north and east axes and was scanning the airspace south and west of its position.

Solid black lines are 100 m contours. The north pass follows the Rio Grande between Sierra de Cristo Rey and the Franklin Mountains. The extended pass includes the plane between Sierra de Cristo Rey and the Sierra Juarez.

Aerosol transport in the boundary layer was imaged with horizontal scans and boundary-layer depths were estimated with vertical scans. The hourly wind fields were extracted from three-angle correlation scans with the maximum cross-correlation algorithm. The lidar wind fields do not represent hourly averages, but it is hoped that the wind fields are representative of wind conditions each hour under steady-state assumptions. The time and spatial averages represented by the lidar wind fields are discussed in more detail later in this chapter.

5-1 Boundary Layer Depths

The boundary layer was observed near 500 m thickness around 0900 hours each morning, and grew to more than 2,000 m on September 10, 1994, and to more than 1,500 m on September 11, 1994. Although the air above the boundary layer was clear on September 10, on September 11 aerosols were observed from 200 m up to 4,000 m. The high-altitude aerosols observed on September 11 could be residual layers or emissions injected directly into the atmosphere above the boundary layer by a nearby industrial source such as the smelter 4 km away. The smelter operates 24 hours per day, has a 180 m high smokestack, and may have been exhausting during the night when the boundary-layer depth could drop below 200 m above the ground.

The lidar system used at Sunland Park provides best wind results in the boundary layer where aerosols are emitted directly into the atmosphere and provide a high density of aerosols to scatter light from. When residual layers are present, however, winds may be measured within the residual layers. The lidar may not sense high-

altitude winds above the boundary layer if higher altitude residual layers are not present. Fig. 5.2 shows boundary-layer depths for September 10 and 11, 1994. These depths were estimated from the vertical scans in Appendix D, and provide a lower bound for the altitude above the ground where the lidar can remotely measure winds.

5-2 Lidar Winds

Lidar winds were extracted from the lidar wind data base generated by the maximum cross-correlation method. Feature distortion of the imaged aerosols occurring during the transport process are the main source of noise in the lidar wind data base. The patterns or features defined by imaging the nonuniformities of particle sizes, shapes, number density, and chemical species from a parcel of air change due to turbu-

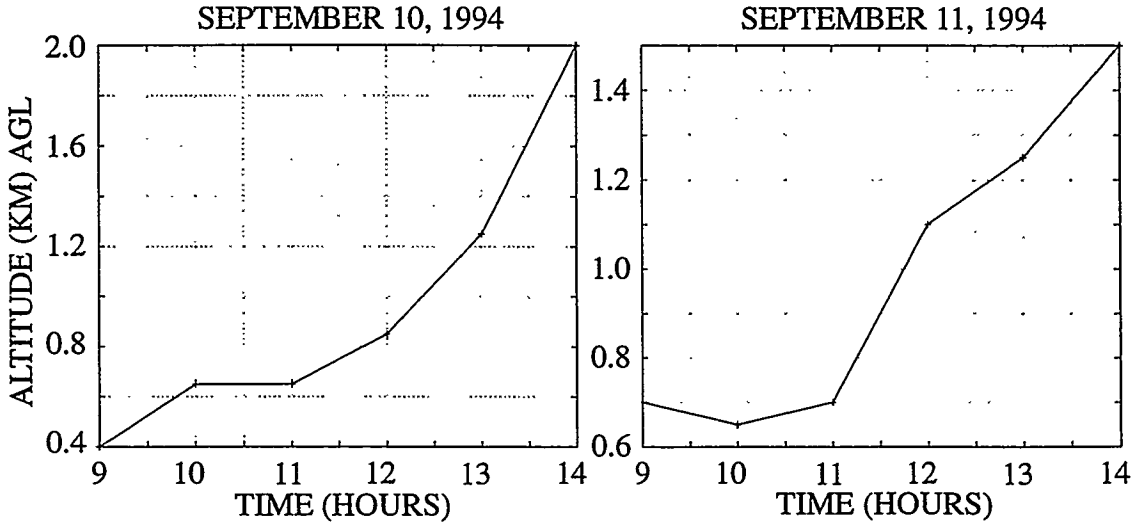

Fig. 5.2: Estimated Mean Boundary Layer Depths

The left plot is estimated boundary layer depths for September 10, 1994. Right plot is estimated boundary layer depths for September 11, 1994. Altitudes are relative to the lidar's ground level (AGL). The lidar was positioned at about 1,170 m MSL.

lent and advective processes in the atmosphere. These changes result in image degradation between the kernel and search space sub-image matches, which can lead to false correlations or noise in the results. The noise appears in the form of spurious wind speeds and directions.

To minimize feature degradation and reduce the effects of spurious winds on the data set, kernel sizes of ~200 m in the range dimension and ~13 s in the time dimension were chosen. The resultant kernel dimension of 31 range bins by 9 time bins for the Sunland Park data, is discussed in Ch. 4. This large spatial extent was chosen because large-scale features persist longer than small-scale features, as shown by scale analysis of the Kolmogorov turbulent energy spectrum (Landau 1989). These turbulent features are transported with the mean wind measured by the lidar.

Only data with correlations greater than 85% were used in the wind fields plotted. To further minimize noise effects, a vector median filter (Simpson et al. 1994) was applied to the data with correlations greater than 85%. The magnitude of the correlated wind vectors was ignored in the vector median filtering process. In effect, this application of the vector median filter (to unit vectors) selects the median direction from the set of wind vectors under consideration for plotting. Once the median direction is determined, all wind vectors within ±5° of the median direction were vector averaged and plotted. The scalar median is a special case of a vector median where all of the vectors lie on the real line.

The vector median is defined as the minimum sum of the magnitudes of the differences between a set of vectors. This statement is expressed in Eq's 5.1 to 5.3:

$$S_i = \sum_{j=1}^{N} \left| \vec{v}_i - \vec{v}_j \right|, \quad i = 1, 2, \ldots, N. \tag{5.1}$$

We now define S as the set of S_i such that

$$S \equiv \{S_1, S_2, \ldots, S_N\}. \tag{5.2}$$

The vector median, $\vec{v}_{vm}$, from the set of vectors $V = \{\vec{v}_1, \vec{v}_2, \ldots, \vec{v}_N\}$ is defined as the vector associated with the infimum of S. The infimum of S is the greatest lower bound of S, denoted ${}_{inf}S$, and the ${}_{inf}S$ is a member of the set S, i.e.,

$${}_{inf}S \in \{S_1, S_2, \ldots, S_N\}. \tag{5.3}$$

The median direction is similarly defined except that the median direction is given by the angle corresponding to the unit vector associated with the minimum sum of the magnitudes of the differences in the unit vectors, i.e., the set S is now given by

$$S = \{S_i\} = \left\{ \sum_{j=1}^{N} \left| \hat{v}_i - \hat{v}_j \right| \right\}, \quad i = 1, 2, \ldots, N. \tag{5.4}$$

And the median direction is given by $\hat{v}_k$, where k is, again, the value of j for which S_j is the minimum

$$\text{atan}\left(\hat{v}_k\right). \tag{5.5}$$

Three or more vectors are needed to apply a vector median filter.

5-2.1 Lidar and Laser Doppler Velocimeter Wind Comparisons

The Physical Sciences Laboratory LDV measures the doppler shift in back-scattered laser light to estimate winds. Since the doppler shift only gives the component of the wind toward or away from the laser system, the LDV system rotates through two pi radians (360°) and measures the doppler shift as a function of direction. To acquire the doppler data as a function of altitude, the laser is positioned at a 45° elevation angle. Thus, the doppler data are acquired on a conical surface and plots of the doppler data at a given altitude look much like a phase plot, as seen in the LDV wind plot (Fig. 5.3). The maximum doppler shift determines the wind direction. To account for instantaneous wind speed differences, the magnitude of the LDV winds are calculated as the scalar average of the wind magnitude moving toward and away from the LDV system. Since data are acquired at a 45° elevation angle, the doppler winds must also be multiplied by the square root of 2, i.e., divided by the *cosine* of 45°. The time to rotate the system through two pi radians is about 5 s. It appears from Fig. 5.3 that the LDV acquires data at about 100 samples per second (I am uncertain about this since that information was not provided me). The LDV winds probably have a minimum uncertainty of about ±0.25 m/s.

The LDV calibration data were acquired in a fixed altitude mode for better comparison with the lidar data. Calibration data were acquired at 100 m, 200 m, 300 m, 400 m, and 500 m (except at 0800 hours on September 10 when calibration data were acquired at 200 m, 300 m, and 400 m). The lidar and LDV operations were

coordinated so that the LDV was focused at each altitude for about 10 minutes while the lidar data acquisition was also concentrated at a similar altitude for the same time period. The LDV was ~1.9 km from the lidar. Due to the 45° elevation of the LDV, LDV data acquired at 100 m represent 5 s time averages across a distance of 200 m. LDV data acquired at 200 m represent 5 s time averages across 400 m, etc.

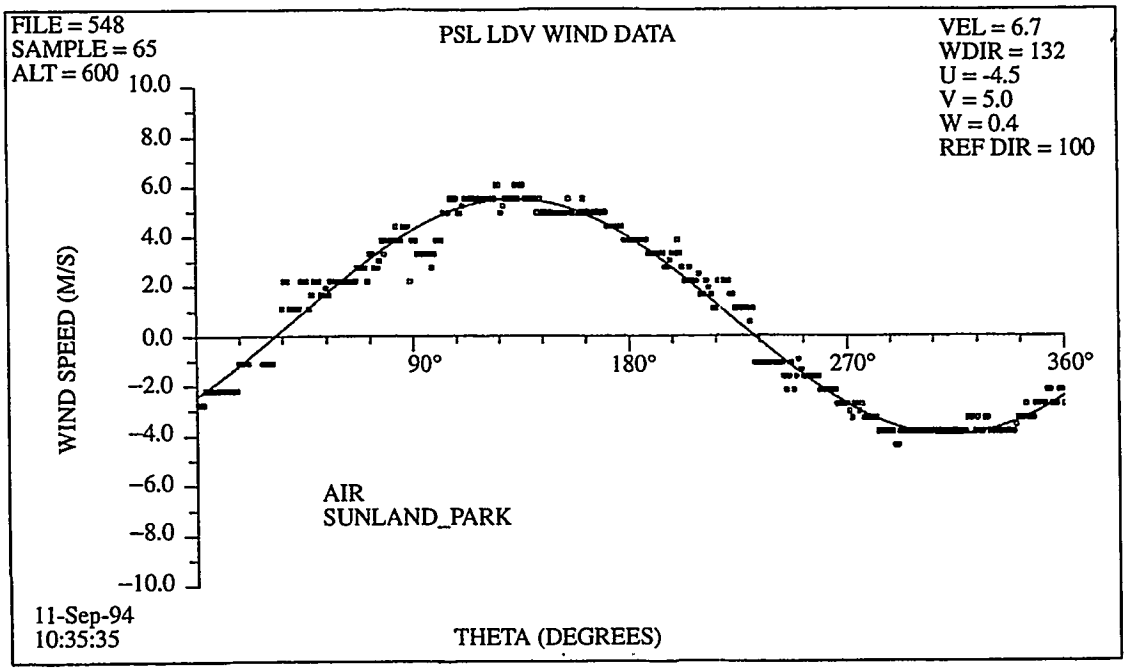

Fig. 5.3: Laser Doppler Velocimeter Doppler Shift Plot

The wind speed (VEL) in the upper right corner is the absolute average of the minimum and maximum wind speeds multiplied by the square root of two, i.e., $ws \approx (5.5 \text{ m/s} + 4.0 \text{ m/s}) \times \sqrt{2}/2 = 6.7$ m/s. The wind direction (WDIR) of 132° in the upper right corner is measured from true north and corresponds to the maximum doppler wind, i.e., the maximum doppler wind was 5.5 m/s in this plot and occurred at 132° from north.

These data were provided courtesy of the Physical Sciences Laboratory of New Mexico State University, Las Cruces, NM 88001, and the US Army Research Laboratory of White Sands Missile Range, NM 88002.

The lidar system differs from the LDV in that lidar winds can be long or short time averages over distances of a few meters to hundreds of meters. Fast wind speeds are shorter time averages than low wind speeds, and transverse winds represent shorter distance averages than winds which are not transverse to the lidar's observation angle. These key differences in the LDV and lidar systems could lead to different results between the two systems. The two systems, however, should give similar results in steady wind conditions.

5-2.1.1 LDV/Lidar Comparison Conclusions

LDV/lidar wind comparisons of calibration data (Figs. 5.4 and 5.5) show strongly correlated results except for Fig 5.4A. The lidar data plotted represent winds acquired at a range of 1,850 ±400 m from the lidar. The LDV/lidar wind comparisons support the validity of the lidar remote wind fields.

The 0800 hour wind speed comparisons agree well at 200 m, but wind speeds differ by as much as 7 m/s at 300 m. At 200 and 400 m altitude, the LDV and lidar wind directions differ by about 20° and at 300 m the wind directions differ by about 40°. These different results do not mean that one of the two systems has incorrectly measured the winds since the LDV and the lidar measure different physical quantities. The LDV measures an instantaneous doppler shift along its observation angle. Thus, although the doppler winds toward and away from the LDV system are averaged to give an estimated wind speed across the diameter of the conical surface, the actual doppler measurement is two instantaneous measurements on the circumference of a

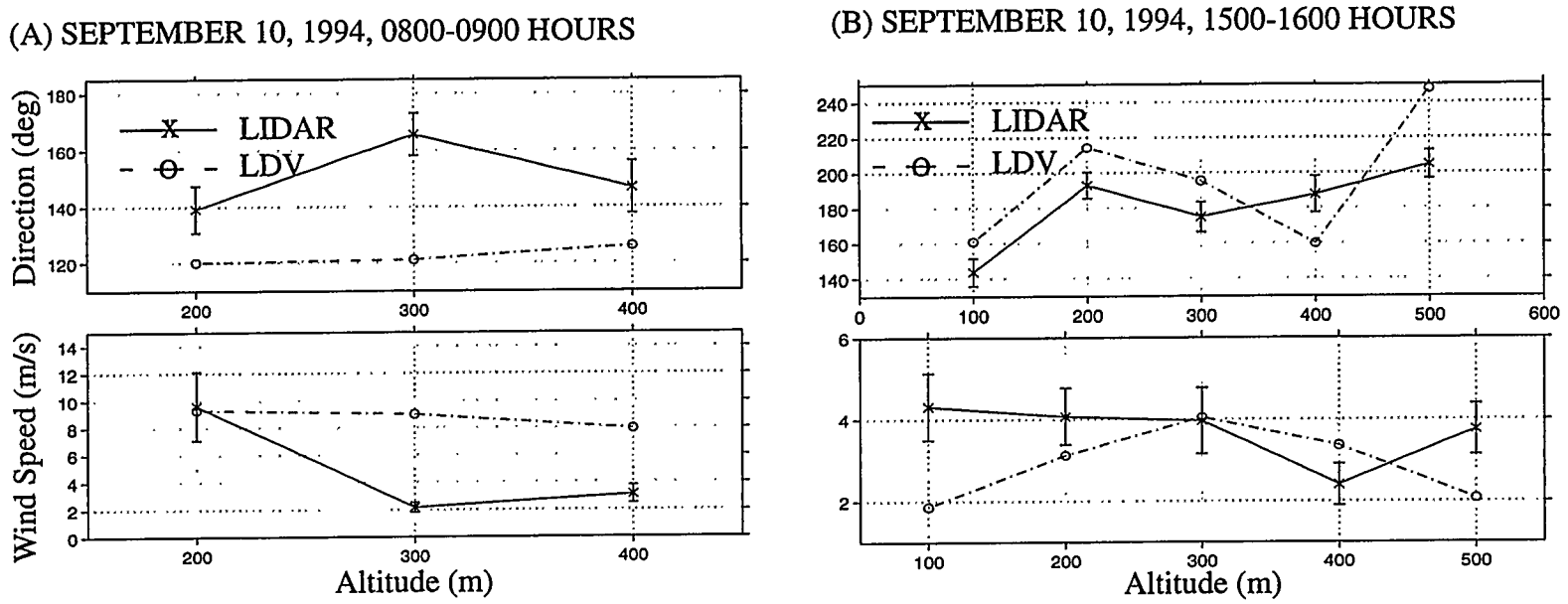

Fig. 5.4: Lidar/LDV Wind Comparisons for September 10, 1994 (Calibration Runs).

Both these lidar and LDV data were unit-vector median filtered. All data within ±5° of the median direction were vector averaged and plotted. Dashed lines marked by an 'o' correspond to LDV data. Solid lines, with error bars and marked by an 'x', correspond to lidar data. LDV wind speed uncertainties are estimated to be about ±0.25 m/s.

(A) The left plots are the 0800 to 0900 hours calibration run and fails to show strongly correlated results. (B) The right plots are the 1500 to 1600 hours calibration run and show good agreement in wind speed and direction.

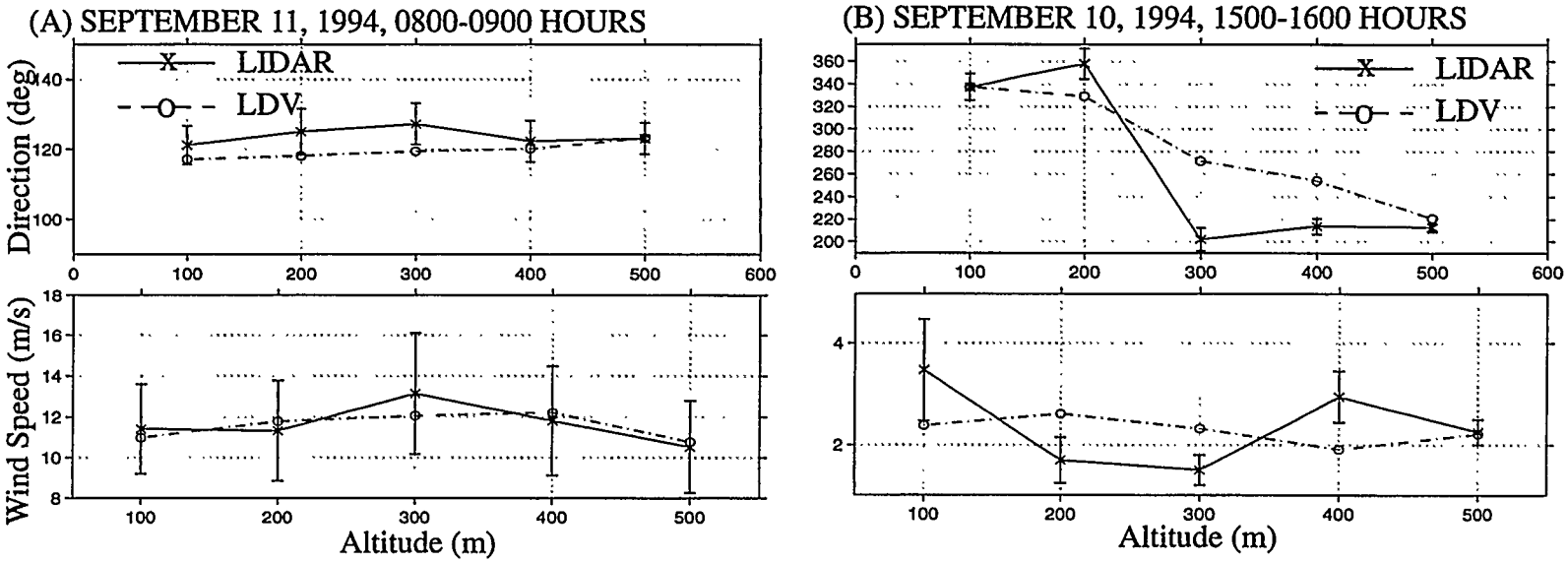

Fig. 5.5: Lidar/LDV Wind Comparisons for September 11, 1994 (Calibration Runs).

Both these lidar and LDV data were unit-vector median filtered. All data within ±5° of the median direction were vector averaged and plotted. Dashed lines marked by an 'o' correspond to LDV data. Solid lines, with error bars and marked by an 'x', correspond to lidar data. LDV wind speed uncertainties are estimated to be about ±0.25 m/s.

(A) The left plots are the 0800 to 0900 hours calibration run and show strongly correlated results. The large uncertainties in the wind speeds are related to the high wind speeds (very fast transport times). (B) The right plots are the 1500 to 1600 hours calibration run and show good agreement in wind speed and direction. Of interest is the wind shear seen by both the LDV and lidar system. The LDV data at 300 and 400 m show wind directions from the lidar's blind spot. This blind spot is discussed in more detail later in this section.

circle whose diameter is twice the height of the measurement (the two measurements are chosen after fitting the LDV data (Fig. 5.3) to a sine function). Thus, the LDV could measure a high wind speed while the lidar is measuring a low wind speed. For instance, an eddy centered almost directly above the LDV could cause the lidar to see different average wind speeds than the LDV.

Between 1500 to 1600 hours on September 10, 1994, the LDV and lidar wind plots generally agree in magnitude and direction (Fig 5.4B). The general shape of the plot of wind directions is similar through the first 300 m even though the directions differ by about 15° at those altitudes. At 500 m altitude, the LDV shows a wind direction of about 248° while the lidar shows a direction near 205°.

One weakness of the three-angle correlation wind algorithm is that winds directly toward or away from the lidar system are not measured because correlations are performed between different observation angles. This cross-correlation algorithm leads to blind spots of about 7.2° toward and away from the lidar system for correlations between observation angles one and two and observation angles two and three, at the range of the LDV from the lidar. The size of the blind spots doubles for correlations between observation angles one and three. The calibration data were acquired with the lidar system observing the airspace at about 247° from north—exactly the direction the winds were observed to be traveling by the LDV system on September 10, 1994. Thus, the lidar cannot see the winds from about 245°±3.6° or from about 65°±3.6° from the north, but will see any winds distributed around these directions.

This weakness does not detract from the usefulness of the lidar winds within the boundary layer since winds come from a variety of directions throughout such a large volume of the atmosphere sampled by the lidar. Furthermore, the lidar system surpasses the LDV, and other remote systems, such as doppler radar profilers and balloons, because they only measure the winds directly above the instrument (or where the device is located at a given time, in the case of the balloon). This limitation may have been a strong motivation for Eloranta (Schols et al. 1992) to move towards three-dimensional data acquisition methods to estimate his lidar winds. (Eloranta's decision may have resulted from other considerations too, such as detector bandwidths, spatial and temporal averages represented by the lidar winds, etc.)

The lidar and LDV winds agree well for 0800 hours data from September 11, 1994 (Fig 5.5A), and the data from 1500 hours also agree well except for the directions at 300 and 400 m. Again, the LDV shows the winds to be near the lidar's blind spot at these altitudes. Both the LDV and lidar systems show a strong shear in the winds between 200 m and 400 m in the data from 1500 hours on September 11, 1994. The ability to detect wind shear is important for air traffic safety.

5-3 Three-Dimensional Lidar Wind Fields

Three-dimensional winds for September 10 and 11, 1994, are plotted above a topographic map of the Mexico/New Mexico/Texas region. The three-dimensional wind plots between 0800 and 0900 hours, and between 1500 and 1600 hours are limited since those hours correspond to the calibration runs. The plots show winds flowing into Sun-

land Park, New Mexico, from Juarez, Mexico, and El Paso, Texas, during time periods preceding peak ozone levels in the Sunland Park region (Kennedy et al. 1994).

Winds are plotted in three-dimensional averaging cells. The depth of the three-dimensional averaging cells varies but the sides of each cell are 500 m. All wind vectors which fell within an averaging cell's boundaries were unit-vector median filtered, as described earlier, and the vector average of all the cell's wind vectors within ±5° of the resulting median direction was plotted. The three-dimensional lidar wind plots (Figs. 5.6 to 5.21) were processed as discussed in Ch. 4 and section 5-2 of this chapter.

Between two and five wind fields for each hour are plotted. Each wind field plotted is associated with a different altitude level. The data are sparse for the first hour from September 10, 1994, because data acquisition was behind schedule for that day. As a result, only two altitude levels of data were plotted. The rest of the wind fields for September 10 contain at least three altitude levels of wind fields, and the wind fields between 1300 to 1400 hours, and 1400 to 1500 hours include a fourth altitude level plotted in red.

The first and last hours of wind fields from September 11 contain only two altitude levels of data, because the winds were steady in the lowest 400 m above the lidar between 0800 to 0900 hours and were also steady in the lowest 200 m between 1500 to 1600 hours. The rest of the data from September 11 includes three plots for each hour with three or four altitude levels except for the wind fields acquired between

1400 to 1500 hours which includes four wind-field plots and five different altitude levels. Data acquired between 0900 to

1000 hours, 1100 to 1200 hours, 1200 to 1300 hours, and 1300 to 1400 hours on September 11 contain three plots with four different altitude levels. The volume represented by each plot varies, but the altitudes of wind vectors, relative to the lidar's altitude are marked at the bottom left corner of each plot.

Each plot contains statistics for the vector field plotted. The statistics quoted for each plot are the scalar-average wind speed and the standard deviation of the scalar averaged wind speed, the minimum and maximum wind speed for the vector plot, the scalar-average direction and its standard deviation. Low standard deviations indicate steady, or low variability, winds.

The number of vectors which fell within each averaging cell varied from as few as three vectors to as many as a few hundred vectors. This poses a question of import to atmospheric modelers. Most atmospheric wind models generate fields with long time averages and large spatial averages (with the exception of large eddy simulations). Many models use a "nested grid" with variable depths (similar to the variable depth averaging cells discussed earlier). These nested grids might be 2 km on a side near the edges of the modeled region and be 1 km on a side in the interior of the modeled region (thus the term *nested* grid). Thus, the interior grid is four times the area of my 1/2 km per side averaging cells. This gives a large spatial average and small-scale motions are neglected. This means turbulent eddies are difficult to generate (except

with large eddy simulations), especially since only one vector per hour is generated—thus the long time and spatial average. This algorithm leads to very smooth results and atmospheric modelers interested in comparing modeled wind fields to lidar wind fields will be interested to know the time and spatial averages represented by the lidar wind fields. The time average represented by each averaging cell can vary between a few minutes to as many as 30 minutes depending on the cell's proximity to the lidar, the cell's altitude level, the volume of the cell, and the cell's proximity to the boundaries or border of the plotted lidar wind field. Cells near the boundary or border of the lidar wind fields likely represent short time averages, but cells within the interior of the lidar wind fields could vary from 10 to as much as 30 minute time averages.

5-4 Discussion

Atmospheric meteorological modelers are generally interested in large range scale and long time scale structure in the boundary layer. Also of interest are the geostrophic winds Geostrophic winds are above the boundary layer, are minimally affected by turbulence usually, and are slowly varying with time, direction and magnitude.

There are three basic types of meteorological modeling. Hydrostatic, non-hydrostatic, and large eddy simulations. These models can be predictive (prognostic), or they can use actual measurements to estimate meteorological conditions over a wide area (diagnostic). Hydrostatic models assume that gravitational and pressure

forcings balance each other so that over long time periods vertical motions negligible and winds move parallel to the local terrain.

All of the models are depicted in the lidar winds. Recall that lidar data were acquired at eight different azimuthal angles and five different elevation angles each hour. This is a total of 40 unique sets of backscatter records, or sets of observation angles, with each set occurring during a 62 s time period. Individual wind measurements within each set of observations may represent 5 to 20 s time averages across distances of tens to hundreds of meters, and there could well be more than 100 unique measurements, during different time periods at similar ranges, from one or more observations. Winds for each observation angle approach 45 s time averages.

Data at the perimeter of the lidar's range may best depict large eddy simulations, for example, the eddy just southwest of Sierra de Cristo Rey (Fig. 5.10). A similar eddy appeared at this location at other times. The data in this area of the lidar scans represent perimeter data and as such depict short time scale structures.

Data within the interior of the wind fields can represent time averages on the order of 5 to 30 minutes. The time average will depend on the depth of the cell and the proximity of the measurement to the lidar. For instance, low-, medium-, and high-altitude data within a few kilometers of the lidar, with cell depths of 200 to 500 m, could represent statistical averages of 100 to 200 wind vectors acquired at two or more elevation angles. Lidar wind vectors determined from multiple elevation angles will be comparable to long time scale and large range scale wind vectors generated by meteo-

rological wind models. (Recall that each averaging cell was 500 m on a side, and that all wind vectors which fell within the cell were unit-vector median filtered to determine the median direction, and that all vectors within ±5° of the median direction were vector averaged to give an average wind for the cell.)

Future calculations of velocity potentials and stream lines from the lidar wind fields may resolve hydrostatic balance. Many of the images, however, do not represent divergence-free wind fields (the lowest 300 m, or lowest altitude level, in Fig. 5.12, for example). Hydrostatically-balanced wind fields are non-divergent throughout the entire field. A diverging wind field would imply a vertical component to the winds. In the hydrostatic approximation there are no vertical winds. Thus, these lidar data do not always depict hydrostatic balance. (Note that the updraft depicted in Fig. 5.12, and discussed in the Fig. 5.12 caption, persisted for at least 10 to 15 minutes. The updraft was imaged in the vertical scan about 10 or 15 minutes before the wind field data were acquired, and the diverging field is about where the mean winds would have carried the cloud and its updraft.)

Finally, wind patterns which persist from hour to hour, or level to level, must be considered as long time scale wind patterns and should be predicted by prognostic models. For those persistent wind patterns, the general trend of the wind vectors should depict the mean wind for those levels and those hours. Persistent wind patterns were frequently observed over Sunland Park at many altitude levels.

(A) $v = (7.7 \pm 3.4)$ m/s
$(2.0 \leq v \leq 10.4)$ m/s
$\Theta = 148.6° \pm 9.6°$

(B) $v = (4.2 \pm 4.7)$ m/s
$(1.0 \leq v \leq 14.9)$ m/s
$\Theta = 170.3° \pm 46.8°$

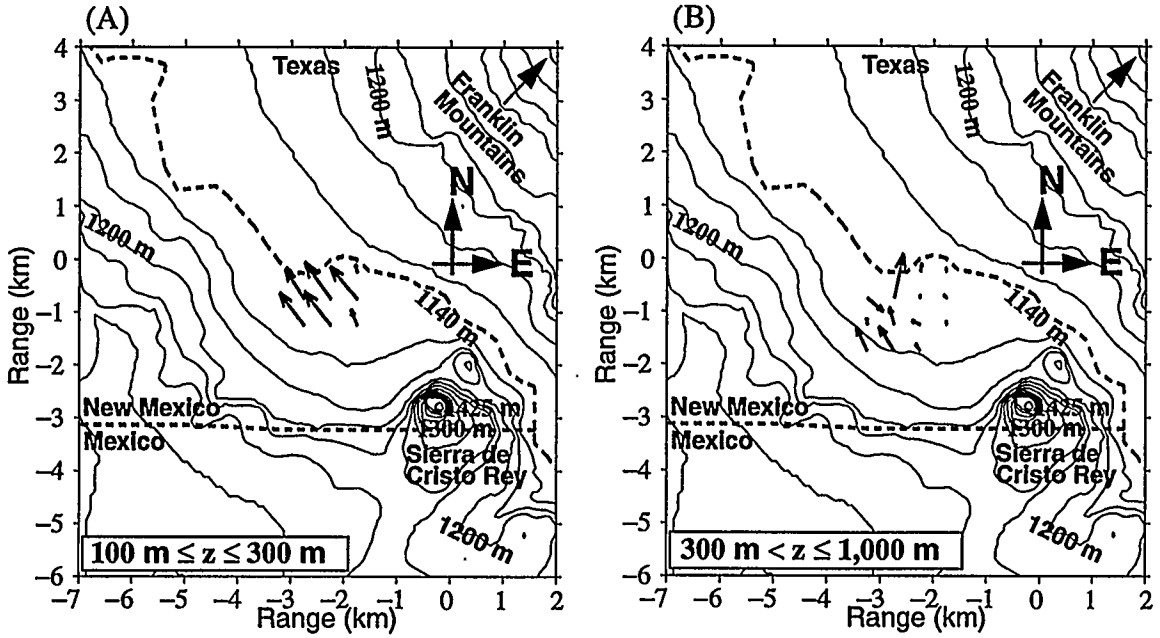

Fig. 5.6: Lidar Winds From 0800 to 0900 Hours (September 10, 1994 Calibration Run)

(A) Lowest level altitudes shows moderate to strong SE winds with moderate variabilities in magnitudes and low variabilities in directions. This low level wind pattern is seen in Figs 5.7A to 5.10A and Figs 5.14A to 5.17A and is evidence of "up-river" flow caused thermal heating of the earth surface. (B) Higher altitudes shows winds with high variabilities in magnitude and direction. There is an eddy over the Sunland Park race track area near the PSL LDV position. This may account for the poor agreement between the lidar and the LDV wind results. This type of eddy could produce a stagnant region and is evidence of terrain induced turbulence. (Note that a similar eddy appeared at this same time and similar altitudes on September 11, 1994 (Fig. 5.14B). This suggests that the eddy could be a structure which appears regularly for extended time periods during early mornings in the Sunland Park area.)

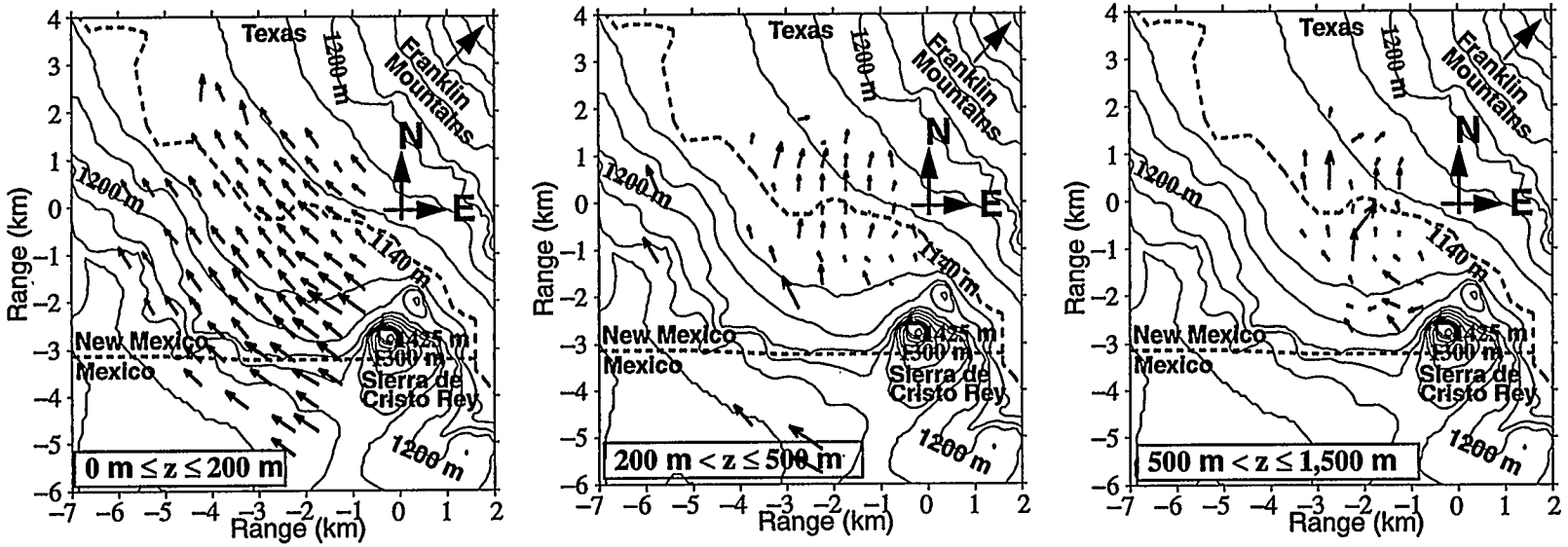

(A) v = (8.3 ± 2.2) m/s
(1.4 ≤ v ≤ 15.0) m/s
Θ = 137.1° ± 12.0°

(B) v = (4.0 ± 2.5) m/s
(0.6 ≤ v ≤ 11.3) m/s
Θ = 177.9° ± 37.4°

(C) v = (2.7 ± 2.3) m/s
(0.8 ≤ v ≤ 13.0) m/s
Θ = 167.3° ± 38.0°

Fig. 5.7: Lidar Winds From 0900 to 1000 Hours (September 10, 1994)

(A) The lowest level shows no thermal turbulence and moderate to strong terrain following SE winds from El Paso, Texas, and Juarez, Mexico, with low variabilities in magnitudes and directions. (B) and (C) Show stagnant winds just northwest of Sierra de Cristo Rey with winds which curl toward low speed S winds that travel toward the Franklin Mountains. This wind pattern appears in both (B) and (C) suggesting that this could be a persistent structure affecting aerosol transport into the Sunland Park area. These middle- and upper-level patterns appear in several of the plots which follow (e. g., Figs. 5.8 and 5.9). (C) Upper-level winds are low in magnitude with high variabilities in magnitude and moderate directional variabilities. The high variabilities are caused by the terrain induced turbulence at the level of the Sierra de Cristo Rey.

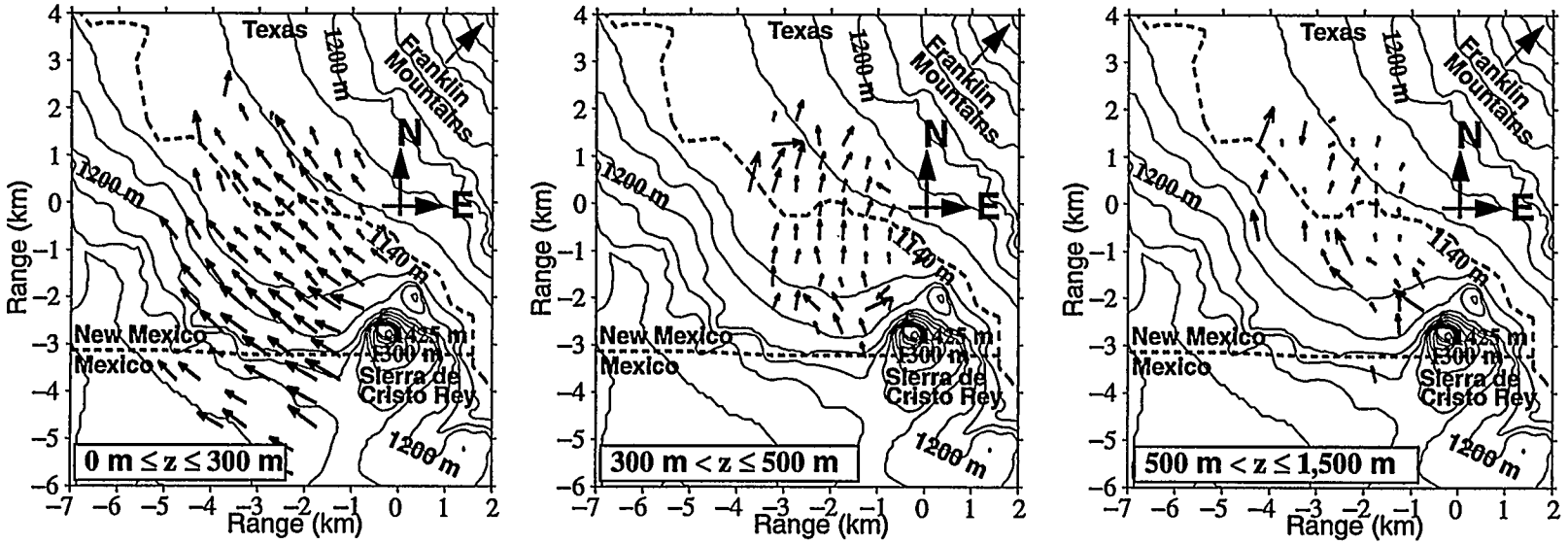

(A) v = (6.1 ± 1.7) m/s
(1.8 ≤ v ≤ 9.7) m/s
Θ = 135.6° ± 15.8°

(B) v = (3.9 ± 1.4) m/s
(1.8 ≤ v ≤ 9.5) m/s
Θ = 184.2° ± 32.3°

(C) v = (3.4 ± 2.2) m/s
(1.0 ≤ v ≤ 9.2) m/s
Θ = 171.2° ± 38.6°

Fig. 5.8: Lidar Winds From 1000 to 1100 Hours (September 10, 1994)

These three plots are similar to plots from the previous hours indicating steady wind patterns. (A) Low altitudes shows moderate terrain following SE winds. (B) Middle altitude winds are low to moderate in magnitudes from the south with moderate directional variabilities. The moderate directional variabilities indicate terrain induced turbulence caused by the Sierra de Cristo Rey. (C) Upper altitude plot shows a possible stagnant zone with more terrain induced turbulence at the level of the Sierra de Cristo Rey.

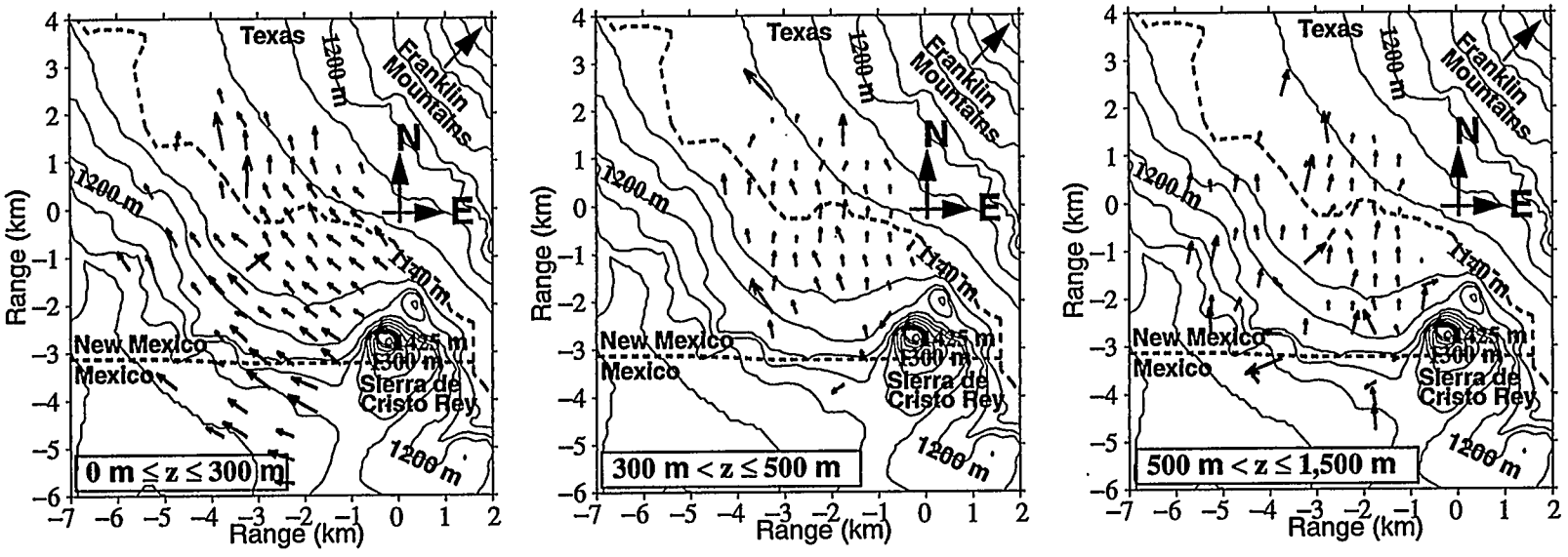

(A) $v = (5.0 \pm 1.7)$ m/s
$(1.9 \le v \le 11.2)$ m/s
$\Theta = 141.0° \pm 22.5°$

(B) $v = (3.9 \pm 2.1)$ m/s
$(1.1 \le v \le 12.3)$ m/s
$\Theta = 167.6° \pm 35.4°$

(C) $v = (3.8 \pm 1.9)$ m/s
$(0.7 \le v \le 10.4)$ m/s
$\Theta = 177.8° \pm 33.1°$

Fig. 5.9: Lidar Winds From 1100 to 1200 Hours (September 10, 1994)

These plots look similar to the two previous hours' data. (A) Lowest altitude winds are SE with moderate magnitude, low directional variabilities, with no evidence of thermal turbulence. (C) Upper level winds are low to moderate in magnitude with moderate variabilities, are from the south with moderate directional variabilities, show possible stagnant regions over Sunland Park, and continue to exhibit terrain induced turbulence. Middle (B) and upper (C) level winds seem to be mostly from the south. Upper level (C) shows terrain induced turbulence.

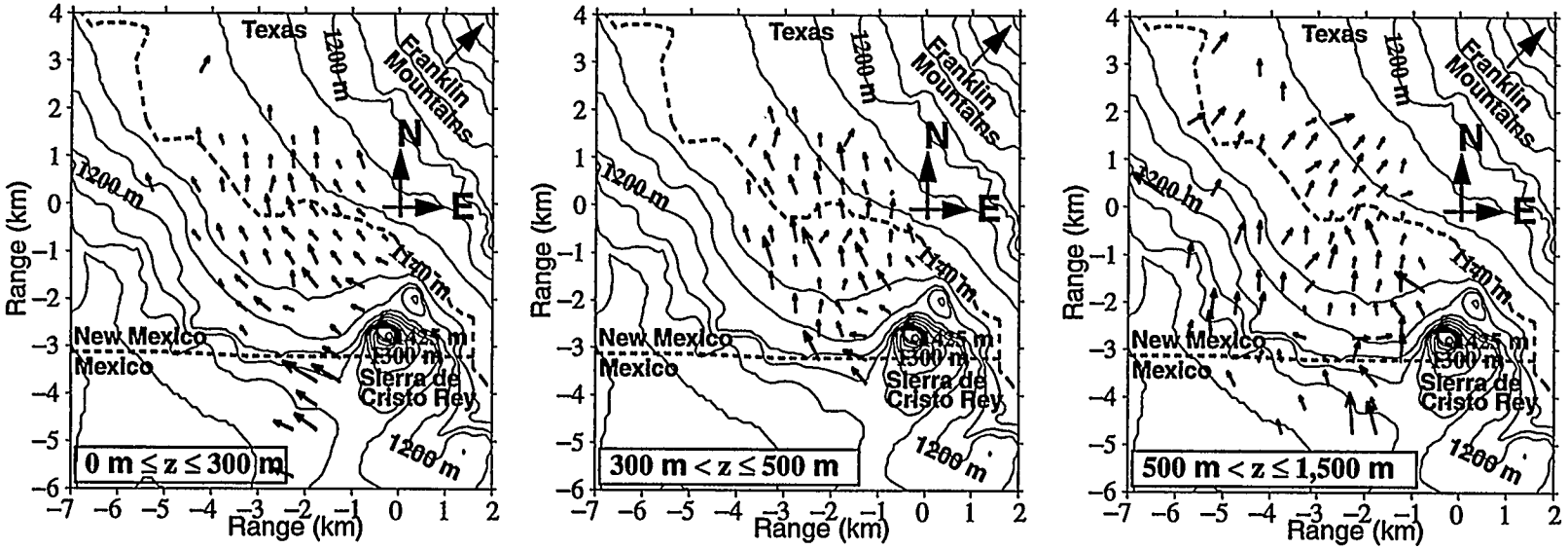

(A) v = (4.2 ± 1.6) m/s
(1.7 ≤ v ≤ 10.9) m/s
Θ = 148.0° ± 22.0°

(B) v = (3.5 ± 1.3) m/s
(0.7 ≤ v ≤ 8.4) m/s
Θ = 167.0° ± 25.0°

(C) v = (4.3 ± 1.7) m/s
(1.8 ≤ v ≤ 9.9) m/s
Θ = 191.5° ± 31.0°

Fig. 5.10: Lidar Winds From 1200 to 1300 Hours (September 10, 1994)

(A) Lower level winds show low to moderate magnitude with moderate variabilities (the moderate variabilities indicate that thermal turbulence has begun). These winds seem to curl toward the Franklins as the winds travel up the Rio Grande Valley. Near the pass, and south of Sierra de Cristo Rey, the winds continue to be from the SE. (B) Middle level winds are similar to the previous hour's data in magnitude, direction, variabilities, and continue to exhibit terrain induced effects. (C) Upper level winds show a interesting eddy just west of Sierra de Cristo Rey that is likely a short time scale structure. Similar eddies appear in this region at other times, however, suggesting eddies in this area may be common. The rest of the upper level winds show low to moderate winds with moderate variabilities in direction and low variabilities in magnitude. The upper level winds mainly travel from the south and curl toward the Franklins.

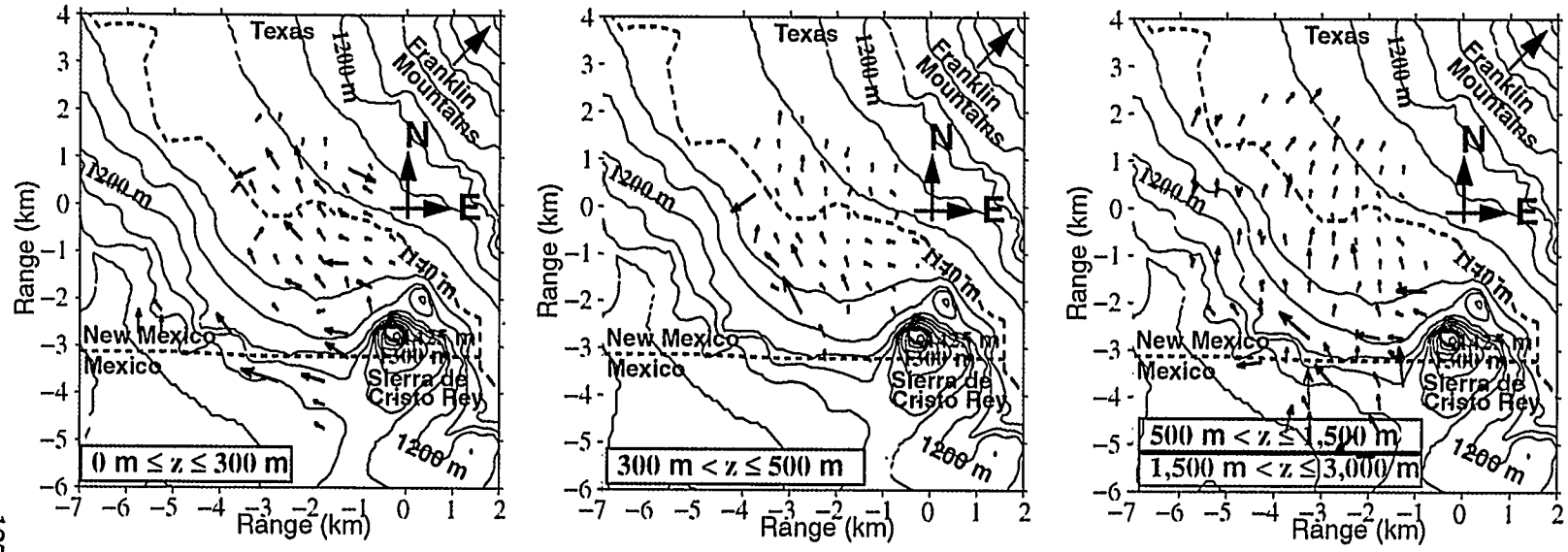

(A) v = (4.0 ± 2.1) m/s
(1.4 ≤ v ≤ 11.2) m/s
Θ = 145.2° ± 40.0°

(B) v = (3.9 ± 2.6) m/s
(0.8 ≤ v ≤ 15.7) m/s
Θ = 150.9° ± 37.7°

(C) v = (4.3 ± 2.3) m/s
(0.8 ≤ v ≤ 12.6) m/s
Θ = 174.4° ± 34.4°

Fig. 5.11: Lidar Winds From 1300 to 1400 Hours (September 10, 1994)

(A) Lower level winds are low to moderate in magnitude with moderate variabilities in magnitude and moderate to high variabilities in direction. Thermal turbulence is evident. Air motions are from El Paso and Juarez into Sunland Park with some possible stagnation. (B) Middle level winds shows similar direction and magnitude with stagnant regions in the Sunland Park area. (C) Upper level winds shows an eddy near Sierra de Cristo Rey (as the prior hour shows) with low to moderate winds curling from the southeast toward the Franklins. Terrain induced turbulence persists. The fourth level's winds, denoted by the red vectors, are mostly from the south and agree in magnitude and direction with a PSL radar profiler positioned about 4 km W and 1.5 km S of the lidar.

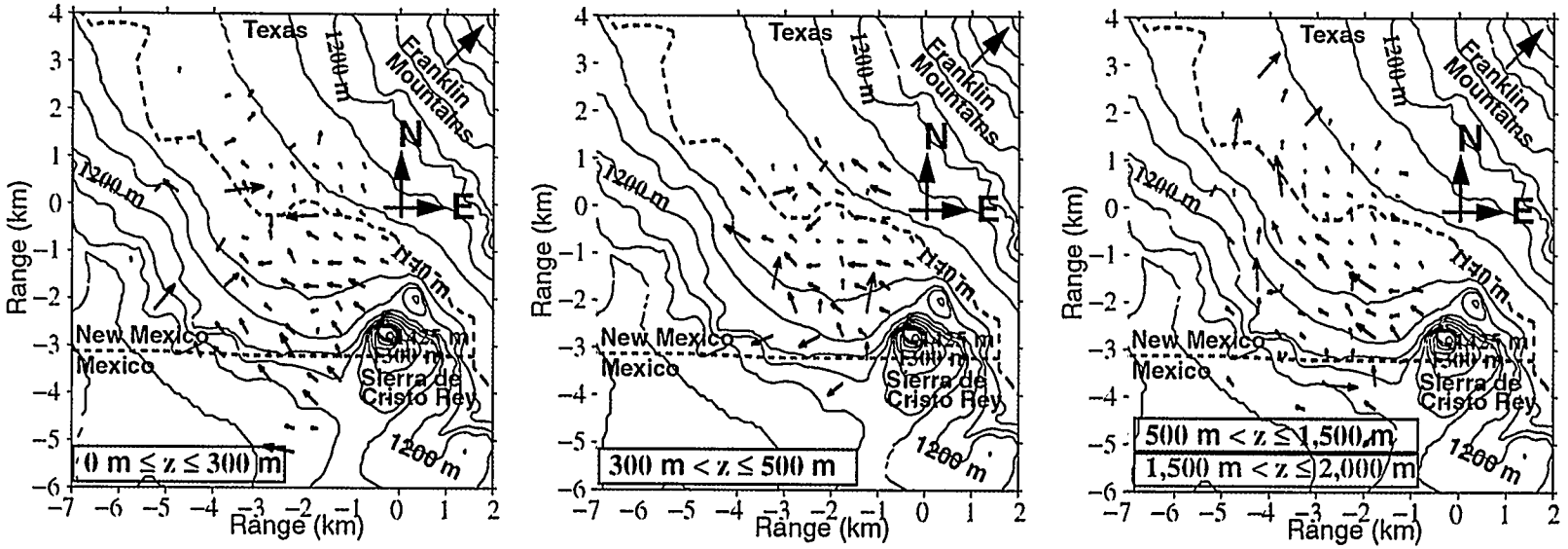

(A) $v = (4.6 \pm 2.7)$ m/s
$(1.3 \le v \le 15.2)$ m/s
$\Theta = 139.5° \pm 49.1°$

(B) $v = (4.8 \pm 2.7)$ m/s
$(1.3 \le v \le 14.3)$ m/s
$\Theta = 130.0° \pm 44.7°$.

(C) $v = (5.1 \pm 3.2)$ m/s
$(1.0 \le v \le 17.8)$ m/s
$\Theta = 154.9° \pm 43.6°$

Fig. 5.12: Lidar Winds From 1400 to 1500 Hours (September 10, 1994)

(A) Evidence of an updraft is seen approximately 4.5 km W of the lidar in the lower level plot. The updraft is revealed as diverging vectors from this region. The sixth vertical scan shown in Appendix D (also in Ch. 3) lends credibility to this assertion. The updraft is a structure that persisted for at least 15 to 20 minutes since wind data were acquired that much later. Otherwise, low to moderate winds appear to be spewing into Sunland Park from El Paso at all levels, i.e., (A), (B), and (C). Air movements are also from Juarez. (C) Stagnant regions were seen in the upper levels. Winds at all levels curl toward the Franklins, and all winds show moderate to high directional variabilities suggested deep turbulent mixing.

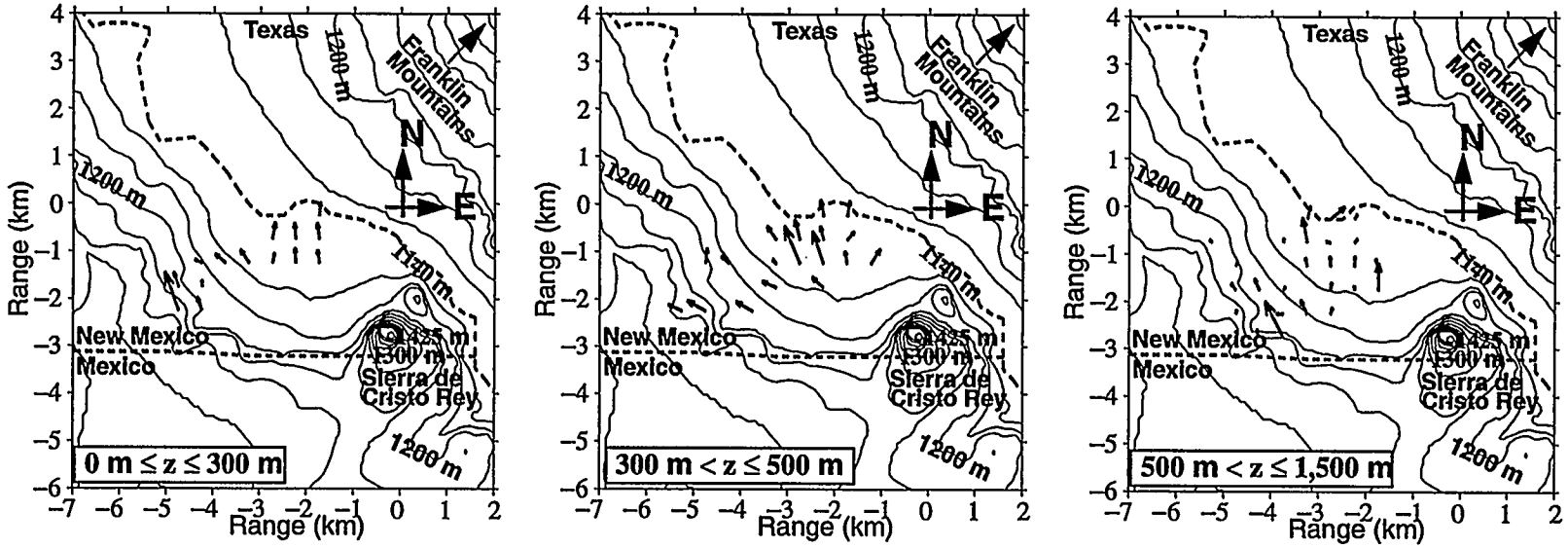

(A) $v = (4.4 \pm 2.3)$ m/s
$(1.8 \le v \le 11.6)$ m/s
$\Theta = 164.7° \pm 23.0°$

(B) $v = (3.6 \pm 1.6)$ m/s
$(1.1 \le v \le 8.2)$ m/s
$\Theta = 156.2° \pm 32.3°$

(C) $v = (4.6 \pm 3.9)$ m/s
$(1.4 \le v \le 17.6)$ m/s
$\Theta = 173.8° \pm 33.5°$

Fig. 5.13: Lidar Winds From 1500 to 1600 Hours (September 10, 1994 Calibration Run)

At this time of the day, winds are mostly due south with moderate directional variabilities and moderate to high variabilities in magnitude. There may have been some stagnation in the upper level (C).

(A) $v = (11.4 \pm 1.7)$ m/s
$(6.6 \leq v \leq 15.5)$ m/s
$\Theta = 127.0° \pm 5.4°$

(B) $v = (10.2 \pm 3.2)$ m/s
$(3.1 \leq v \leq 14.2)$ m/s
$\Theta = 115.2° \pm 41.7°$

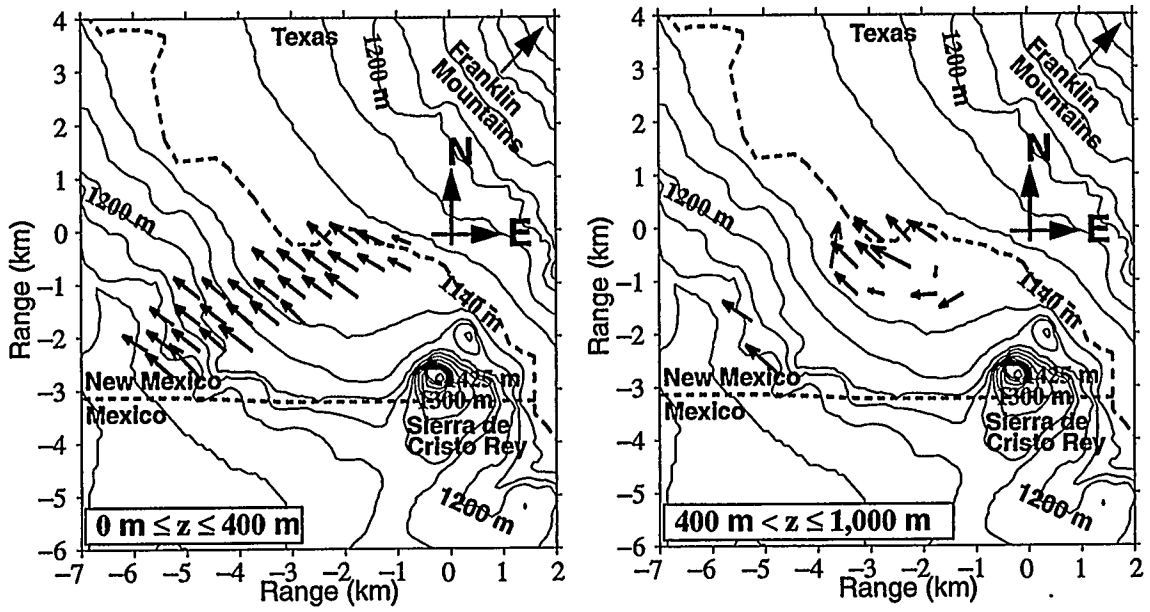

Fig. 5.14: Lidar Winds From 0800 to 0900 Hours (September 11, 1994 Calibration Run)

(A) Winds in the lowest 400 m are from the southeast, high in magnitude, and show low variabilities indicating no thermal turbulence. (B) Upper level winds show an eddy above the Sunland Park downs. This structure is a terrain induced effect and was seen at the same time on September 10, 1994 (Fig. 5.6B). Upper level winds are high with moderate variabilities in magnitude and high variabilities in direction.

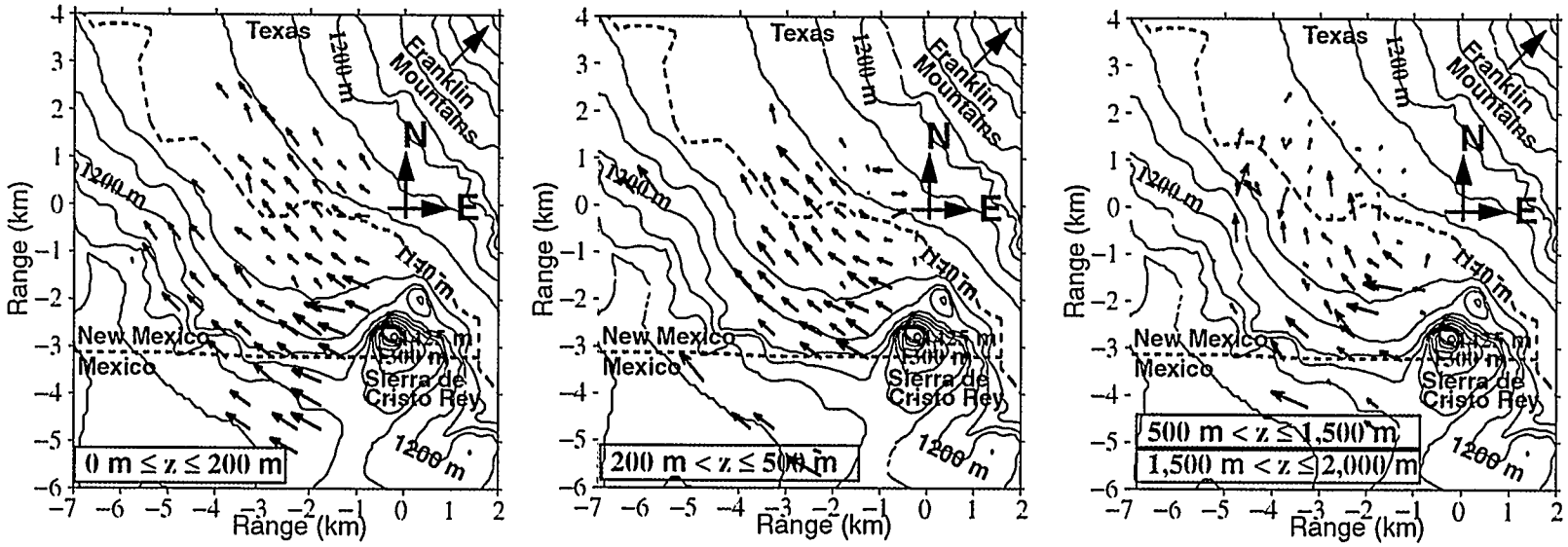

(A) $v = (8.5 \pm 2.7)$ m/s
$(2.0 \le v \le 16.4)$ m/s
$\Theta = 132.1° \pm 13.5°$

(B) $v = (8.0 \pm 3.4)$ m/s
$(0.6 \le v \le 16.1)$ m/s
$\Theta = 138.0° \pm 28.4°$

(C) $v = (4.0 \pm 2.6)$ m/s
$(0.6 \le v \le 11.6)$ m/s
$\Theta = 163.5° \pm 43.9°$

Fig. 5.15: Lidar Winds From 0900 to 1000 Hours (September 11, 1994)

(A) As during the previous day at this hour (Fig. 5.7A), lower level winds are up-pass from El Paso and SE from Juarez. Lower and middle level (B) winds continue to be high in magnitude with low to moderate variabilities, respectively. A stagnant region is seen about 1 km west of the lidar's position in (B). The stagnant region persists in (C) and winds in this plot originated from Juarez and El Paso and curl toward the Franklins. (C) Upper level winds are moderate in magnitude with moderate variabilities and show high variabilities in direction. The high directional variabilities indicate terrain induced turbulence. The higher level winds, denoted by the red vectors (C), also originate from Juarez and curl towards the Franklins.

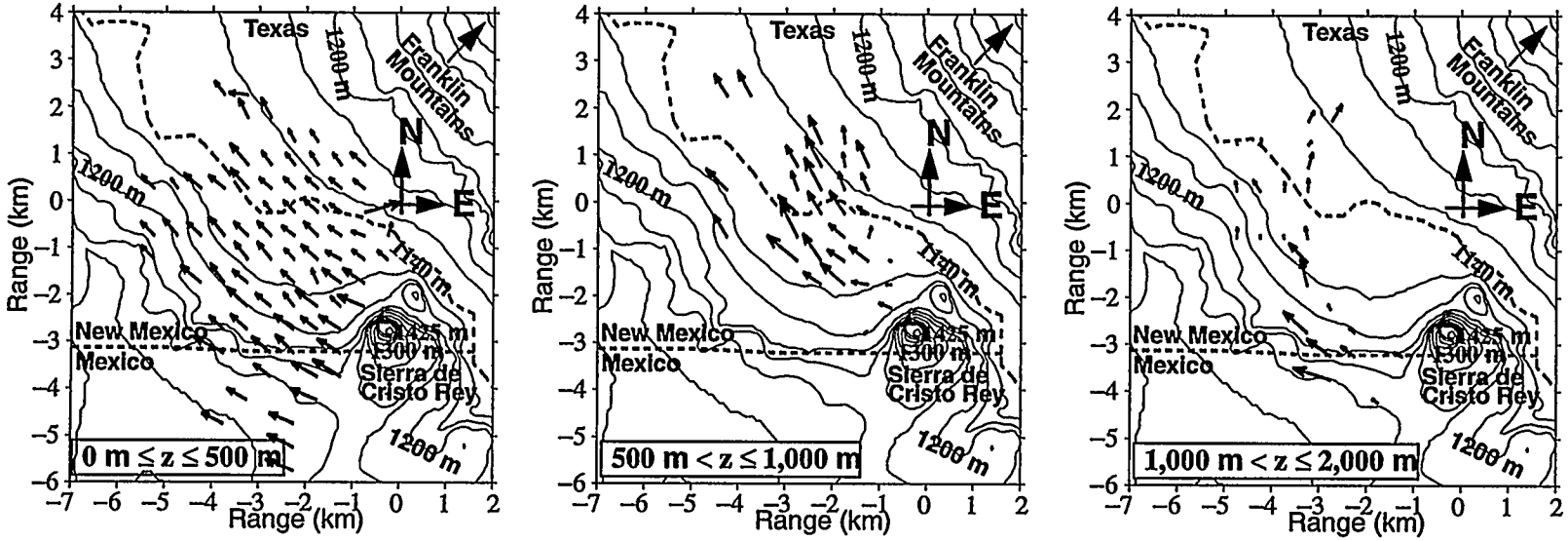

(A) $v = (7.7 \pm 2.0)$ m/s
$(4.4 \leq v \leq 14.4)$ m/s
$\Theta = 133.0° \pm 19.1°$

(B) $v = (6.7 \pm 2.8)$ m/s
$(0.9 \leq v \leq 11.6)$ m/s
$\Theta = 138.7° \pm 26.5°$

(C) $v = (4.4 \pm 3.0)$ m/s
$(1.2 \leq v \leq 11.9)$ m/s
$\Theta = 162.3° \pm 32.3°$

Fig. 5.16: Lidar Winds From 1000 to 1100 Hours (September 11, 1994)

(A) Lower level winds are terrain following, moderate to high in magnitude with low variabilities, and show moderate directional variabilities. Lower level winds travel up-pass from El Paso, are SE from Juarez, and do not exhibit thermal turbulence. (B) Middle level winds are moderate in magnitude with moderate variabilities in both magnitude and direction and enter Sunland Park from El Paso. A stagnant region is at the mouth of the pass. (C) Upper level winds depict a stream flowing from Juarez which sharply curls toward the Franklins with moderate directional variabilities and high variabilities in magnitude.

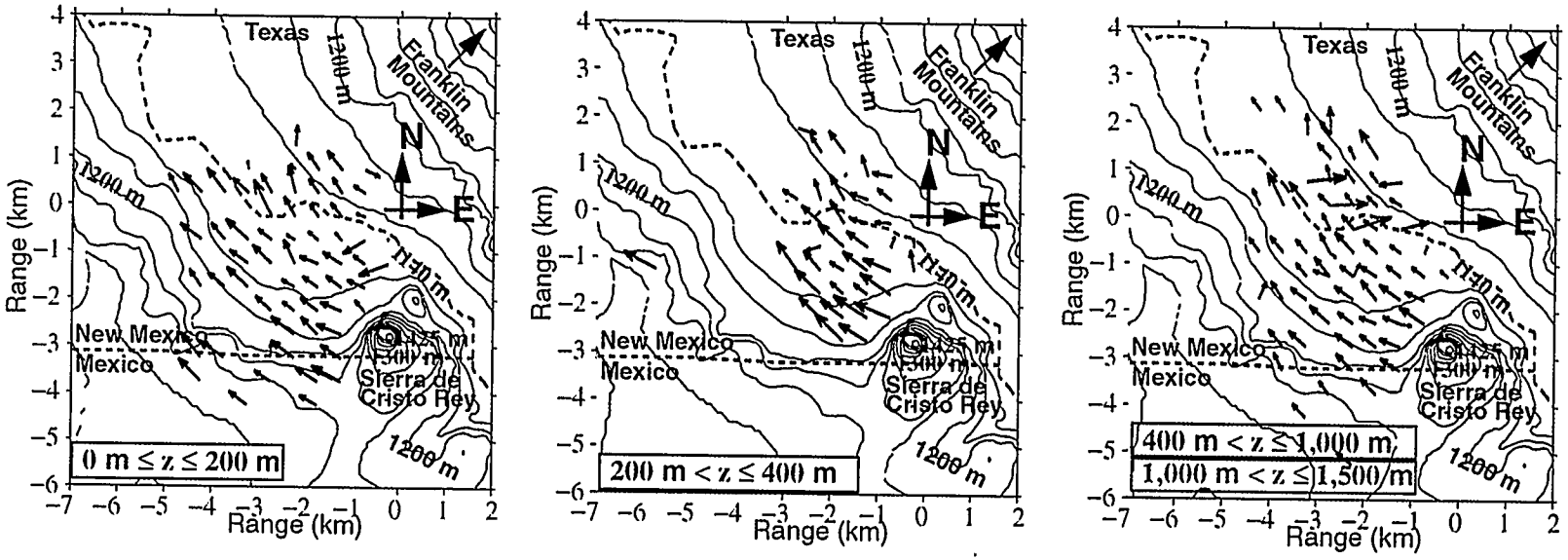

(A) v = (6.5 ± 2.2) m/s
(0.7 ≤ v ≤ 12.4) m/s
Θ = 134.8° ± 29.1°

(B) v = (5.1 ± 1.9) m/s
(0.6 ≤ v ≤ 8.3) m/s
Θ = 137.9° ± 37.4°

(C) v = (6.6 ± 2.2) m/s
(1.6 ≤ v ≤ 13.6) m/s
Θ = 149.3° ± 43.0°

Fig. 5.17: Lidar Winds From 1100 to 1200 Hours (September 11, 1994)

(A) Lower level winds change little from the previous hours' winds. The lower and middle level (B) winds, however, decrease in magnitude but continue to show moderate variabilities in magnitude and direction. Winds at all levels continue to travel into the Sunland Park region from El Paso and Juarez. (C) Upper level winds show high directional variabilities.

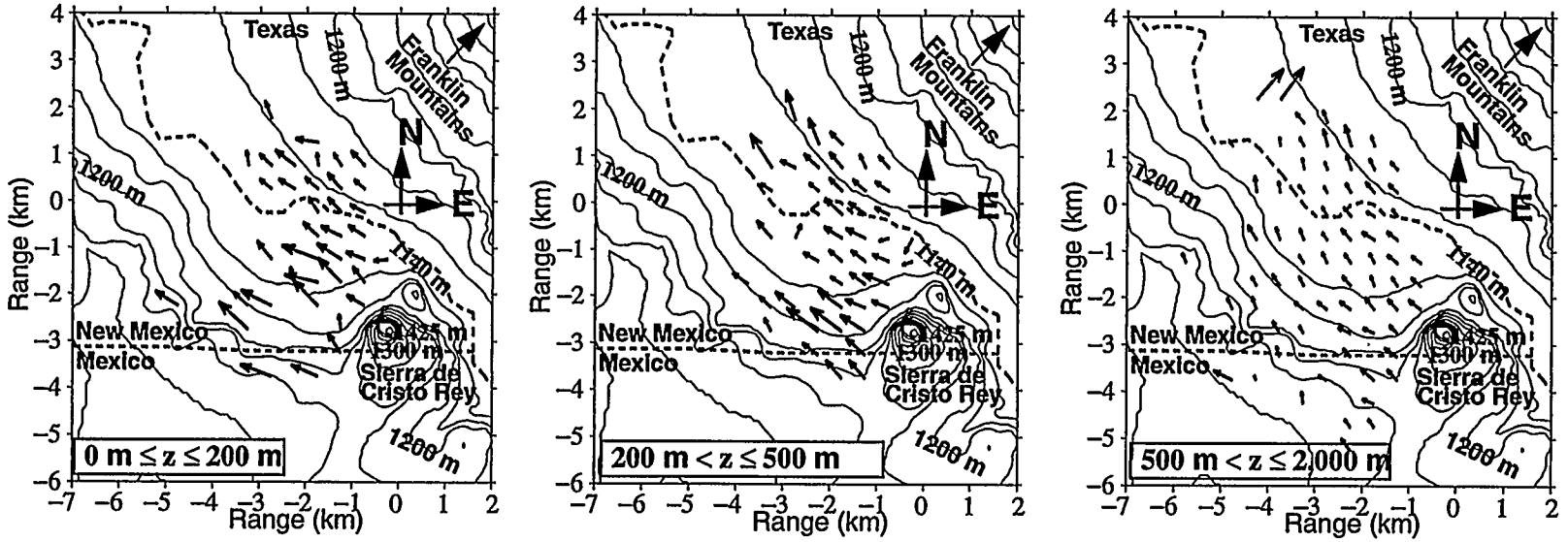

(A) v = (5.9 ± 2.0) m/s
(3.4 ≤ v ≤ 10.4) m/s
Θ = 130.7° ± 19.8°

(B) v = (6.2 ± 2.2) m/s
(2.9 ≤ v ≤ 12.1) m/s
Θ = 126.5° ± 25.0°

(C) v = (5.8 ± 2.3) m/s
(2.0 ≤ v ≤ 17.5) m/s
Θ = 149.8° ± 19.5°

Fig. 5.18: Lidar Winds From 1200 to 1300 Hours (September 11, 1994)

(A) Lower level winds are exhibiting thermal turbulence. Winds at all levels are moderate in magnitude with moderate variabilities in both direction and magnitude. Winds continue to travel from El Paso and Juarez into Sunland Park.

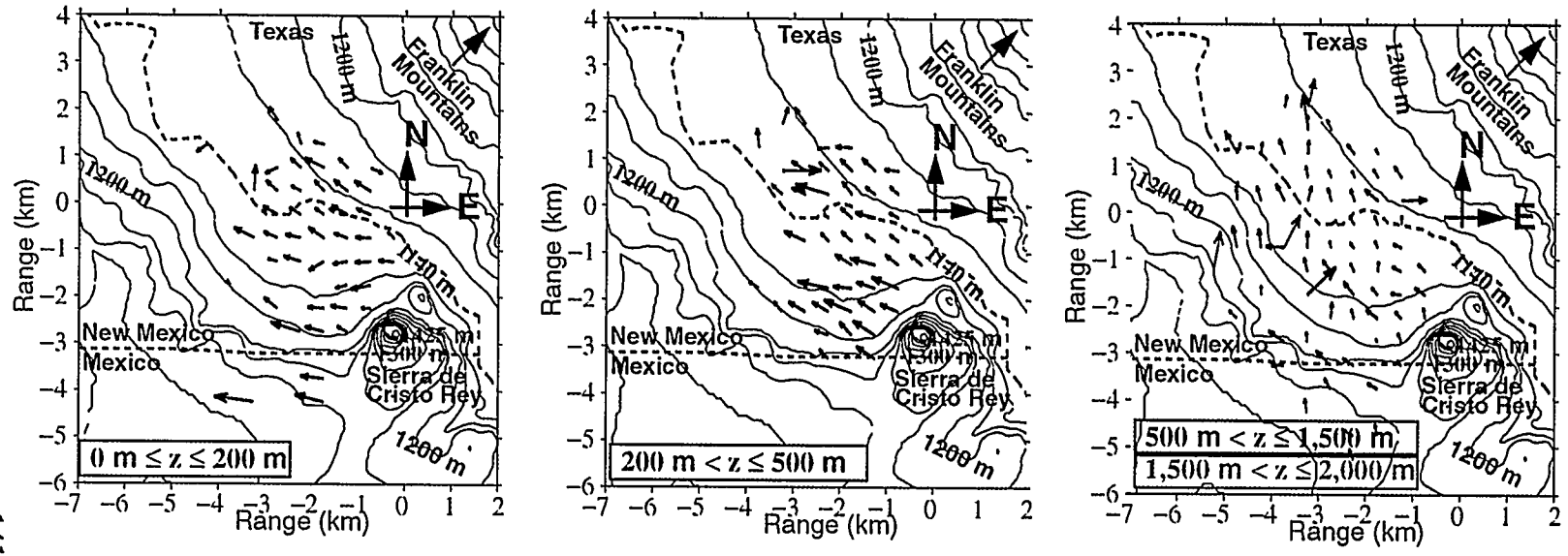

(A) v = (5.2 ± 1.9) m/s
(1.8 ≤ v ≤ 12.5) m/s
Θ = 114.8° ± 36.9°

(B) v = (4.9 ± 1.8) m/s
(1.7 ≤ v ≤ 10.6) m/s
Θ = 126.6° ± 28.9°

(C) v = (5.2 ± 2.5) m/s
(1.4 ≤ v ≤ 16.7) m/s
Θ = 159.3° ± 31.0°

Fig. 5.19: Lidar Winds From 1300 to 1400 Hours (September 11, 1994)

(A) Thermal turbulence is evident and lower level winds are mostly east from El Paso into Sunland Park. Winds appear spewing out of the pass as if from a jet nozzle. Winds from Juarez are easterly and do not seem to enter the Sunland Park area. Winds at all levels are moderate in magnitude and variabilities. (C) Upper level winds are traveling into the Sunland Park region from both El Paso and Juarez and may stagnate over Sunland Park. The extreme upper level winds, denoted by the red vectors, agree in magnitude and direction with the PSL radar profiler.

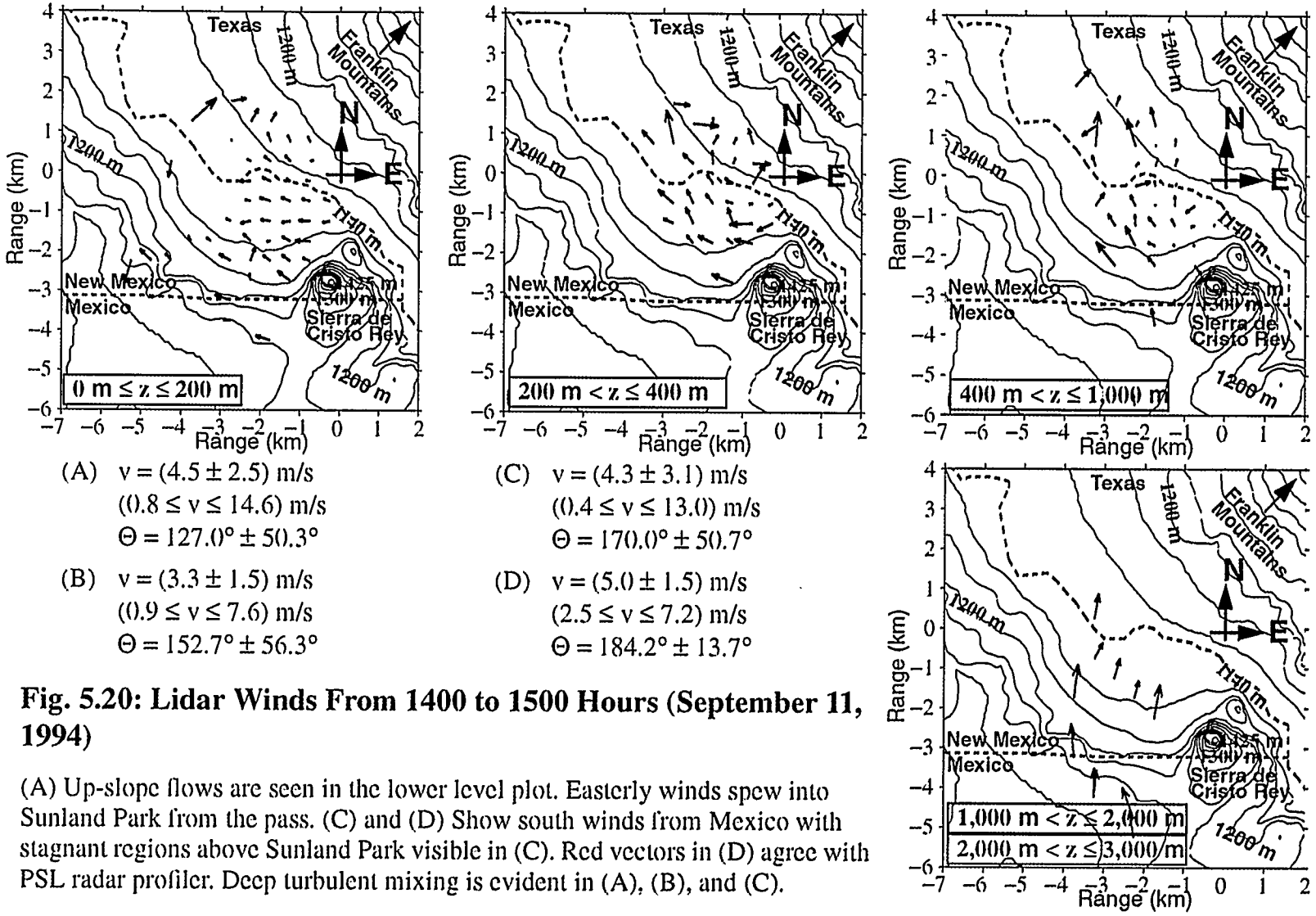

(A) v = (4.5 ± 2.5) m/s
((0.8 ≤ v ≤ 14.6) m/s
Θ = 127.0° ± 50.3°

(B) v = (3.3 ± 1.5) m/s
((0.9 ≤ v ≤ 7.6) m/s
Θ = 152.7° ± 56.3°

(C) v = (4.3 ± 3.1) m/s
((0.4 ≤ v ≤ 13.0) m/s
Θ = 170.0° ± 50.7°

(D) v = (5.0 ± 1.5) m/s
(2.5 ≤ v ≤ 7.2) m/s
Θ = 184.2° ± 13.7°

Fig. 5.20: Lidar Winds From 1400 to 1500 Hours (September 11, 1994)

(A) Up-slope flows are seen in the lower level plot. Easterly winds spew into Sunland Park from the pass. (C) and (D) Show south winds from Mexico with stagnant regions above Sunland Park visible in (C). Red vectors in (D) agree with PSL radar profiler. Deep turbulent mixing is evident in (A), (B), and (C).

(A) $v = (4.9 \pm 3.3)$ m/s
$(1.3 \leq v \leq 10.5)$ m/s
$\Theta = 123.4° \pm 48.9°$

(B) $v = (3.7 \pm 1.8)$ m/s
$(1.6 \leq v \leq 9.0)$ m/s
$\Theta = 194.1° \pm 21.1°$

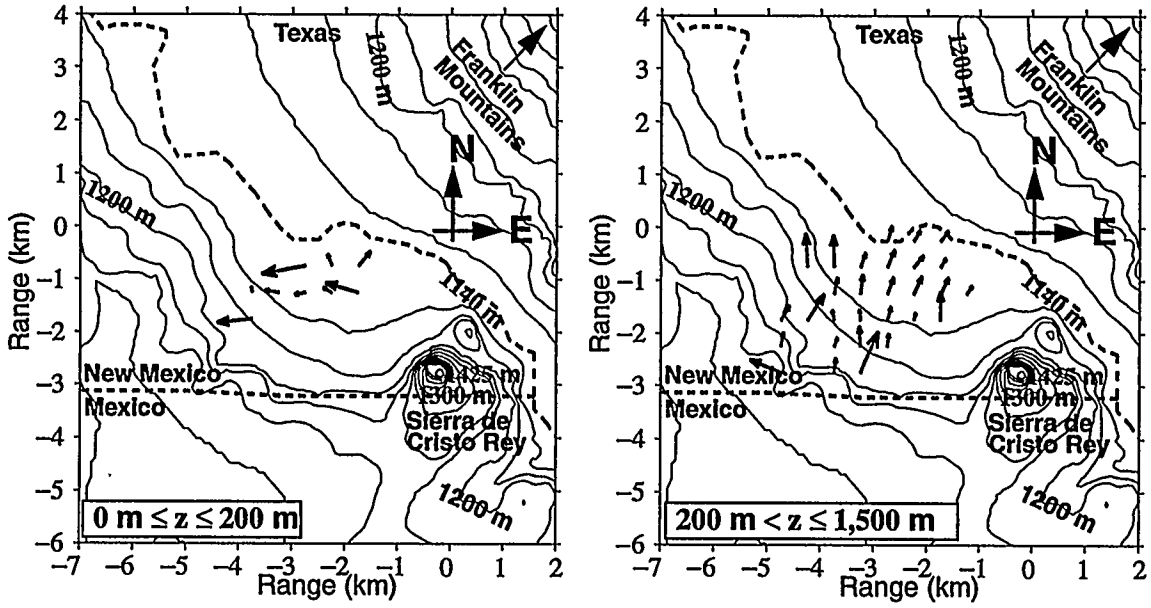

Fig. 5.21: Lidar Winds From 1500 to 1600 Hours (September 11, 1994 Calibration Run)

(A) The lowest 200 m show moderate easterly winds from El Paso into Sunland Park with high variabilities in magnitude and direction. (B) Winds above 200 m are from the SSW with low magnitude and moderate variabilities in magnitude and direction. The wind shear shown between these two plots is also evident in the PSL data plotted in Fig. 5.5.

TABLE 1. Wind Directions into Sunland Park, New Mexico (September 10, 1994)

September 10, 1994	Low Level	Middle Level	High Level	Upper (Red) Level
0800-0900 (Hours) Calibration Run	[0-300 m] (O_3~45 ppb) (El Paso Not Clear) SE From Mexico	[300-1,000 m] Eddy Over LDV (El Paso Not Clear) SSE From Mexico	No Data	No Data
0900-1000 (Hours)	[0-200 m] (O_3~55 ppb) SE From El Paso and Mexico	[200-500 m] No Winds From El Paso, SE From Mexico	[500-1,500 m] SE From El Paso, SSE From Mexico	No Data
1000-1100 (Hours)	[0-300 m] (O_3~74 ppb) SE From El Paso and Mexico	[300-500 m] No Winds From El Paso, SSE From Mexico	[500-1,500 m] SE From El Paso, S From Mexico	No Data
1100-1200 (Hours)	[0-300 m] (O_3~97 ppb) SE From El Paso and Mexico	[300-500 m] SSE From El Paso and Mexico	[500-1,500 m] Stagnation, No Winds From El Paso, S From Mexico	No Data
1200-1300 (Hours)	[0-300 m] (O_3~105 ppb) SE From El Paso and Mexico	[300-500 m] SSE From El Paso, SE From Mexico	[500-1,500 m] Large Eddy, SE From El Paso, S From Mexico	No Data
1300-1400 (Hours)	[0-300 m] (O_3~85 ppb) E From El Paso, ESE From Mexico	[300-500 m] Stagnation, E From El Paso, SSE From Mexico	[500-1,500 m] E From El Paso, S From Mexico	[1,500-3,000 m] S From Mexico
1400-1500 (Hours)	[0-300 m] (O_3~78 ppb) Updraft, E From El Paso, ESE From Mexico	[300-500 m] E From El Paso (Mexico Not Clear)	[500-1,500 m] Stagnation, E From El Paso, S From Mexico	[1,500-2,000 m] Trend is SSW From Mexico
1500-1600 (Hours) Calibration Run	[0-300 m] (O_3~70 ppb) (El Paso Not Clear) S, SSE From Mexico	[300-500 m] (El Paso Not Clear) S, ESE From Mexico	[500-1,500 m] Stagnation, (El Paso Not Clear) S From Mexico	No Data

TABLE 2. Wind Directions into Sunland Park, New Mexico (September 11, 1994)

September 10, 1994	Low Level	Middle Level	High Level	Upper Level(s) Noted By Red Vectors, Except 1400-1500
0800-0900 (Hours)	[0-400 m] (O_3~41 ppb) SE From El Paso and Mexico	[400-1,000 m] Eddy Over LDV, E From El Paso, SE From Mexico	No Data	No Data
0900-1000 (Hours)	[0-200 m] (O_3~45 ppb) SE From El Paso and Mexico	[200-500 m] Stagnation, ESE From El Paso, SE From Mexico	[500-1,500 m] Stagnation, E From El Paso, SE From Mexico	[1,500-2,000 m] (El Paso No Data) SE From Mexico
1000-1100 (Hours)	[0-500 m] (O_3~54 ppb) SE From El Paso and Mexico	[500-1,000 m] Stagnation, E From El Paso, (Mexico Not Clear)	[1,000-2,000 m] Curling Stream, (El Paso Not Clear) SE From Mexico	No Data
1100-1200 (Hours)	[0-200 m] (O_3~57 ppb) SE From El Paso and Mexico	[200-400 m] Stagnation, SE From El Paso and Mexico	[400-1,000 m] SE From El Paso and Mexico	[1,000-1,500 m] (El Paso No Data) Trend: SSE From Mexico
1200-1300 (Hours)	[0-200 m] (O_3~66 ppb) E From El Paso, SE From Mexico	[200-500 m] ESE From El Paso, SE From Mexico	[500-2,000 m] SE From El Paso and Mexico	No Data
1300-1400 (Hours)	[0-200 m] (O_3~69 ppb) E From El Paso and Mexico	[200-500 m] ESE From El Paso, SE From Mexico	[500-1,500 m] SE From El Paso, SSE From Mexico	[1,500-2,000 m] SSW From Mexico
1400-1500 (Hours)	[0-200 m] (O_3~68 ppb) Up Slope Flow, E From El Paso, ESE From Mexico	[200-400 m] E From El Paso, ESE From Mexico	[400-1,000 m] Stagnation, E From El Paso, SSE From Mexico	[1,000-2,000 m] [2,000-3,000 m] S From Mexico
1500-1600 (Hours)	[0-200 m] (O_3~63 ppb) E From El Paso (Mexico No Data)	[200-1,500 m] (El Paso Not Clear) S From Mexico	No Data	No Data

5-5 Observations and Conclusions

The Border Area Air-Quality Study sought to determine whether winds preceding peak O_3 concentrations in Sunland Park, New Mexico, flow into the area from El Paso, Texas, or Juarez, Mexico, or both. Sunland Park experienced peak O_3 concentrations (Kennedy et al. 1994) at 1200 hours on September 10, and at 1300 hours on September 11, 1994. On September 10, O_3 levels quickly dropped to half their peak value of 105 parts per billion (ppb) by around 1600 hours (4 hours later). On September 11, O_3 concentrations reached a maximum of almost 70 ppb and dropped to half the peak value at around 1800 hours (5 hours later). Ozone levels began increasing from a baseline of about 30 ppb at around 0600 hours (sunrise) on both September 10 and 11. (Appendix F contains plots of O_3 concentrations in the Sunland Park region for September 10 and 11, 1994.)

Between 0800 and 0900 hours, on both September 10 and 11, 1994, an eddy was observed in the middle altitudes. The eddies were approximately above the PSL LDV and could account for the poor agreement between the LDV and lidar calibration data between 0800 and 0900 hours on September 10, 1994. An eddy may appear at the same time in the same location on other days as well.

The horizontal scans (Appendix E) support arguments that aerosols are being transported into the Sunland Park region from Texas and Mexico. The horizontal scans were acquired at a 2° elevation angle between the same azimuthal limits as the correlation wind data. The horizontal scan acquired at 1000 hours on September 10, 1994,

showed large volumes of aerosols being transported into Sunland Park from Mexico and a smaller volume of aerosols flowing up the pass from El Paso, Texas. The next time horizontal scans were acquired on September 10 was at 1300 and 1400 hours. Those two horizontal scans suggest low level E winds up the pass with air masses stagnating over Sunland Park.

On September 11, 1994, horizontal scans were acquired at 0900, 1000, 1100, 1200, 1300, and 1400 hours. The horizontal scan at 0900 hours showed aerosols streaming into Sunland Park from Juarez. At 1000 and 1100 hours, the majority of the aerosol masses continued to flow from Juarez with some mass movements up the pass from El Paso. At 1200 hours aerosols were observed to be traveling east. At 1300 and 1400 hours, the horizontal scans showed increased movements up the pass from El Paso with continued movements into Sunland Park from Juarez.

The lidar system can not determine the constituents that make up the aerosols traveling into Sunland Park from Texas and Mexico, or estimate the total mass traveling with the winds. The aerosols may be dust lofted into the boundary layer by cars traveling the many dirt roads in the Juarez area, O_3-producing chemicals, water, or O_3, or all of the above.

I think it is likely, however, that a reservoir of O_3 and aerosols exist within the middle levels and are transported up the Rio Grande River Valley into Sunland Park, New Mexico, from Mexico and Texas preceding peak O_3 levels in the Sunland

Park area. By mid-afternoon the thermal turbulence mixes the aerosols and O_3 down to the surface and decrease the ground level air-quality.

At times, the winds in the middle and upper levels stagnate above Sunland Park. The stagnant zones may be an artifact of vector averaging many different wind vectors, or it could be that O_3 and aerosols carried into Sunland Park from Texas and Mexico precipitate from the stagnant zones and decrease air-quality in this part of New Mexico during the mid- to late-afternoons on September 10 and 11, 1994.

(General descriptions of wind patterns and directions for September 10 and 11, 1996, are summarized in Tables 1 and 2. The descriptions are adapted from Figs. 5.6 to 5.21. The tables include general comments regarding flow patterns into the Sunland Park, New Mexico, region as well as if any stagnation was observed. Obvious eddies are noted.)

References

Kennedy, B. W., J. M. Serna, J. R. Pridgen, D. Kessler, R. Okrasinski, J. G. Moran, G. P. Steele, J. R. Fox, and R. Savage, "Border Area Air-Quality Study 8-11 September 1994," Physical Sciences Laboratory Final Report (1994).

Landau, L. D., and E. M. Lifshitz, "Fluid Mechanics (2nd Edition)," *Course of Theoretical Physics*, Vol. 6, by Pergamon Press plc. (1989).

Schols, J. L. and E. W. Eloranta, "Calculation of Area Averaged Vertical Profiles of the Horizontal Wind Velocity From Volume-Imaged Lidar Data," *Journal of Geophysical Research*, Vol. 97, No. D17 (1992).

Simpson, J. J., and J. I. Gobat, "Robust Velocity Estimates, Stream Functions, and Simulated Lagrangian Drifters from Sequential Spacecraft Data," *IEEE Transactions on Geoscience and Remote Sensing*, Vol. 32, No. 3 (1994).

Appendix A: The LANL Mobile Lidar System[1]

Data for the Border Air-Quality Study (Buttler et al. 1995), analyzed in this thesis, were taken with the Los Alamos National Laboratory mobile, elastic-backscatter lidar system. The system is mounted in a 15-ft Chevrolet Stepvan and is completely self-contained except for the power source. Major components of the system are the laser and transmitting optics, the telescope and receiving optics, the gimbal mount and motors, and the data-acquisition and control system.

The laser is a Continuum NY-81 ND:YAG with a maximum output of 500 mJ/pulse when it is operated at a 1.064-μm wavelength with a repetition rate of 50 Hz and of 250 mJ/pulse at a 532-nm wavelength and a repetition rate of 50 Hz. Laser divergence is 0.5-mrad at full angle. During the Border Air-Quality Study, laser output was about 150 mJ/pulse at a 1.064-μm wavelength with a repetition rate of 50 Hz. The laser is mounted on an optical bench inside the van, and the beam is directed to the gimbals on the roof through Coudé optics. The beam exit is about 19 in. off the centerline of the telescope optical axis.

Scanning is done under computer control. Compumotor servomotors are used to drive each axis. Drive resolution is 13,333 steps per degree azimuth and 17,778 steps per degree elevation. Shaft encoders of 14-bit resolution give a read-out resolution of 0.0220°.

---

1. This description of the LANL mobile lidar is excerpted from the "Sunland Park Border Air-Quality Study," authored by David A. Clark. David has granted me permission to include this description of the mobile lidar system in my thesis.

The receiving system consists of an Office of Scientific and Technical Information (OSTI) 16-in.-diam f/8 Cassegrain telescope, a dichroic beam splitter, bandpass filter, neutral-density attenuators, transfer lenses, and silicone avalanche photodiode detectors (APDs). The dichroic beam splitter allows simultaneous acquisition of 1.064-μm and 532-nm data. Only the 1.064-μm signal was used for the Border Air-Quality Study. Transfer lenses in front of the APDs give them a field of view (FOV) of 3 mrad. Amplifiers and a fiber-optic driver system are built into the small APD packages. Analog signals from the detectors are digitized by 12-bit DSP-2112 CAMAC-based digitizers operating at 20 megasamples per second. Starting at the time of the outgoing laser burst 1024 channels were digitized.

Digitizer memory is read by a Dell 486DX66 computer and placed onto the internal hard disk after each laser shot. Periodically, data files are transferred to 500-MB optical disks for archiving and subsequent analysis.

Appendix B: Cross-Correlation Computer Code I

```
function Mxc2 = xc2(Kij,SS)
%     Algorithm is based on the Correlation Theorem.
%
%     This function was written by William T. Buttler.
%     Most recent modification was November 4, 1995.
%
%     This function calculates the 2D lag matrix between a given 2D kernel
%     and a given 2D search space.
%
%     Inputs: zero-averaged and normalized 2-D kernel, Kij; search space,
%     SS. Returns: Mxc, the normalized cross-correlation matrix.
%
%     Allocate data storage arrays.
[ln_rijl n_tij] = size(Kij);
[ln_ruvln_tuv] = size(SS);
m_ = floor(ln_rij/2);
m_ = m_+1:ln_ruv-m_;
n_ = floor(ln_tij/2);
n_ = n_+1:ln_tuv-n_;
K = zeros(ln_ruv,ln_tuv);
Filter = K;
sum_mask = ones(ln_rij,ln_tij);
%
%     Determine indices to position the kernel and the summing filter mask
%     in the center of zero padded storage arrays, and then place the kernel
%     and summing mask in the zero padded arrays.
n = floor((ln_tuv - ln_tij)/2);
N = n+1:n+ln_tij;
m = floor((ln_ruv - ln_rij)/2);
M = m+1:m+ln_rij;
K(M,N) = Kij;
Filter(M,N) = sum_mask;
%     Calculate un-normalized correlation matrix between kernel and search
%     space.
A = fft2(K); B = fft2(SS); B = conj(B);
Mxc = real(ifft2(A.*B));
Mxc = fftshift(Mxc);
```

```
Mxc = Mxc(m_,n_);
%     Calculate the normalization factors for the cross-correlation matrix.
%     First calculate the average of the search space with the sum_mask,
%     sum over the square of the search space. Then divide Mxc pixels by
%     the appropriate normalization factor.
A = fft2(Filter);
Sum = real(ifft2(A.*B));
Sum = fftshift(Sum);
Sum = Sum(m_,n_);
Sum_sq_N = (Sum.*Sum)/(ln_rij*ln_tij);
B = conj(fft2(SS.*SS));
nrm = real(ifft2(A.*B));
nrm = fftshift(nrm); nrm = nrm(m_,n_);
nrm = sqrt(nrm - Sum_sq_N);
for m = 1:length(n_)
      Mxc(:,m) = Mxc(:,m)./nrm(:,m);
end
Mxc2 = fliplr(flipud(Mxc));
```

Appendix C: Cross-Correlation Computer Code II

```
function Mxc2 = xplicit_sum(Kij,SS)
%     Algorithm is based on the explicit definition of the correlation matrix
%     and does not use the Correlation Theorem.
%
%     This function calculates the 2D lag matrix between a given 2D kernel
%     and a given 2D search space using explicit summation.
%
%     Inputs: zero-averaged and normalized 2-D kernel, Kij; search space,
%     SS. Returns: Mxc, the normalized cross-correlation matrix.
%
%     The average execution time is roughly 2.03 seconds for correlations
%     between a kernel of dim(Kij) = 31x9, and a search space of
%     dim(SS) = 81x40.
%_____________________________________________________________________
[n m] =size(Kij);
[N M] = size(SS);
Q = m*n;
Mxc2 = zeros(N-n+1,M-m+1);
SS_2 = SS.*SS;

A = sum(SS(:,1:m)');
B = sum(SS_2(:,1:m)');
p = 1;
s = p + m - 1;
s1 = sum(A(1:n));
s2 = sum(B(1:n));
for q = 1:N-n
  u = q+n-1;
  Mxc2(q,p) = sum(sum(SS(q:u,p:s).*Kij))/sqrt(s2 - s1*s1/Q);
  s1 = s1 - A(q) + A(q+n);
  s2 = s2 - B(q) + B(q+n);
end
q = q+1;
u = u+1;
Mxc2(q,p) = sum(sum(SS(q:u,p:s).*Kij))/sqrt(s2 - s1*s1/Q);

A = sum(SS(1:n,:));
```

```
B = sum(SS_2(1:n,:));
for q = 1:N-n
   u = q+n-1;
   s1 = sum(A(1:m));
   s2 = sum(B(1:m));
   for p = 2:M-m+1
        r = p-1;
        s = r+m;
        s1 = s1 - A(r) + A(s);
        s2 = s2 - B(r) + B(s);
        Mxc2(q,p) = sum(sum(SS(q:u,p:s).*Kij))/sqrt(s2 - s1*s1/Q);
   end
   A = A - SS(q,:) + SS(q+n,:);
   B = B - SS_2(q,:) + SS_2(q+n,:);
end
q = q + 1;
u = q+n-1;
s1 = sum(A(1:m));
s2 = sum(B(1:m));
for p = 2:M-m+1
   r = p-1;
   s = r+m;
   s1 = s1 - A(r) + A(s);
   s2 = s2 - B(r) + B(s);
   Mxc2(q,p) = sum(sum(SS(q:u,p:s).*Kij))/sqrt(s2 - s1*s1/Q);
end
```

Appendix D: Vertical Scans (10 and 11 September 1994)

This appendix includes vertical lidar scans acquired over Sunland Park, New Mexico. Data were acquired with the lidar facing southwest observing the distribution of aerosols in the vertical dimension over Sunland Park on September 10 and 11, 1994. The vertical scans clearly revealed the inhomogeneous nature of the boundary layer structure. In these 12 images, red colors indicate regions of high backscatter returns and blue colors indicate regions of low backscatter returns.

The first six images were acquired hourly beginning at 0900 hours and ending at 1400 hours on September 10, 1994, respectively; the second six images were acquired at the same times on September 11, 1994. Each set of six images revealed how the boundary layer grows with increasing insolation and anthropogenic

0900 HOURS: SEPTEMBER 10, 1994

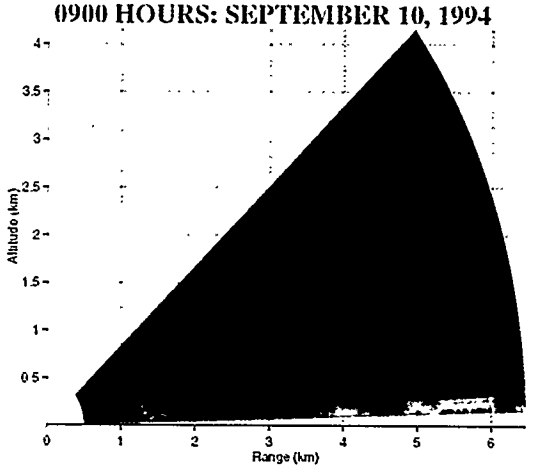

1000 HOURS: SEPTEMBER 10, 1994

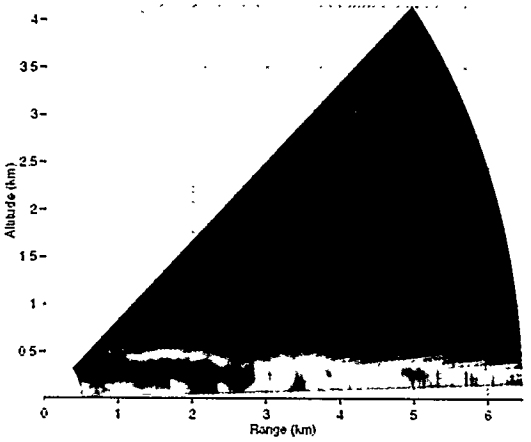

1100 HOURS: SEPTEMBER 10, 1994

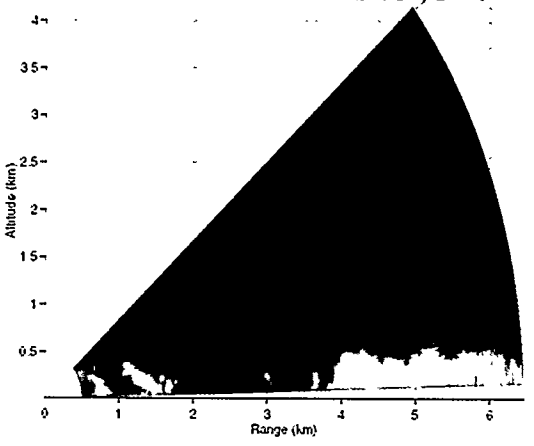

activity by entraining cleaner air from above the boundary layer into dirtier air below. The entrainment process is one mechanism responsible for the formation of nonuniform aerosol distributions. These nonuniformities are characterized by persistent trackable features which allow for the remote sensing of three-dimensional winds throughout a large volume within the boundary layer. In this thesis, lidar winds were extracted with the maximum cross-correlation method (discussed in detail in Ch. 4), and the application of a vector median filter to the lidar wind data base (discussed in Ch. 5).

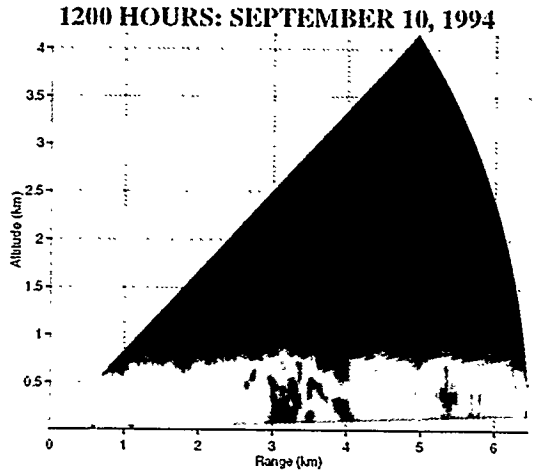

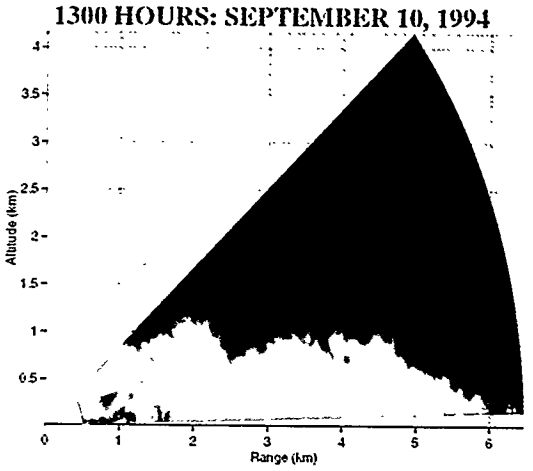

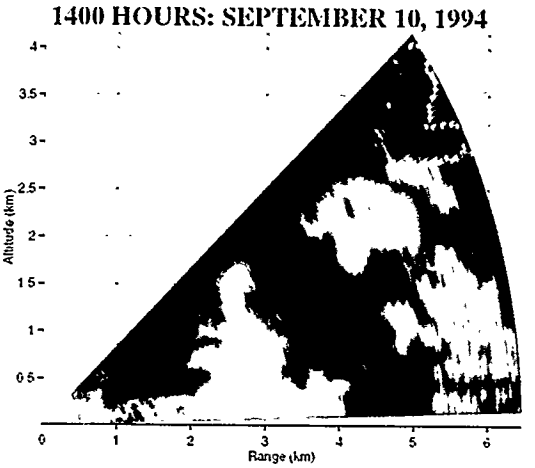

The boundary layer had a mean depth of approximately 400 m at 0900 hours on September 10, 1994. As insolation, industrial activity, and other human activity increased, the boundary layer thickened or increased in depth until

boundary layer aerosols were observed to extend to the bottom of the cloud imaged in the 1400 hours vertical scan. It is not clear that the bottom of the cloud defined the top of the boundary layer at that time because physical processes occurring within the cloud may have caused an updraft which pulled boundary layer aerosols to the cloud's higher altitude. The 1400 hours wind fields from September 10, 1994 (seen in Fig. 5.12 in Ch 5), lends support to this updraft hypothesis. As further evidence that the boundary layer structure was an updraft, we note the convective plume seen at a range of 2.6 km from the lidar in the same vertical scan. The plume only extended to an altitude of 1.7 km above the lidar's position while the cloud bottom was at an altitude of 2.7 km above the lidar position. Convective plumes are known to penetrate through the boundary

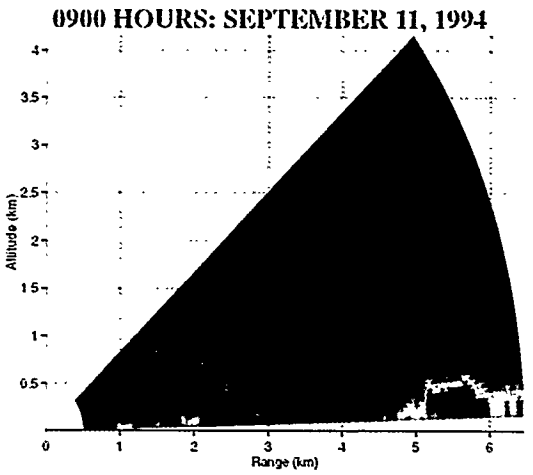

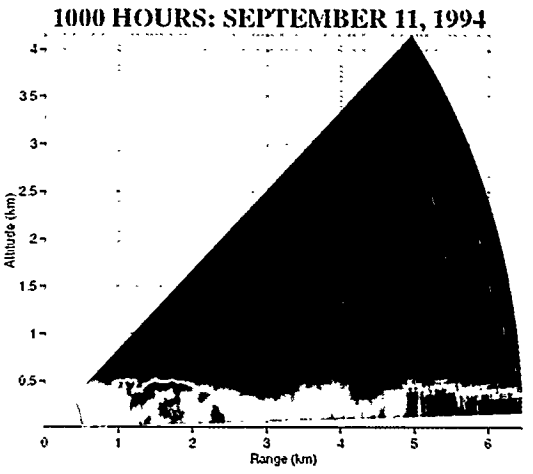

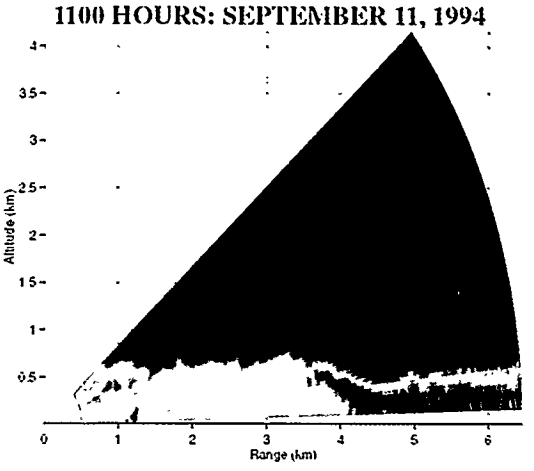

layer into the entrainment zone. This fact coupled with the well defined boundary layer depth shown in the preceding hours vertical scan suggest that the boundary layer depth was likely between 1,200 and 1,500 m.

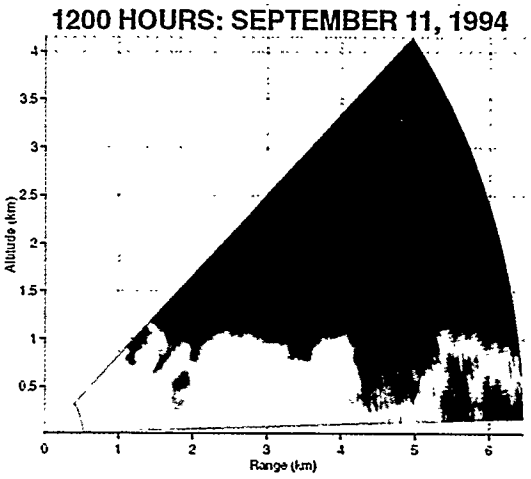

There were no residual layers visible in these six vertical scans from September 10, 1994.

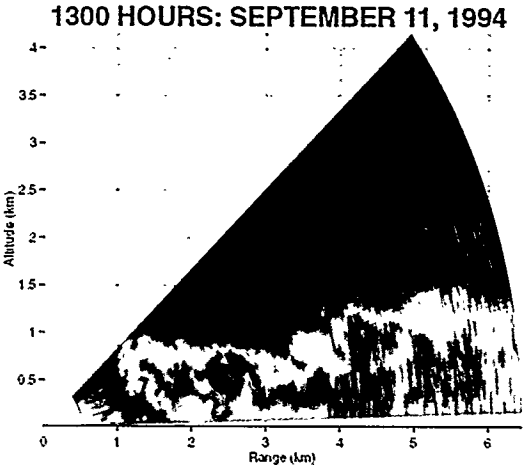

The second six images were acquired hourly beginning at 0900 hours and ending at 1400 hours on September 11, 1994, respectively. These images also showed how the boundary layer grows throughout the day.

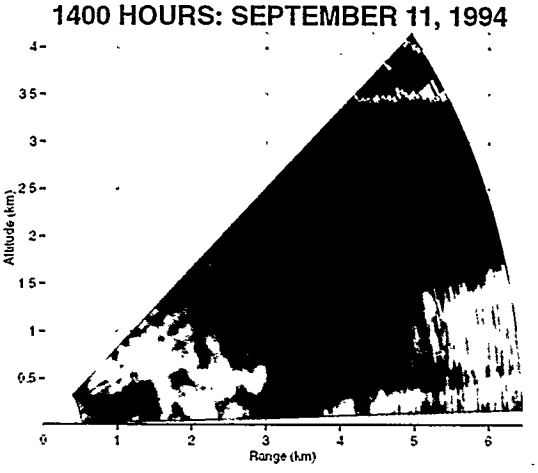

Of interest in these six images were the residual layers visible in all six images. This is particularly interesting since September 11, 1994, was a Sunday and there is no obvious explanation as to what might have caused those layers, espe-

cially when one considers the fact that no residual layers were present in the six images from Saturday, September 10, 1994. Worth noting is that a large smelter was nearby. The smelter was equipped with a tall smokestack and may have directly injected aerosols into the atmosphere above the boundary layer during the early morning before the sun rose.The smokestack was about 185 m above ground at its location.

The mean boundary layer depth was observed to be between 400 and 600 m at 0900 hours and reached a maximum depth of about 1,500 m at 1400 hours on September 11, 1994. In the last image a cloud was present. The cloud bottom was about 3,400 m above the lidar position.

Appendix E: Horizontal Scans (10 and 11 September 1994)

This appendix includes horizontal scans acquired on September 10 and 11, 1994. These scans aid in confirmation of lidar winds and are approximate snapshots of the distributions of aerosols in the horizontal dimension. In the images which follow, red colors indicate locations of high return powers (backscattered intensities) and blue colors indicate regions of low return powers.

Variations in return power can result from a variety of reasons. For instance, any change in the local aerosol densities, sizes or shapes, or the relative mixtures or distributions of aerosol species can effect a change in backscattered intensities. Thus, we cannot differentiate scatterers as pollutants, dust, or water, with a single-wavelength (mono-static) lidar system. We can only note that relative backscattered intensities have changed.

The horizontal scan at right showed aerosol transport consistent with the moderate to strong SE winds observed by the lidar near this time. The main body of the imaged aerosols were moving into New Mexico from Mexico with some aerosols seen travelling into the area from El Paso.

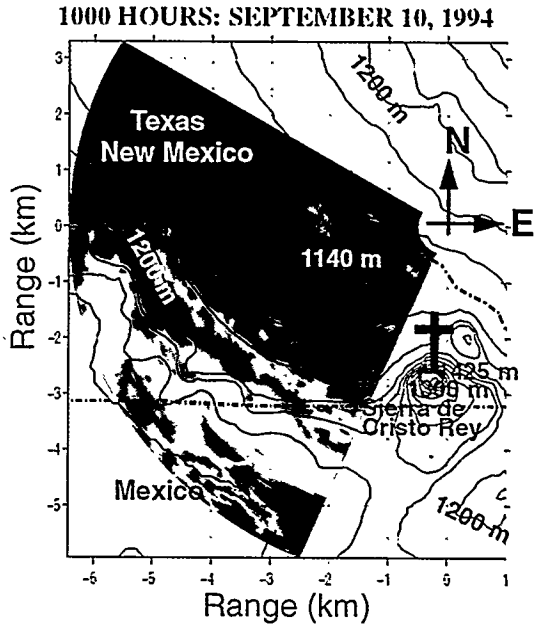

The next horizontal scan was acquired 3 hours later on September 10, 1994, and showed aerosol distributions consistent with the local winds observed by the lidar. The lidar winds were E from El Paso and turned to S winds after clearing the pass. This is evidenced in the collecting of the aerosols within a distance of 3 or 4 km of the north pass and Sierra de Cristo Rey. The aerosols appeared to have entered the area from both El Paso and Mexico.

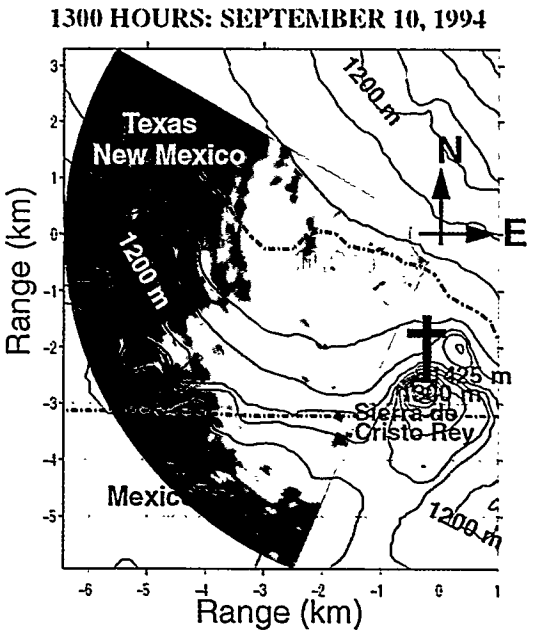

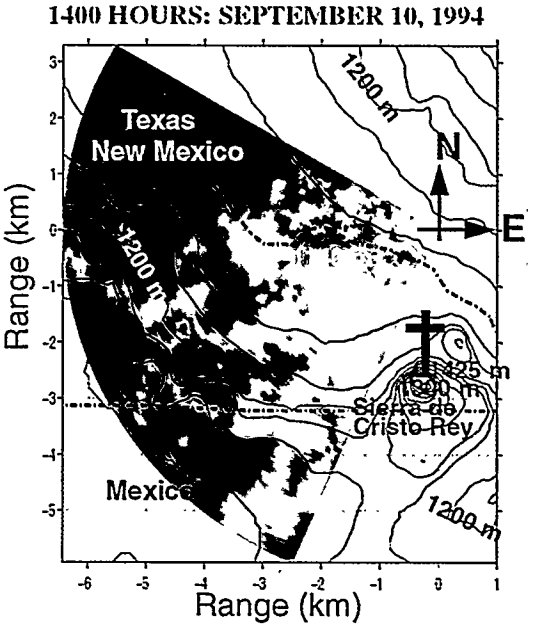

The 1400 hours scan was also consistent with E winds from El Paso which turned to S winds after clearing the pass. At this time, large areas of low return powers were observed 3 to 5 km west of the lidar and Sierra de Cristo Rey. This was consistent with the lidar wind fields from Ch. 5 in the clear areas. The deep red spot about 2 km south and 4.5 km west of the lidar was near the NuMex landfill (where PSL's radar profiler was positioned) and was most likely caused by dust.

The remaining 6 scans were acquired on September 11, 1994. The 0900 hours scan (upper right corner of this page) showed large volumes of aerosols streaming into Sunland Park from Juarez, Mexico; smaller volumes of aerosols flowed with SE winds from El Paso. The stream lines correlate strongly with the strong SE winds observed by the lidar at this time.

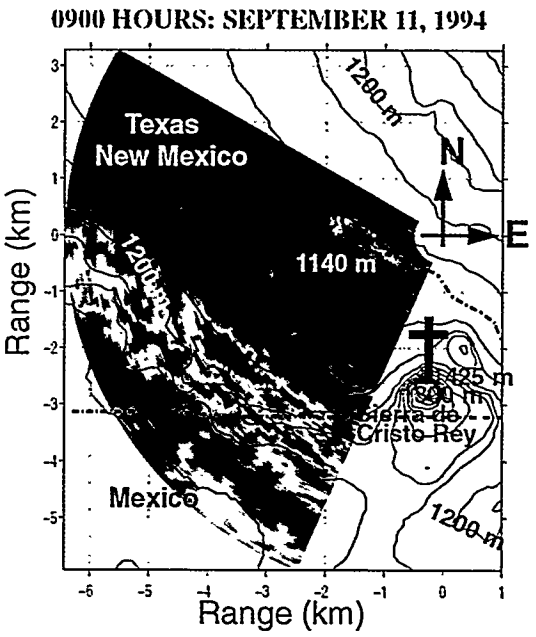

The 1000 hours scan also showed large volumes of aerosols moving into the region from Mexico and smaller volumes moving into Sunland Park, up the north pass, from El Paso. These images lend strong support to the theory that many of the local aerosols in the Sunland Park region travel into the area from Mexico and El Paso; it follows that the majority of Sunland Park's pollution problems may be caused by pollutants entering the region from Mexico and Texas.

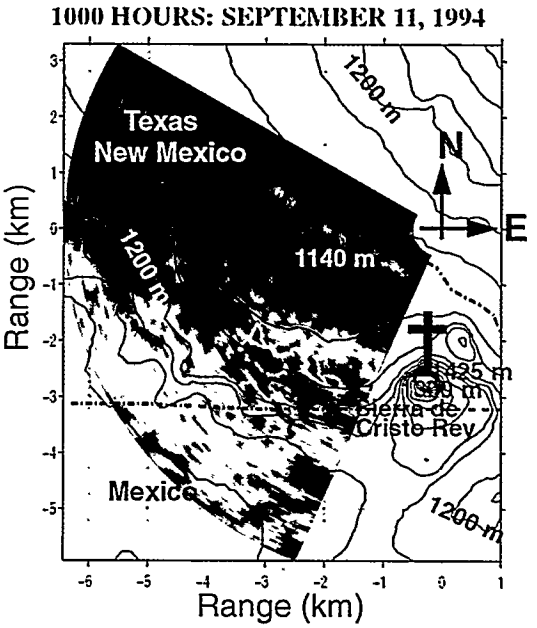

The 1100 hours image showed more aerosols streaming into Sunland Park from Mexico. Again, this was consistent with SE winds from El Paso and Mexico. The

major portion of the aerosols were seen entering the area from Mexico with a small portion up the north pass from El Paso.

The 1200 hours image showed a very strong return 2 km south of and 5 km west of the lidar's position. This is where the NuMex landfill is located and those aerosols were probably dust lofted into the air by the landfill's earth moving equipment. Otherwise, it appeared that the majority of the aerosols continued to flow into the area from Mexico. Peak O_3 levels in the Sunland Park area were observed at 1300 hours on September 11, 1994. However, at 1200 hours the O_3 levels were within 5 parts per billion (ppb) of the peak levels observed at 1300 hours.

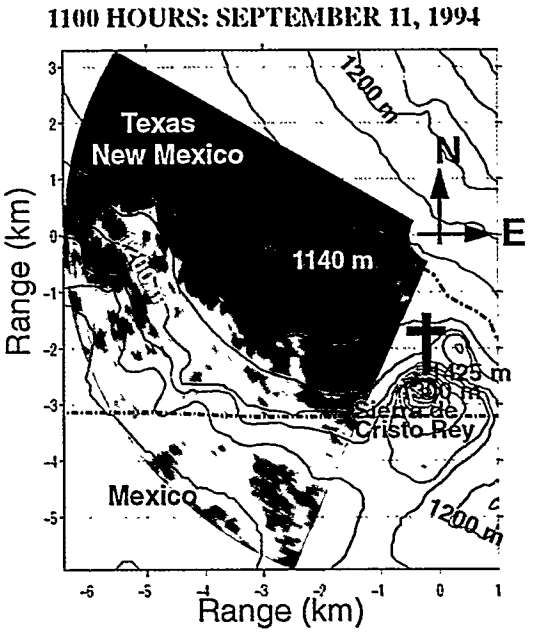

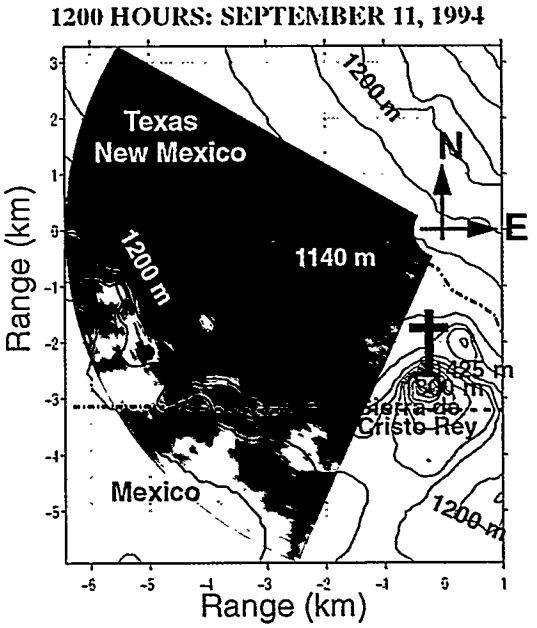

At 1300 hours, winds were E from El Paso, ESE from Mexico, and showed low to moderate magnitudes. The NuMex landfill showed two strong returns in its vicinity and aerosols were collecting over the Sunland Park area. Ozone reached its peak level at this hour.

At 1400 hours, winds showed low magnitudes with some up-slope flows on opposite sides of the Rio Grande. Up-slope flows are expected at this time of day. Local stagnation was evidenced by the several concentrated strong returns in the Sunland Park area at this time. Earlier data showed a smeared out appearance to the plumes. Ozone levels at this time were within a few ppb of the peak value observed on this day and were observed to decline sharply after 1400 hours.

1300 HOURS: SEPTEMBER 11, 1994

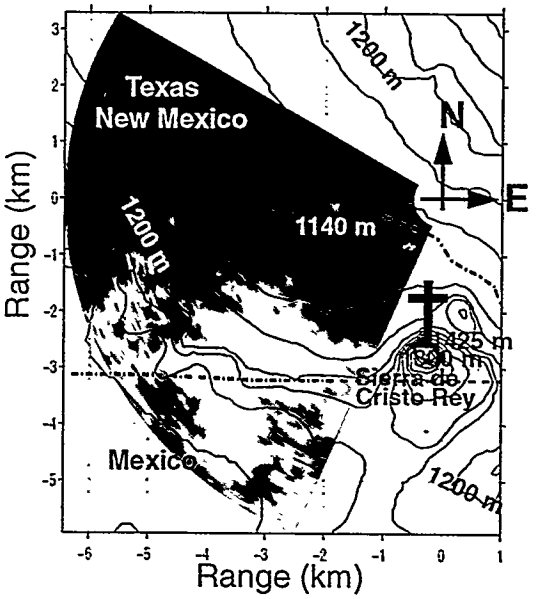

1400 HOURS: SEPTEMBER 11, 1994

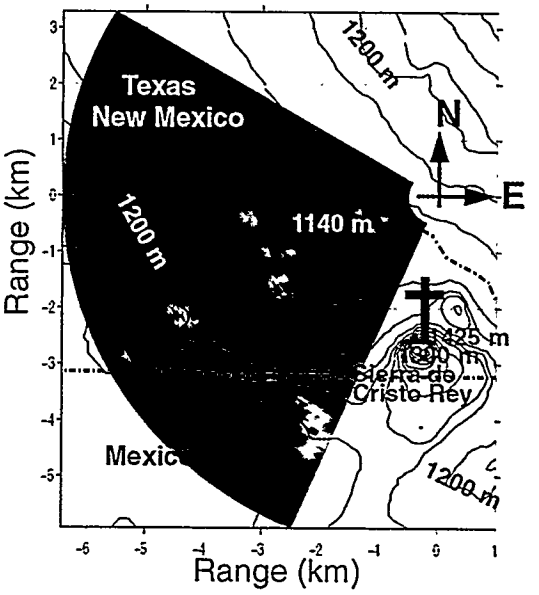

Appendix F: Sunland Park Ozone Levels

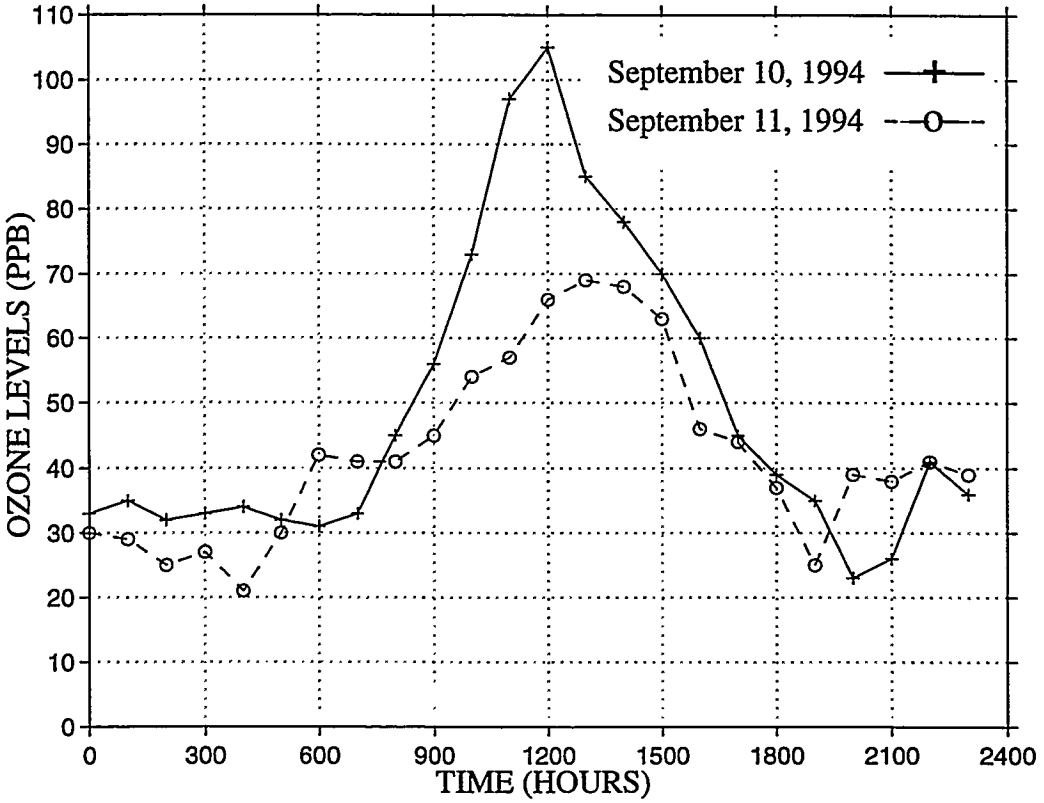

This figure shows ozone levels for September 10 and 11, 1994. These data were provided by the Physical Sciences Laboratory and are published in *The Border Area Air Quality Study, 8-11 September, 1994*, by Kennedy et al. 1994.

Bibliography

Bairlein, R., "Newtonian Dynamics," by McGraw-Hill, Inc. (1983)

Batchelor, G. K., "An Introduction to Fluid Dynamics," by Cambridge University Press (1967).

Bendat, J. S., and A. G. Piersol, "Random Data: Analysis and Measurement Procedures," John Wiley and Sons (1971).

Bohren, C. F., and D. R. Huffman, "Absorption and Scattering of Light by Small Particles," by John Wiley and Sons, Inc. (1983).

Brutsaert, W., "Evaporation of Water into the Atmosphere," by Klewer Academic Publishers (1982).

Buttler, W. T., W. E. Eichinger, C. G. Lebeda, D. I. Cooper, and J. Moses, "Barcelona Air-Quality Initiative," *Alliance For Transportation Research, Project Document,* ATR 94-1 (1994).

Buttler, W. T., C. Soriano, D. A. Clark, C. R. Quick, and T. N. Oakeley, "Sunland Park Border Air-Quality Study," Los Alamos National Laboratory Document LA-UR-95-861 (1995).

Emery, W. J., A. C. Thomas, and M. J. Collins, "An Objective Method for Computing Advective Surface Velocities from Sequential Infrared Images," Journal of Geophysical Research. Vol. 91, No. C11 (1986).

Evans, H. L., "Laminar Boundary-Layer Theory," by Addison-Wesley Publishing Company, Inc. (1968).

Garcia, C. A. E., and I. S. Robinson, "Sea Surface Velocities in Shallow Seas Extracted From Sequential Coastal Zone Color Scanner Satellite Data," *Journal of Geophysical Research*, Vol. 94, No. C9 (1989).

Ghil, M., and S. Childress, "Topics in Geophysical Fluid Dynamics: Atmospheric Dynamics, Dynamo Theory, and Climate Dynamics," *Applied Mathematical Sciences*, Vol. 60, by Springer-Verlag New York, Inc. (1987).

Hooper, W. P., and E. W. Eloranta, "Lidar Measurements of Wind in the Planetary Boundary Layer: The Method, Accuracy and Results from Joint Measurements with Radiosonde and Kytoon," *Journal of Climate and Applied Meteorology*, Vol. 25, No. 7 (1986).

Houghton, J. T., "The Physics of Atmospheres (Second Edition)," by Cambridge University Press (1986).

Jackson, J. D.,"Classical Electrodynamics (Second Edition)," by John Wiley & Sons, Inc. (1975).

Kennard, E. H., "Kinetic Theory of Gasses," by the McGraw-Hill Book Company, Inc. (1938).

Kennedy, B. W., J. M. Serna, J. R. Pridgen, D. Kessler, R. Okrasinski, J. G. Moran, G. P. Steele, J. R. Fox, and R. Savage, "Border Area Air Quality Study 8-11 September 1994," Physical Sciences Laboratory Final Report (1994).

Klett, J. D., "Stable Analytical Inversion Solution For Processing Lidar Returns," *Applied Optics,* Vol. 20, No. 2 (1981).

Klett, J. D., "Lidar Inversion With Variable Backscatter/Extinction Ratios," *Applied Optics,* Vol. 24, No. 11 (1985).

Landau, L. D., and E. M. Lifshitz, "Fluid Mechanics (2nd Edition)," *Course of Theoretical Physics*, Vol. 6, by Pergamon Press plc. (1987).

Leese, J. A., C. S. Novak, and B. B. Clark, "An Automated Technique for Obtaining Cloud Motion from Geosynchronous Satellite Data Using Cross Correlation," *Journal of Applied Meteorology*, Vol. 10 (1971).

Leith, C. E., Classroom notes on Atmospheric Physics, circa 1960's.

McIlveen, R., "Fundamentals of Weather and Climate," by Chapman & Hall (1992).

Measures, R. M., "Laser Remote Sensing: Fundamentals and Applications," by John Wiley and Sons, Inc. (1984).

Ninnis, R. M., W. J. Emery, and J. M. Collins, "Automated Extraction of Pack Ice Motion from Advanced Very High Resolution Radiometer Imagery," *Journal of Geophysical Research*, Vol. 91, No. C9 (1986).

Press, W. H., S. A. Teukolsky, W. T. Vetterling, and B. P. Flannery, "Numerical Recipes in FORTRAN: The Art of Scientific Computing (Second Edition)," Cambridge University Press (1992).

Reichl, L. E., "A Modern Course in Statistical Physics," Copyright © 1980, by the University of Texas Press.

Serna, J. M., Physical Science Laboratory, Box 30002, Las Cruces, New Mexico 88003-0002.

Schols, J. L. and E. W. Eloranta, "Calculation of Area Averaged Vertical Profiles of the Horizontal Wind Velocity From Volume-Imaged Lidar Data," *Journal of Geophysical Research*, Vol. 97, No. D17 (1992).

Simpson, J. J., and J. I. Gobat, "Robust Velocity Estimates, Stream Functions, and Simulated Lagrangian Drifters from Sequential Spacecraft Data," *IEEE Transactions on Geoscience and Remote Sensing*, Vol. 32, No. 3 (1994).

Soriano, C., W. T. Buttler, and J. M. Baldasano, "Comparison of Temperature and Humidity Profiles with Elastic Backscatter Lidar Data," *Air Pollution III*, Vol. 2, Air Pollution Engineering and Management (1995).

Sroga, J. T., and E. W. Eloranta, "Lidar Measurement of Wind Velocity Profiles in the Boundary Layer," *Journal of Applied Meteorology*, Vol. 19, No. 5 (1980).

Stull, R. B., "An Introduction to Boundary Layer Meteorology," by Klewer Academic Publishers (1988).

Sommerfeld, A., "Thermodynamics and Statistical Mechanics," *Lectures on Theoretical Physics*, Vol. V, Printed by Academic Press, Inc. (1956).

United States Geologic Survey (USGS), 1.800.USA.MAPS; Digital Elevation Map Site: "Anonymous FTP: edcftp.cr.usgs.gov." The digital elevation map (DEM) used in this thesis can be found in "pub/data/DEM/250/E/el_paso-w.gz" at the anonymous ftp site listed above. The USGS 7.5 minute DEMs are in compressed "gzip" freeware format.

AUTHOR'S PUBLICATIONS

Quick, Jr., C. R., W. T. Buttler, W. E. Eichinger, D. B. Holtkamp, C. F. Lebeda, R. J. Martinez, D. A. Richter, L. L. Tellier, and J. J. Tiee, "1992 Mexico City Lidar Measurements Campaign," Los Alamos National Laboratory Document LA-UR-93-3657 (1993).

Buttler, W. T., and W. E. Eichinger, "Wind Speed Measurements With a Scanning-Elastic Backscatter Lidar," *21st Conference on Agricultural & Forest Meteorology*, March 7-11, 1994.

Buttler, W. T., W. E. Eichinger, C. F. Lebeda, D. I. Cooper, and J. Moses, "Barcelona Air-Quality Initiative," *Alliance for Transportation Research Project Document*, Albuquerque, New Mexico. Project Document No. ATR 94-1 (1994).

Buttler, W. T., G. H. Nickel, C. Soriano, J. Smith, J. Archuleta, D. A. Clark, W. B. Cottingame, L. L. Tellier, and J. C. Heskett, "El Paso Demonstration: Wind Speed Measurements with a Scanning Elastic-Backscatter Lidar," Los Alamos National Laboratory Document LA-UR-94-2902 (1994).

Dyer, P., D. M. Alde, W. T. Buttler, D. A. Clark, W. Cottingame, R. R. Karl, Jr., T. W. Meyer, C. R. Quick, Jr., W. W. Saylor, J. R. Stephens, J. J. Tiee, and B. Wong-Swanson, "Lidar Elastic Backscattering Measurements of Rocket Bodies and Exhaust Plumes," Los Alamos National Laboratory Report LA-12974-MS (1995).

Buttler, W. T., C. Soriano, D. A. Clark, C. R. Quick, and T. N. Oakeley, "Sunland Park Border Air-Quality Study," Los Alamos National Laboratory Document LA-UR-95-861 (1995).

Soriano, C., W. T. Buttler, and J. M. Baldasano, "Comparison of Temperature and Humidity Profiles With Elastic Backscatter Lidar Data," *Air Pollution III*, Vol. 2, Air Pollution Engineering and Management (1995).

Moore, K. R., D. M. Alde, W. T. Buttler, M. P. Caffrey, M. M. Schauer, and C. Soriano, "Performance of a VME-Based Parallel Processing Lidar Data Acquisition System," *International Conference on Computer Applications in Engineering Medicine*, November 29-December 1, 1995.

Hollen, G. Y., D. Rej, and W. T. Buttler, "Physics Division Technology Review: Remote Sensing in the Atmosphere," Los Alamos National Laboratory Publication LALP-95-85 (1995).